OBSERVATIONS AND MODELING OF THERMALLY DRIVEN WIND JETS AT THE EXIT OF A UTAH CANYON

by

Morgan Farley-Chrust

A thesis submitted to the faculty of
The University of Utah
in partial fulfillment of the requirements for the degree of

Master of Science

Department of Atmospheric Sciences

The University of Utah

December 2011

The University of Utah Graduate School

STATEMENT OF THESIS APPROVAL

The thesis of **Morgan Farley-Chrust**

has been approved by the following supervisory committee members:

C. David Whiteman	, Chair	**10/21/2011** Date Approved
W. James Steenburgh	, Member	**10/21/2011** Date Approved
John D. Horel	, Member	**10/21/2011** Date Approved

and by **Kevin D. Perry** , Chair of

the Department of **Atmospheric Sciences**

and by Charles A. Wight, Dean of The Graduate School.

ABSTRACT

This thesis investigates summertime thermally driven wind circulations in a Utah canyon. The study is focused around Weber Canyon, Utah, which is a main tributary canyon that feeds into the Great Salt Lake basin. A measurement campaign was conducted during July-September 2010 to observe and characterize the wind flow patterns in Weber Canyon and specifically the nature of the summertime fair-weather wind jet that has been observed to form at the exit region of Weber and other Utah canyons. This thesis research uniquely combines many meteorological data sources including existing automatic weather stations, measurement equipment borrowed from several generous parties, and equipment owned by the University of Utah's Atmospheric Sciences department.

Winds within the canyon and at the exit exhibited a strong seasonal and diurnal variation that is linked to the yearly course of solar insolation. Strong nocturnal low-level wind jets formed on 75 of 90 nights (83%) at the Weber Canyon exit during the measurement campaign. Winds inside the canyon consisted of a weak but deep down valley flow layer that occupied most of the depth of the canyon. The flow was observed to descend, thin and compress at the exit where winds were typically twice as strong as inside the canyon and much more shallow. Flow within the canyon and at the exit was influenced by the larger scale synoptic conditions. Clear skies and weak regional pressure gradients along with light winds aloft were conducive to the development of strong

canyon exit flows. Four canyon flow regimes were observed depending upon the strength and orientation of the synoptic flow. Observations of flow properties within and at the exit of the canyon were compared to Large Eddy numerical simulations using the Advanced Research Weather Research and Forecast (ARW) numerical weather prediction (NWP) model developed by NCAR. Good agreement between the observations and model simulations has been achieved. The wind power potential at the exit region is shown to be excellent.

TABLE OF CONTENTS

ACKNOWLEDGEMENTS

I would like to express my sincere gratitude to C. David Whiteman, my advisor and thesis committee chair member for his technical guidance and support in writing this thesis. I would also like to thank my other two committee members W. James Steenburgh and John D. Horel for their valuable comments and suggestions that helped improve the manuscript. I would like to thank Sebastian W. Hoch for his thoughtful input during my research as well as help during the measurement campaign. I would like to thank Joseph S. Young and Christopher Ander for their assistance during the measurement campaign. Thank you to Manuela Lehner and Adam Kochanski for providing valuable guidance while I was learning to run the WRF model. Thank you to the State of Utah anemometer loan program for providing data from the meteorological tower and to NRG Systems Inc. for loaning the WindCube LiDAR for use in this research. Thank you to Gregory S. Poulos and Julie K. Lundquist for their assistance in loaning the LiDAR. Thank you to Alan Marchant and Tom Apedaile from Utah State University for operating and providing data from the ValidWind^{TM} system during the measurement campaign. Several organizations provided land on which measurement equipment was temporarily installed and I am grateful for their cooperation. An allocation of computer time from the Center for High Performance Computing at the University of Utah is gratefully acknowledged. This material is based upon work supported by the National Science Foundation under grant ATM-0938397. Any opinions, findings, and conclusions or recommendations expressed in this material are those of the authors and do not necessarily reflect the view of the National Science Foundation.

CHAPTER 1

INTRODUCTION AND LITERATURE REVIEW

This thesis investigates summertime thermally driven wind circulations in a Utah canyon. The primary study area is Weber Canyon, a small canyon that feeds westward from the Wasatch Mountains into the Great Salt Lake Basin (GSLB). The main goal of this research is to observe and characterize the wind flow patterns in Weber Canyon, and specifically the nature of the summertime fair weather wind jet that has been observed to form at the exit region of the canyon, where it intersects with the GSLB. Exit jets have been observed at the exit of other Utah canyons (Dwyer et al. 2007). In this thesis the term valley will be used interchangeably with canyon but generally refers to a narrow V-shaped topographic feature. Canyons generally flow westward out of the Wasatch Mountains and are usually thought of as the narrow portion immediately adjacent to the GSLB. Most canyons are joined with a larger upstream basin that usually consists of higher mountainous terrain. In this case, the Weber basin originates in the Wasatch and Uinta mountains of Utah and flows northward and westward though Weber Canyon into the GSLB.

The canyon exit jet has gained attention recently due to interest in generating wind energy from the jet. Utah's first wind farm, the 19 MW Spanish Fork Canyon wind project located 120 km south of Weber Canyon, takes advantage of canyon exit winds to generate electricity that is sold to the local electrical utility. The exit jet forms where air

that drains abruptly from a deep but weak down valley flow layer within the canyon transitions to a shallower layer at and beyond the exit where the flow thins, accelerates and is compressed downward. A measurement experiment was conducted at Weber Canyon where many meteorological instruments were sited within and at the exit of the canyon to help quantify the temporal and spatial characteristics of the wind jet. Of particular interest were seasonal and diurnal variations in the strength of the exit jet and how vertical wind and temperature profiles evolved from within the canyon to the exit region. In this thesis, observations of flow properties within and at the exit of the canyon are compared to Large Eddy Simulations (LES) made with the Weather Research and Forecast (WRF-ARW) numerical weather prediction (NWP) model developed by the National Center for Atmospheric Research (NCAR). Good agreement between the observations and model simulations was achieved, which bodes well for the future use of NWP models in simulating weather and climate in complex mountainous terrain. Using the observations, a preliminary estimate of wind power potential at the Weber Canyon exit region has been made. Results show that the canyon exit region has ample resources to support commercial wind power development.

Several observational and modelling studies of katabatic and anabatic flows that have been performed over the years will be reviewed in this thesis. Few have focused on the relationship between winds within a very narrow canyon and winds at the canyon exit. Furthermore, while there have been several observational studies performed over the years within the GSLB, none have explicitly focused on the flow characteristics of the narrow tributary canyons. Most previous modelling studies are associated with much larger valleys and very few have utilized modern large eddy simulation techniques with

fine grid spacing to model the thermodynamics of wind circulations in such a narrow canyon. This thesis contributes to knowledge of thermally driven wind flows in a narrow tributary canyon within the Wasatch Front range of the Rocky Mountains using modern observational and modelling techniques and expands the use of modern NWP models for simulating mountain weather in complex terrain.

Thermally driven wind circulations

The basic mechanisms that produce thermally driven wind circulations in the intermountain west are described by Stewart et al. (2002). Four circulations dominate the climatology of thermally driven winds within the GSLB. These are (1) plain-mountain winds; (2) valley winds; (3) slope winds; and (4) lake-land breezes. These circulations are a result of spatial temperature contrasts that produce pressure gradients that drive wind circulations. This thesis will explore the thermally driven winds within Weber Canyon, which are a combination of plain-mountain and valley winds. Temperature gradients that form between the GSLB and the mountain and valley atmospheres give rise to horizontal pressure gradients. A resulting wind circulation is confined to flow within the narrow Weber Canyon. Fig. 1 displays a schematic of pressure gradient development as a result of horizontal temperature contrast between a valley and the adjacent plain (Whiteman 2000).

Volumetric heating arguments have been proposed to describe the origins of temperature gradient development (Whiteman 1990). The volumetric heating concept, termed the topographic amplification factor (TAF), considers that an equal heat input into two adjacent air volumes will cause a larger temperature increase in the smaller of the volumes and thus will produce a horizontal temperature gradient between the two

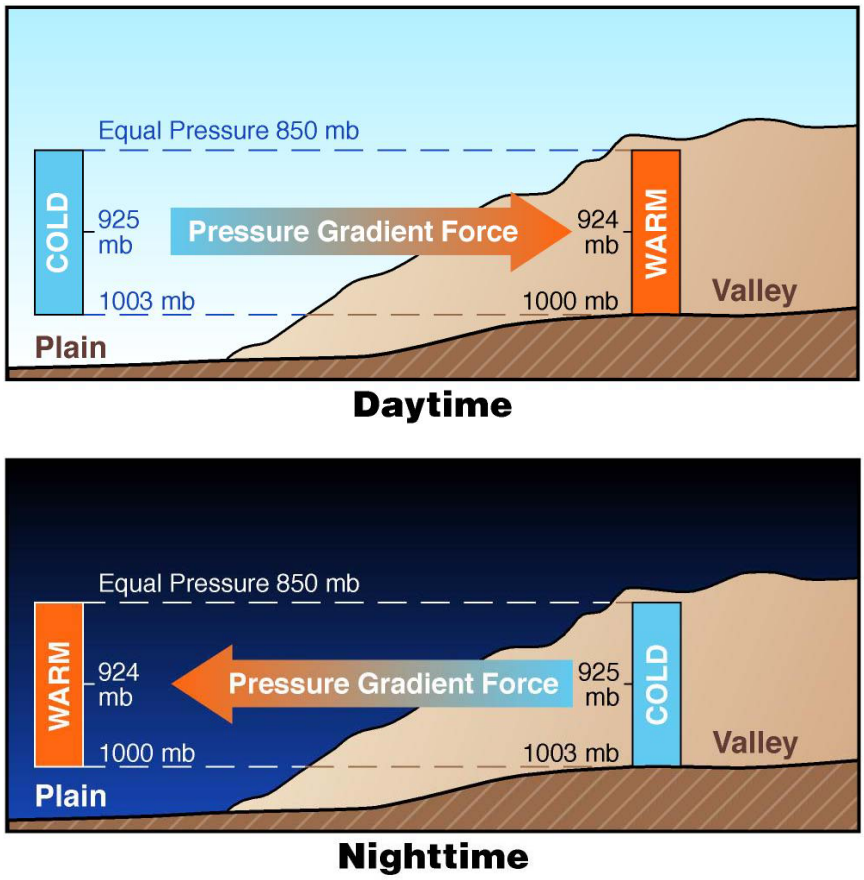

Fig. 1. Schematic of the pressure gradient force resulting from a temperature gradient between a mountain valley and plain atmosphere (from Whiteman (2000)).

volumes. In the case of a mountain valley and its adjacent plain atmosphere, if an equal heat input is supplied over an equal horizontal area above these volumes, the volume of air enclosed beneath the horizontal area in the valley is less than that over the plain, resulting in a larger temperature gain. During the night, similar arguments are applied to radiational cooling, resulting in a greater temperature loss in the valley (Whiteman 1990).

Whiteman and Doran (1993) identify four mechanisms that can produce along-valley winds within a valley. These are (1) thermal forcing, in which winds within the valley are generated by locally produced along-valley pressure gradients due to thermal

contrasts; (2) downward horizontal momentum transport, in which the along-valley component of the momentum of the overlying flow is imparted to the flow within the valley; (3) forced channelling, where ambient geostrophic winds in the direction of the valley axis are channelled by the valley sidewalls to flow within the valley; and (4) pressure driven channelling, where valley winds are driven by the component of the geostrophic pressure gradient that is aligned with the valley axis. Winds that flow down the topographic gradient are termed katabatic winds and winds that flow up the topographic gradient are referred to as anabatic winds. This thesis focuses on the first of the four mechanisms, the thermally driven katabatic and anabatic winds within Weber Canyon and also explores aspects of the other three processes that introduce variability within the Weber Canyon flow.

Katabatic and anabatic flows have been studied since about 1840 and many observational campaigns have contributed to the understanding of basic physical principles involved with these flows. Poulos and Zhong (2008) provide a detailed description of the history of observational campaigns focused on small-scale thermally driven flows in the mid latitudes. Many past studies have focused on the impact of external synoptic meteorology on katabatic and anabatic winds within a valley. Much has been learned through these observational campaigns and a summary of important results is provided here.

Observational studies of valley wind circulations

A Department of Energy-funded meteorological field program was conducted in the Salt Lake Valley in October 2000. The Vertical Transport and Mixing (VTMX) program sought to investigate the mechanisms controlling flows within and into the Salt

Lake Valley. Many papers that provide information on the meteorology of the Salt Lake Valley have been published as a result of this study. These include Doran et al. (2002), Banta et al. (2004), Haiden and Whiteman (2005), Darby and Banta (2006), Darby et al. (2006), Whiteman and Zhong (2008), and Zhong and Whiteman (2008). Darby and Banta (2006) focused on the complex interactions of flows within the Salt Lake Valley and the drainage flows from two major tributary canyons that enter the valley within the Salt Lake City metropolitan area. They also analyzed the relationship between ridge-top winds and tributary canyon outflows. Their study used a scanning Doppler LiDAR at the center of the valley to measure horizontal wind speeds coming out of the canyons. They found that a southerly low-level jet (LLJ) in the Salt Lake Valley suppressed the penetration of canyon outflows into the valley. Strong ridge-top winds also suppressed the canyon outflows, although to a lesser extent. When southerly flows within the Salt Lake Valley reached a speed of 4 m s^{-1}, easterly canyon outflows were shut down temporarily or permanently for the night. When the predominantly southwesterly ridge-top winds were $\geq$ 10 m s^{-1}, canyon outflow winds were inhibited.

Similar studies of thermally driven wind flows were conducted in several other locations as part of the U.S Department of Energy's Atmospheric Studies in Complex Terrain (ASCOT) program. Clements et al. (1989) explored the mean wind and temperature structure of nocturnal drainage flow in the Brush Creek Valley in Colorado. They found that a strong surface-based temperature inversion existed in the lowest 200 m of the valley with near-isothermal conditions above to ridge-top. The vertical wind profile exhibited a low-level jet with jet height equal to 20% of the drainage flow depth. The authors found empirical functions that represented the along-valley and cross-valley

wind profiles and suggested similarity exists in the wind profiles during different canyon flow conditions. They also found that the jet speed increased linearly with increasing surface inversion strength and that the overall depth and mass flux decrease linearly with increasing ridge-top wind speeds.

Coulter and Gudiksen (1995) analyzed 34 months of SoDAR data from within Coal Creek Canyon (CC) in Colorado to investigate the relationship between the flow field within CC, the cooling rate of the surface and the external forcing wind flow. The strength of the external wind affected the magnitude of the wind speed profile but had little effect on the jet maximum height. They also note that strong external winds produced shallower drainage flow with the possibility of recirculation aloft. Based on wind profile parameters they calculated that the most probable jet height, drainage depth and jet speed are 55 m, 110 m and 5.25 m s^{-1} respectively. The authors also compared mean drainage wind profile parameters to other Colorado valleys and found that the wind profiles appear to scale with valley dimensions. It was observed that the ratio of jet height to drainage depth was approximately the same for all valleys as was the ratio of the surface drainage area to the vertical plane through which the wind flows, thus the mass flux from each drainage basin must be confined to the draining valley in a similar way (Coulter and Gudiksen 1995). Other ASCOT studies in the Coal Creek and Brush Creek canyons include Barr and Orgill (1989), Clements et al. (1989), and King et al. (1989).

Despite their regular occurrence, thermally driven low-level jets at the exits of valleys and canyons have been documented at only a few locations around the world. Stilke (1984) and Pamperin and Stilke (1985) observed nocturnal low-level jets at the exit of the Inn Valley with the Rosenheim basin near Thalreit, Germany during the MERKUR

experiment that was conducted during March and April of 1982. The nocturnal low-level jet strengthened during the night and attained a maximum speed of 15 m s^{-1} at a height of around 200 m. Following sunrise the jet rapidly degraded and by 0815 local time the jet profile had almost completely disappeared. Others including Zängl (2004) have also observed low-level jets at the exit of the Inn Valley. In the United States, Banta et al. (1995) observed a low-level jet at the exit of Eldorado Canyon in Colorado during the wintertime, but noted that the jet was present only for a few hours. The jet had a complex vertical structure with peak speeds greater than 6 m s^{-1} at a height of around 600-700 m. Dwyer et al. (2007) documented wintertime nocturnal wind jets at the exit of Spanish Fork Canyon in Utah.

Gap winds

Several analogies can be drawn between small-scale thermally driven, diurnally varying valley exit jets and larger-scale synoptically driven gap winds. Both are a result of pressure gradients that form between two air masses that are separated by gap openings such as channels, valleys or mountain passes. Studies of gap winds have generally been focused in two areas: (1) gap winds through flat bottom channels such as in the Strait of Juan de Fuca south of Vancouver Island (Overland and Walter 1981, Mass et al. 1995), in the Shelikof Strait in Alaska (Lackmann and Overland 1989), or in the Columbia River Gorge (Sharp and Mass 2002, 2004); and (2) gap winds through elevated mountain passes such as those described by Mayr et al. (2007). Overland and Walter (1981) show that the flow magnitudes in the Strait of Juan de Fuca can be explained by the along-valley pressure gradient that exists between the high pressure region over British Columbia and a low pressure system on the Washington coast and that the

strongest winds are found beyond the exit of the gap and not within the narrowest region within the gap. Sharp and Mass (2004) found similar characteristics at the exit of the Columbia River gorge and argue that this finding indicates that venturi effects cannot explain the strong gap winds, rather it is the along valley pressure gradient which maximizes at the exit of the gap that produces the strongest winds downstream of the gap. Our observations at Weber Canyon show similar characteristics where the strongest winds were observed beyond the exit of the canyon and not within the narrow part of the canyon, upstream of the exit. In this context, the exit jets at the Weber Canyon Exit could be interpreted as a gap wind imbedded within a valley flow. Lackmann and Overland (1989) completed a momentum balance for a gap flow event in the Shelikof Strait in Alaska and found that the flow can be described as a balance between the pressure gradient force, inertia, entrainment and friction.

Mayr et al. (2007) compares results from gap flow measurements in the Brenner Pass within the Wipp Valley of Austria to idealized flow simulations over topography. The flow was found to be highly nonlinear and that hydraulic theory can be used to describe the flow conditions. The exit of the gap was found to be the point at which the flow transitioned from subcritical to supercritical. Farther downstream a hydraulic jump was found that returned the flow back to a subcritical state. Warming resulted downstream of the gap due to descent and the author therefore considers this phenomena as a special case of föhn winds.

While many analogies can be made there are still differences between valley exit jets and the gap winds that are described above. Most of the differences have to do with the spatial scale of the wind system and the driving mechanism. Valley exit jets occur on

a much smaller scale and are caused by diurnally varying temperature contrasts between a mountain valley and a plain due to differences in radiational heating and cooling whereas traditional gap winds are much larger in scale and are caused by synoptic-scale pressure gradients. Also, it is unclear whether there is a low-level jet structure at the exit of any of the gaps mentioned above.

Modelling studies of the GSLB

Several modelling studies have been performed for the GSLB over the years. Zhong and Fast (2003) evaluated the performance of the MM5, RAMS and Meso-Eta models over the GSLB. The MM5 and RAMS models performed better than the Meso-eta model. Fast and Darby (2004) used version 5 of the Regional Atmospheric Modelling System (RAMS) to simulate down valley and canyon flows and compare them to measurements from a radar wind profiler and Doppler LiDAR during VTMX. The model was run for nested grid spacings of 45, 15, 5, 1.7 and 0.56 km. The authors note that overall the model captured reasonably well the general features of the observed circulations and that errors were usually associated with the timing, structure, and strength of specific flow features. They report that wind speed bias (simulated-observed) was generally less than 1 m s^{-1}. Interestingly, the predicted wind speeds were lower than observed at the radar wind profiler site and higher than observed at the LiDAR. Wind direction bias was usually within 10º within 1 km of the ground. The authors report that correlation coefficients between observed and simulated winds were higher during periods of significant synoptic forcing and daytime up valley circulations, and were lowest during the evening transition when the flow reverses from up-valley to down-valley. The model performance was better in nocturnal stable conditions when canyon

flows were modified by synoptic forcing compared to evenings with well-developed drainage flows and weak ambient winds. The smallest errors occurred at the lower elevations, indicating that the model simulated flows within the valley better than aloft.

Rife et al. (2004) compared standard verification statistics of low-level wind forecasts for four models in the Salt Lake City area during the 2002 winter Olympics. The four models were the Eta, Rapid Update Cycle (RUC-2), Global Forecast System (GFS) and the fifth generation Pennsylvania State-NCAR Mesoscale Model (MM5), which is the predecessor to the current WRF model. The MM5 model was the only one capable of adequately representing the complex mountainous terrain. The purpose of the study was to investigate why the standard verification measures did not better discriminate amongst the models and to describe alternative measures that might better represent the ability of high horizontal resolution models to forecast locally produced circulations. To assess the spatial variability of diurnal forcing the study included a spectral decomposition of time series data from selected surface weather stations. Results show that the amount of spectral power in the band with diurnal period varies greatly as does the spectral power in bands with longer than diurnal (super diurnal) and shorter (sub diurnal) periods. The authors note that quantitatively determining the power in the diurnal component of the observed time series is important because one of the major potential benefits of high resolution mesoscale models is the ability to capture the diurnal forcing by the local topography, whereas the larger synoptic forcing is understood to be well resolved in current mesoscale models. Therefore mesoscale model forecast quality in a particular area should depend at least partially on the strength of the diurnal forcing and the degree to which the model can represent the forcing (Rife et al. 2004). Three

conventional verification scores were calculated for the wind fields: bias, mean absolute error (MAE) and root mean squared error (RMSE). A strong positive relationship was shown between the strength of the local forcing at each observation location, as measured by the spectral power in the diurnal range, and forecast skill. However the MAE showed no relationship to the power in the diurnal band.

Modelling studies in other mountainous areas

Spengler et al. (2009) also used the Pennsylvania State University-NCAR MM5 model to simulate wind flows in the complex Lech Valley region of Austria. This study compared numerical simulations with data from surface stations and remotely piloted aircraft to analyse flow patterns within the valley and at the asymmetric exit where the valley meets the Bavarian foreland. Modelling results show a LLJ with a wind maximum of around 10 m s^{-1} at the exit and flow that extends 30 km into the foreland. The authors attribute the maximum in the vertical wind speed profile to hydraulic effects with a dipping of isentropic surfaces at the exit. However they note that during the time period for which they took observations that the strong outflow into the foreland was absent from the observations. Modelled surface winds were greater than concurrent observations because the model underestimated the strength of the low-level inversion. Winds were better predicted during daytime than at nighttime.

Zängl (2004) used the Penn State/NCAR MM5 model to perform idealized simulations of the valley wind circulation in Austria's Inn Valley. The simulations were compared to existing data and were used to improve the understanding of valley wind systems. The study used realistic high resolution topography and idealized large scale weather conditions with no synoptic forcing to isolate the thermally induced valley wind

system. He found that the tributaries of the Inn Valley have a large impact on both the up-canyon and down-canyon mass fluxes. Near the exit of the valley a lateral valley contraction was observed to cause important flow features in the canyon near the exit and in the foreland beyond the exit. Due to the constriction, the down valley mass flux was reduced at low levels causing the height of the wind maximum in the interior of the valley to be elevated. Just beyond the valley constriction at the exit the flow accelerated and formed a pronounced low-level jet that maintained its structure several tens of kilometers into the foreland. The author suggests that the acceleration causing the jet could be interpreted as a transition from subcritical to supercritical hydraulic flow.

CHAPTER 2

REGIONAL GEOGRAPHY AND CANYON WIND SYSTEMS

Description of regional canyons and drainage basins

The Wasatch Mountains of Utah run from the northern Utah border south into central Utah and form the border between the Rocky Mountains and the Great Basin farther west. Geographically, the Great Basin contains basin and range topographic elements in which isolated mountain ranges border a multitude of small basins. The Weber River flows westward from the Wasatch Mountains into the larger GSLB. Many other tributary streams flow westward out of the Wasatch Mountains and feed into the GSLB. These tributary streams supply water runoff from the mountains. Canyons generally narrow significantly as they cut through a final ridge before flowing westward out of the Wasatch Mountains into the adjacent GSLB. Most canyons are joined with a larger upstream basin that usually consists of higher mountainous terrain. In the case of Weber Canyon a sub-basin (the Morgan basin) is present immediately east of the narrow 10 km lower section. The canyons provide a path where localized mountain wind circulations flow between the canyon drainage basin and the GSLB. The main drainage basins in the northern Wasatch Mountains are shown in Fig. 2 and their respective areas are listed in Table 1. The Weber and Provo drainage basins are the largest that issue into the northern GSLB. The drainage areas were measured using GIS software. Five meter

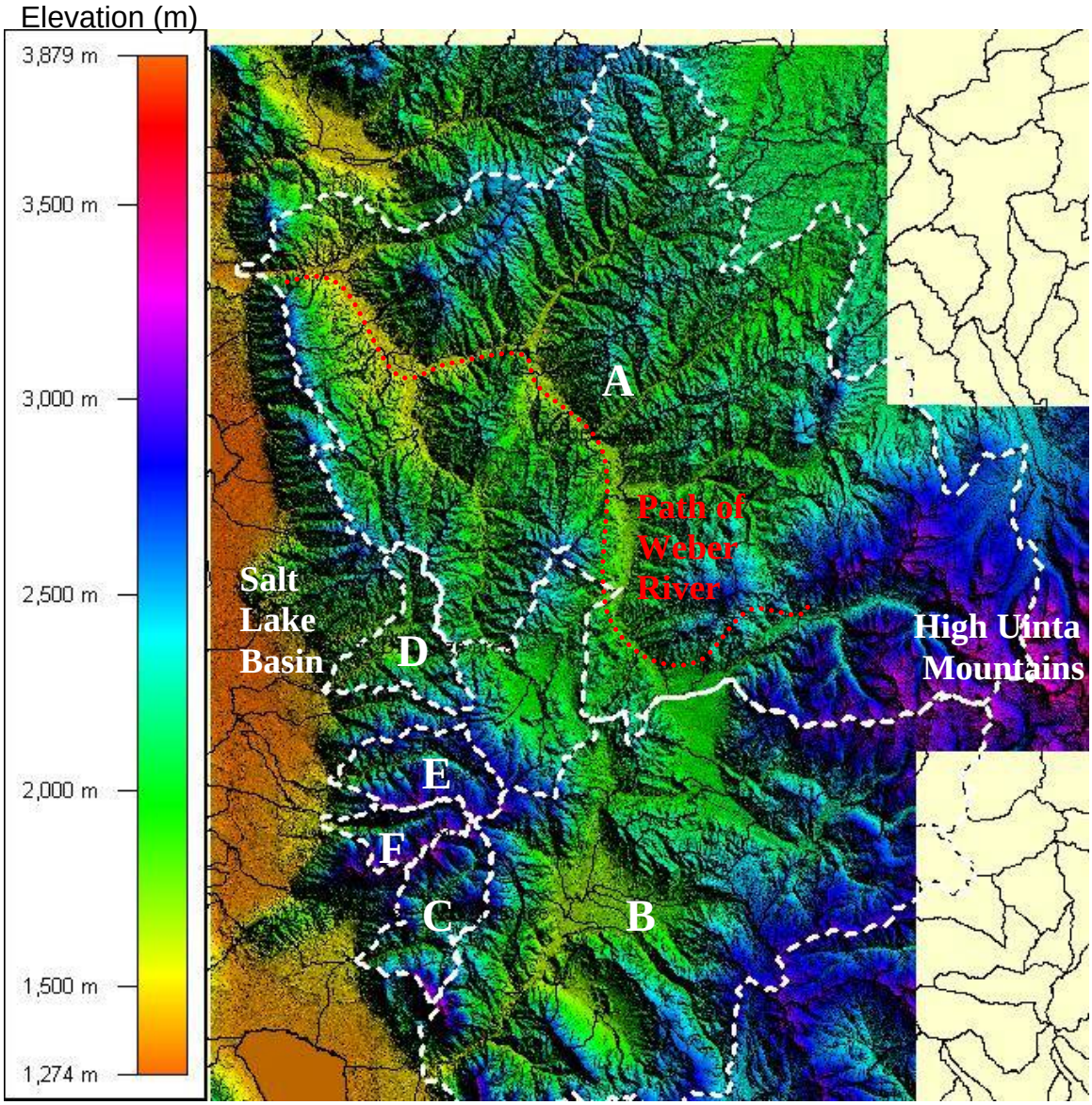

Fig. 2. Drainage basin areas bordering the Great Salt Lake Basin. (A) Weber, (B) Provo, (C) American Fork, (D) Parleys, (E) Big Cottonwood, and (F) Little Cottonwood Canyons. The color scale indicates terrain elevation in meters.

Table 1. Water drainage basin areas bordering the Great Salt Lake Basin. The names of surface weather stations within each basin is listed.

Basin	Approximate Drainage Area km^2 (mi^2)	Map Symbol	Station
Weber	4212 (1627)	A	PWR
Provo	1942 (750)	B	UTPCY
Spanish Fork	1683 (650)	Not shown	RDN
American Fork	155 (60)	C	PGRU1
Parleys	135 (52)	D	UTQRY
Big Cottonwood	129 (50)	E	N/A
Little Cottonwood	71 (27.4)	F	N/A

autocorrelated raster digital elevation model (DEM) data from the State of Utah GIS portal were used in conjunction with hydrological unit data from the USDA NRCS Geospatial Data Gateway to outline and measure drainage areas. The airshed area is analogous to the watershed area and can be thought of as the area of the drainage basin surface over which air resides. The airshed area is an important factor affecting both daytime surface heating and nighttime surface cooling and influences the atmospheric boundary layer through exchanges of sensible and latent heat fluxes as well as radiational heating and cooling. Hydrostatic forces cause air to flow down the topographic gradient during nighttime drainage periods. Other mechanisms such as advection also play a role in the supply and removal of air in a drainage basin depending upon the stability of the atmosphere and the synoptic conditions. This thesis focuses mainly on the Weber Canyon drainage basin, but first the flow properties of this and several canyons are studied to

understand if similarities and differences exist in the wind characteristics inside the canyons.

Wind characteristics of canyons during September 2010

Data from surface weather stations were analyzed to determine the flow characteristics within each of the canyons. The location of each of the stations is shown in Fig. 3 with the exception of the Weber Canyon station. While the position of the station within each canyon could not be controlled to maintain consistency between the

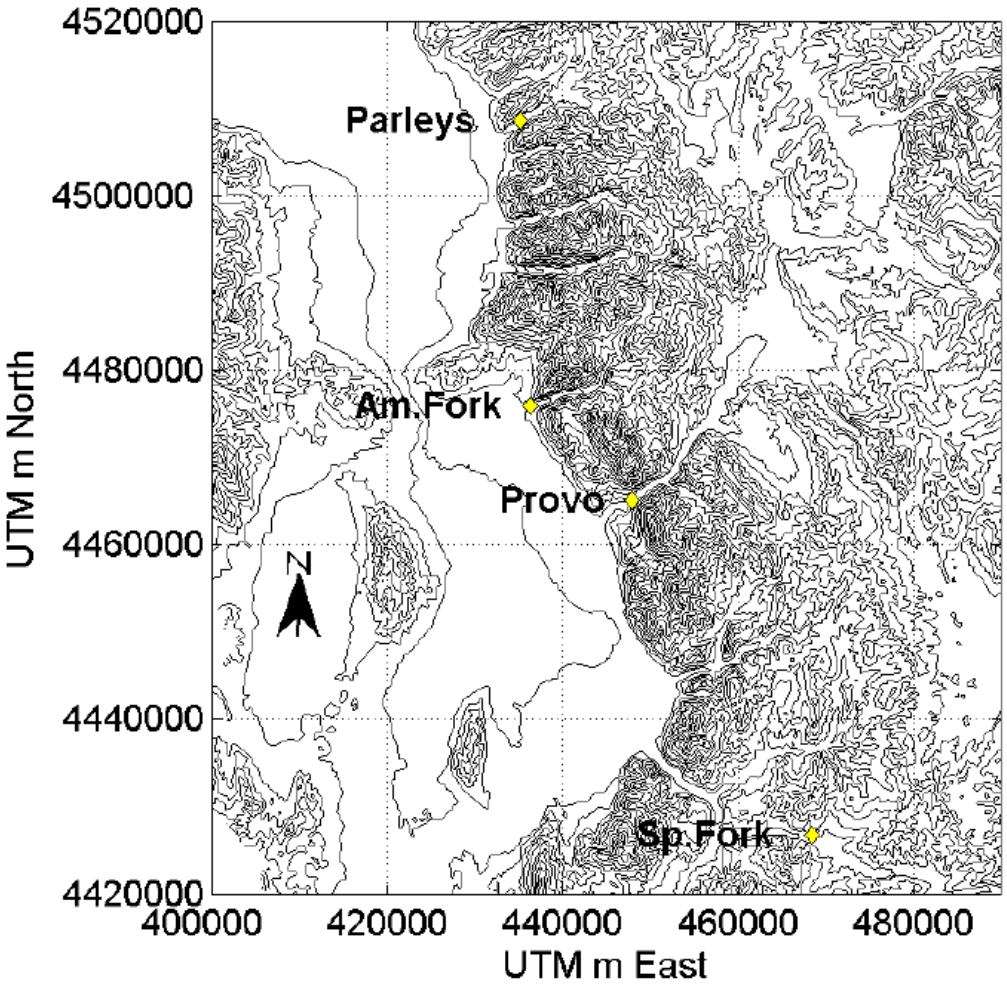

Fig. 3. Map of meteorological surface station locations within selected canyons of the Wasatch Mountains. The name of the weather station in each of the canyons is listed in Table. 1.

different canyons, most of the stations were located inside the canyon, approximately 1-2 km up-canyon from the exit. The outliers are the Spanish and American Fork stations; the Spanish Fork station is located in the upper drainage basin and the American Fork station is located at the exit region of the canyon where it meets the GSLB and is therefore more strongly influenced by the larger GSLB circulations.

Average diurnal patterns of wind speed, wind direction and temperature at the selected canyons during the month of September 2010 are shown in Fig. 4. September was chosen because diurnal temperature contrasts are large and outflow strength is a maximum during this month. Winds inside all of the canyons blow down-canyon during the night and up-canyon during the day. The transition to up-canyon flow following sunrise takes much longer inside the canyons that are associated with a larger drainage basin such as the Weber and Provo. In Weber Canyon, for example, canyon outflow persisted until past noon. Nighttime flow strength in the larger Weber and Provo drainage basins is greater than in the smaller drainage basins, suggesting a relationship between drainage basin size and nighttime flow strength. Other factors such as the small-scale details of canyon and basin geometry and the rate of air mass cooling and cold air buildup east of the canyons are also believed to influence the flow strengths. In contrast, there is less variation in flow strength among the drainage basins during anabatic or up-canyon winds as seen in Fig. 4.

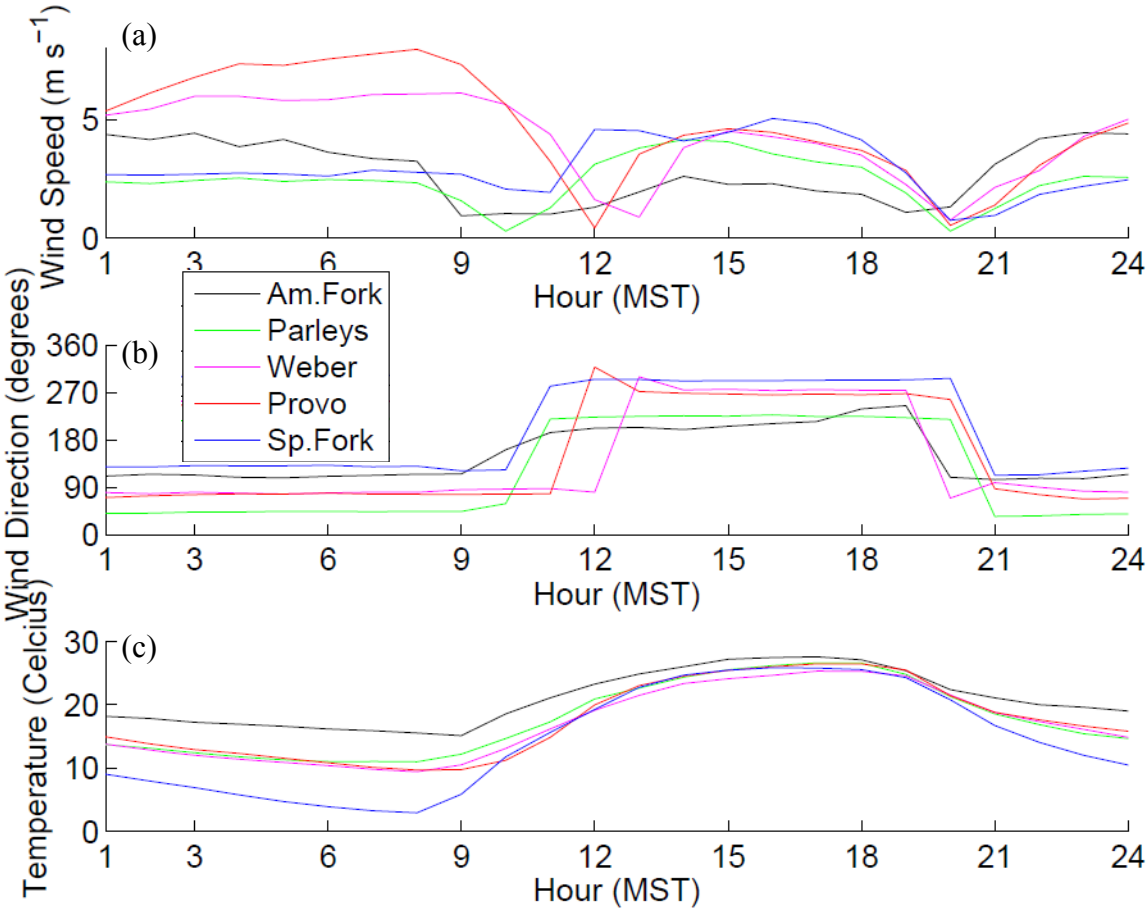

Fig. 4. Average diurnal (a) wind speed, (b) wind direction, and (c) temperature during September 2010 from surface stations within selected canyons of the Wasatch Mountains.

CHAPTER 3

FIELD EXPERIMENT DESIGN AND INSTRUMENTATION

A measurement campaign was designed to gather data that could be used to help understand the seasonal, diurnal and spatial characteristics of winds at the exit of Weber Canyon as well as the mechanisms responsible for producing the strong exit jet. This thesis research uniquely combines many meteorological data sources including existing automatic weather stations, measurement equipment borrowed from several generous parties, and equipment owned by the University of Utah's Atmospheric Sciences department. The location of the measurement area is denoted as a box in Fig. 5 and a map of measurement locations is provided in Fig. 6. Fig. 5 also displays surface meteorological stations that were used in the analysis. Long-term data came from two sources: (1) ten years of data were acquired from the PWR surface meteorological station located within Weber Canyon that is operated by the Utah Department of Transportation (UDOT) and; (2) a 50-m-tall meteorological tower operated by the State of Utah anemometer loan program provided a 12-month record of wind data at the exit region. A three month field study provided additional high resolution time and space measurements to better determine spatial and diurnal wind conditions as well as causal mechanisms of the jet formation. A pulsed Doppler Sonic Detection And Ranging (SoDAR) instrument was operated at the exit of Weber Canyon during the three-month general observation period (GOP) of July-September 2010 to continuously monitor exit wind profiles. The

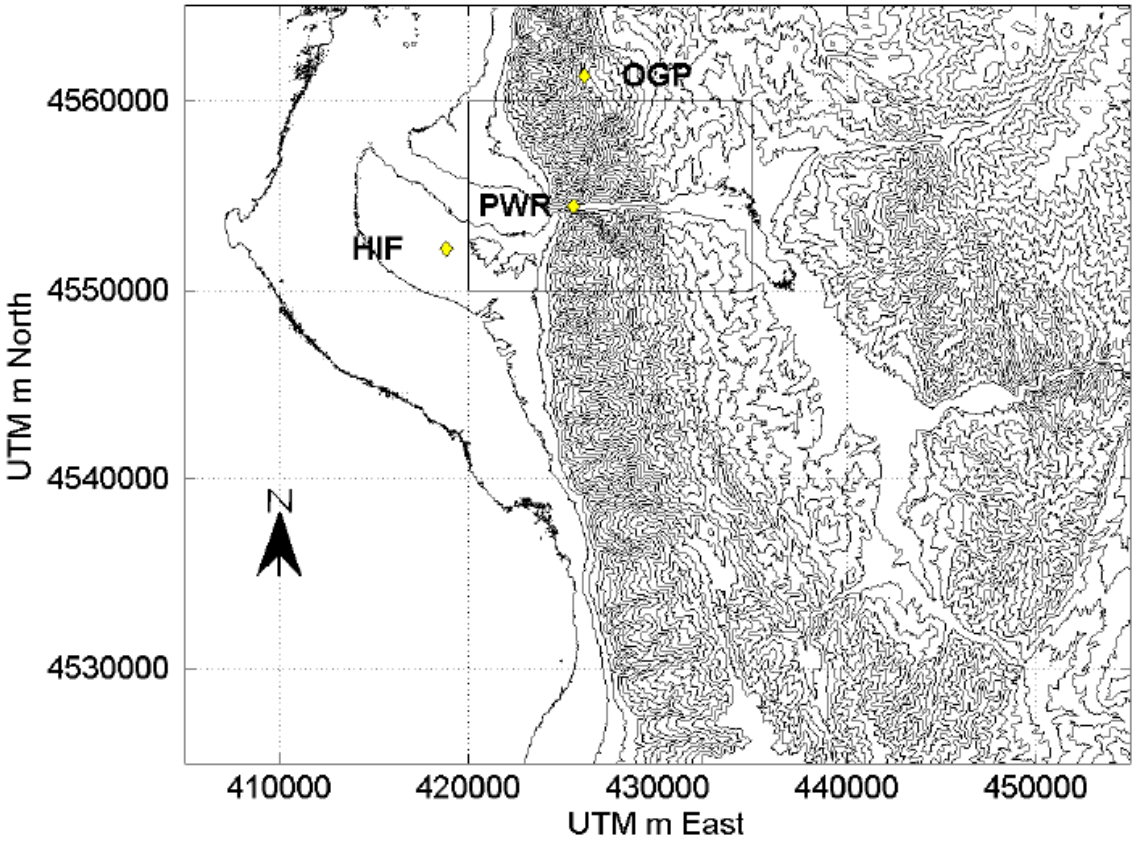

Fig. 5. Topography of Weber Canyon. Contour lines are displayed every 100 m. The names of existing surface stations used in the analysis are shown in bold print. The rectangle denotes the high density measurement area shown in Fig. 6.

presence of jets at the exit of the canyon was believed to be strongest during this time of year. During the GOP the objective was to document the highly consistent pattern of nighttime exit-jet formation. During the GOP, 75 of 90 nights (83%) displayed strong exit-jet outflow.

Four overnight IOPs were conducted during the GOP to collect additional detailed measurements within and at the exit of the canyon. The IOPs took place in late September and early October 2010. Table 2 shows information about each IOP and Fig. 7 provides a timeline of the measurements. The objective during IOPs was to observe how

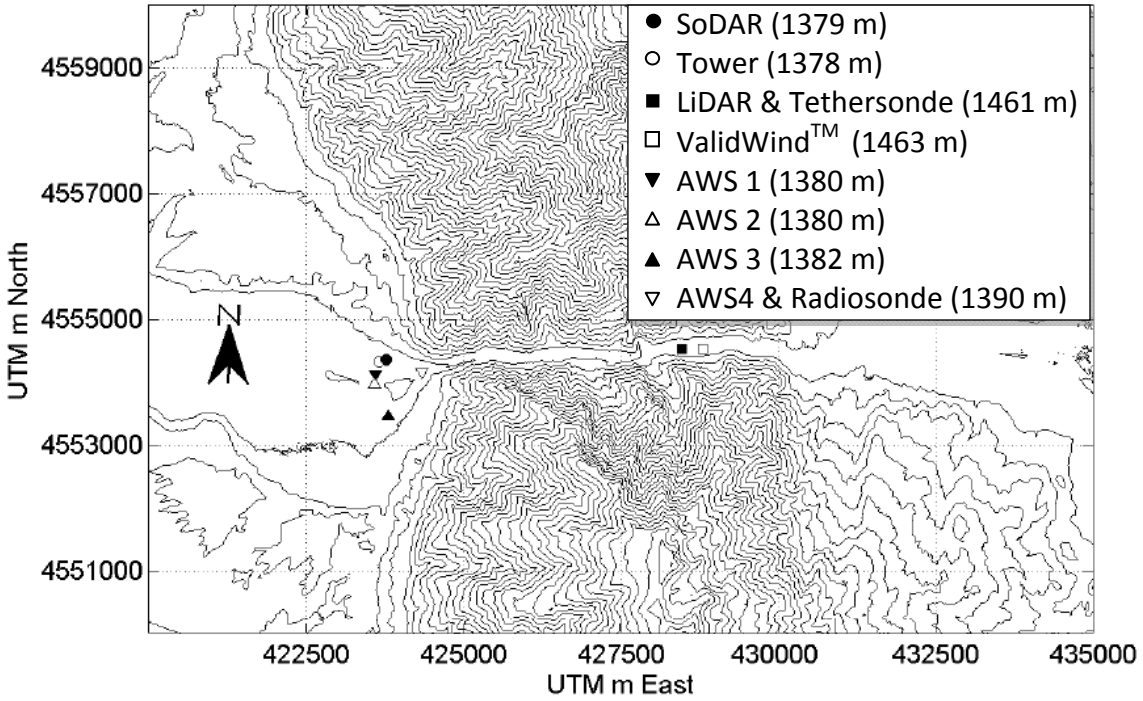

Fig. 6. High density measurement area and topography of the lower section of Weber Canyon. Contour lines are displayed every 50 m. The symbols denote measurement locations, as listed in the legend. The UTM zone is 12T. Station elevations in meters are shown in the legend.

wind and temperature profiles evolved from within the canyon to the exit during strong nighttime canyon flow. The IOP dates were chosen on the basis of weather forecasts and knowledge obtained about flow development from previous nights during the GOP. The weather conditions sought were high pressure, clear skies, weak synoptic pressure gradients and light background winds. These conditions are conducive to the development of localized thermally driven flows. As expected, on all four IOP nights strong outflow jets were observed at the exit of Weber Canyon.

A pulsed Doppler WINDCUBE® LiDAR (Light Detection And Ranging) measured wind speed profiles within the canyon for three weeks over the course of the IOPs. The WINDCUBE® was chosen for its narrow beam geometry and its ability to

Table 2. IOP information.

	Date of 2010	**Number of rawinsonde launches**	**Number of tethersonde ascents**	**Number of ValidWind™ launches**
IOP1	18-19 Sep	0	18	-
IOP2	24-25 Sep	7	21	6
IOP3	28-29 Sep	7	21	-
IOP4	30-01 Oct	7	21	28

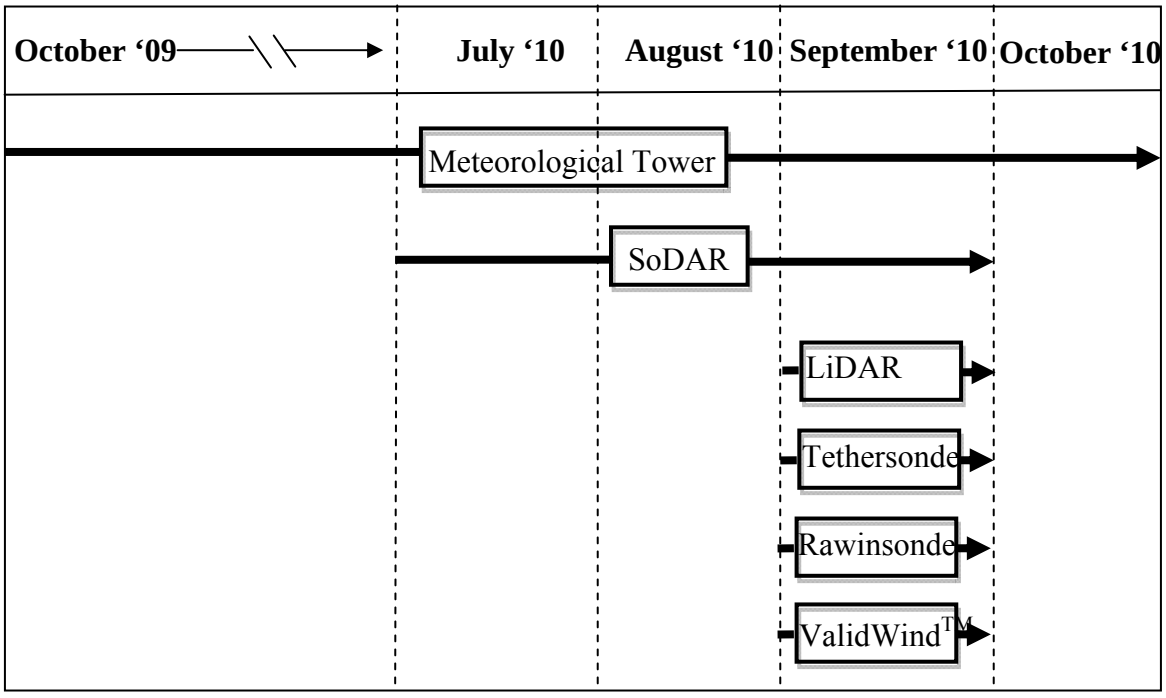

Fig 7. Measurements timeline.

capture wind profiles continuously within the canyon without interference from canyon walls and other flow obstructions. During IOPs, tethersonde and rawinsonde systems were used to measure temperature profiles within and at the exit of the canyon, respectively. The following sections describe each measurement system in more detail.

Meteorological tower

An NRG Systems 50 m meteorological tower was installed in October 2009 by the State of Utah anemometer loan program to assess whether the Weber Canyon exit region is suitable for large scale commercial wind energy generation. Data from the tower were used to understand the longer term wind climatology at the Weber Canyon exit region and to compare with SoDAR observations during the GOP. The tower is equipped with multiple levels of anemometry to observe vertical wind shear. The configuration of the tower sensors is shown in Table 3. The sensors are mounted on booms to minimize flow distortion impacts from the cylindrical tower. Ideally, the booms should be oriented such that they are at an angle of ±45º from the prevailing wind direction, based on potential flow theory around a cylinder (IEA 2003). Considering the prevailing E-W wind directions the boom orientations are considered acceptable.

Automatic weather station arc

Automatic weather stations (marked as AWS 1-5) were placed in an approximate arc at the exit of the canyon to measure the spatial variation of exit region surface wind characteristics during the GOP. The meteorological sensors and data loggers for each of the AWSes are listed in Table 4. A photograph of a typical AWS is shown in Fig.8. The AWSes were configured to record 10-minute-average values of near-surface wind speed,

Table 3. Meteorological tower instruments description. The tower has operated from October 2009 to the present.

	Type	**Height (meters)**	**Boom Orientation from True N**
Tower 0923	NRG 50 m	50.0 m	N/A
Anemometer 1	NRG#40	50.0 m	192º
Anemometer 2	NRG #40	50.0 m	20º
Anemometer 3	NRG #40	30.0 m	192º
Anemometer 4	NRG#40	10.0 m	20º
Anemometer 5	NRG #40C	3.0 m	20º
Wind Vane 1	NRG #200p	45.0 m	0º
Wind Vane 2	NRG #200p	45.0 m	102º
Temperature 1	NRG #110s	3.0 m	0º

Table 4. Automated weather station configuration information.

3 m Automated Weather Station Configuration	
Data Logger	Campbell Scientific CR1000
Anemometer	RM Young wind monitor 05103
Wind Vane	RM Young wind monitor 05103
Temperature & RH	Campbell Scientific CS500
Pressure	Vaisala PTB101B

Fig. 8. Photograph of one of the five automatic weather stations used in the experiments.

wind direction, temperature,relative humidity, and pressure. A 3 m anemometer installed at the meteorological tower was designated AWS 5.

SoDAR

An Atmospheric Systems Corporation (ASC) pulsed Doppler mini-SoDAR was used to measure continuous wind profiles up to 200 m above ground at the exit region. The SoDAR unit was powered by a solar panel/battery charging system. This allowed the SoDAR to operate continuously during the measurement period at a location where no grid power was available. Low relative humidity and high wind speeds during strong nighttime exit jets led to signal attenuation that generally limited measurement heights to ~140 m. The SoDAR was sited 100 m up-canyon from the tower and 750 m down-canyon from the valley exit. A digital level was used to ensure that the SoDAR antenna was horizontal. The SoDAR was set to record 10 min. data averages. Table 5 lists

Table 5. SoDAR operational settings.

Machine Type	Atmospheric Systems Corp. miniSoDAR
Orientation relative to true N	92º
Transmit Frequency	4500 Hz
Pulse length/Output level	60 ms/100%
Range/First/Interval	200 m/20 m/10 m

SoDAR operational settings and Fig. 9 shows the SoDAR site up-canyon from the tower. Due to space constraints, the SoDAR was installed only about 25 m from a semi major highway and 50 m from a railway line that runs through the canyon. Due to ambient noise sources from the highway and railroad there was concern that the SoDAR measurements would be contaminated by acoustic noise. Data post processing, however, showed that ambient noise sources did not appear to contaminate the SoDAR signal. SoDAR and tower wind speeds are compared in the following section as a quality control check on these two data sets.

The SoDAR operates by issuing three acoustic pulses, one directed vertically and the other two at a small beam angle θ from vertical and in directions that are orthogonal to each other as in shown in Fig. 10. The acoustic signals are scattered by turbulent refractive index changes and are received by the SoDAR transmitting antenna. Signal processing algorithms are used to extract the most probable wind speed distribution from the frequency shift in the returned acoustic signal from the three beams. The resultant wind speed at each level is a vector average of the three sample beams.

Fig. 9. Photograph of the SoDAR location up-canyon from the meteorological tower.

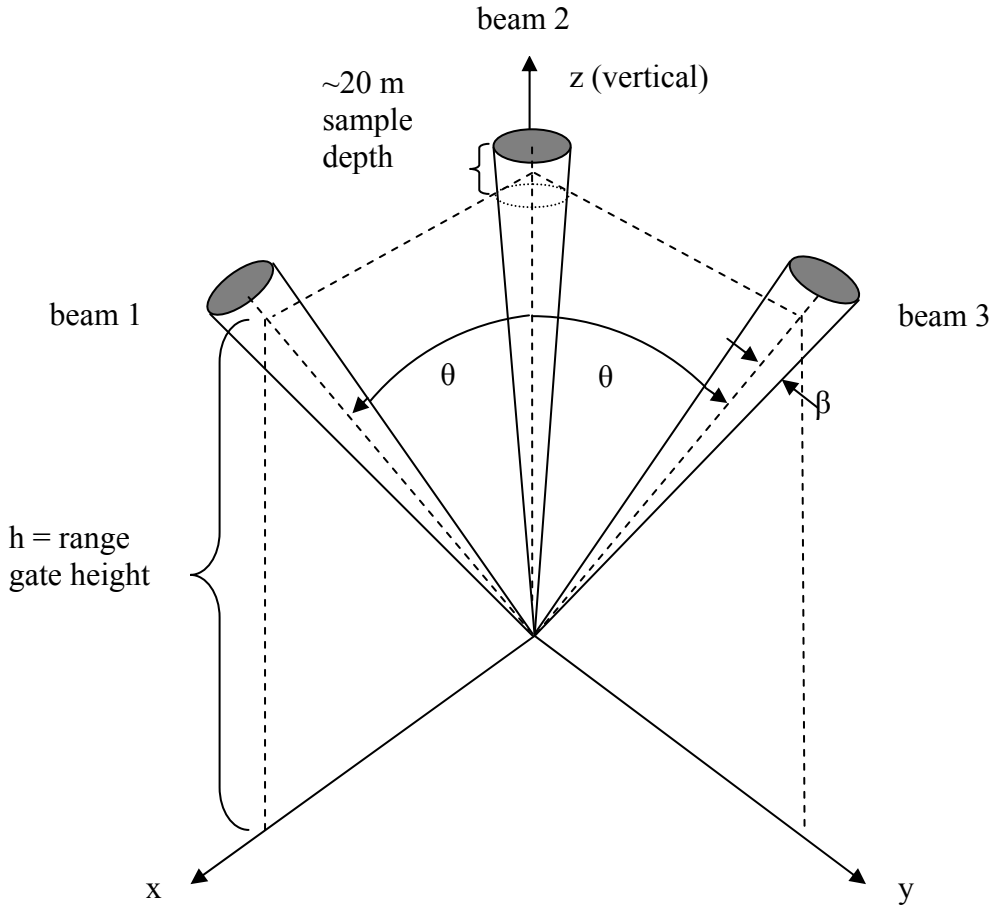

Fig. 10. Schematic of SoDAR sample beams. At each range gate height h, the SoDAR samples from a depth of ~20 m. The sample volume increases with height due to an increasing beam width β (adapted from Antoniou et al. (2003)).

At each measurement height h the SoDAR samples from an approximately 20 m deep volume that, because it is conically shaped due to an increasing beam width β, increases with height. The 20 m range gate length of the instrument is determined by the product of the pulse duration and the speed of sound. Range gates are centered every 10 m and therefore adjacent range gates overlap. Antoniou et al. (2003) describe in detail the operating principles of the SoDAR.

SoDAR vs. tower comparison

Comparing SoDAR and tower based wind measurements can serve to validate the two data sets and help to elucidate measurement problems during an observational campaign. The SoDAR and tower calculate wind speeds based on different methods; as described, the SoDAR measures and calculates a volume-averaged vector wind speed based on acoustic principles (Crescenti 1997) and the tower measures an in situ scalar wind speed using cup anemometers. Therefore the SoDAR is considered a remote sensing device, while standard anemometers are in situ mechanical devices with signal responses determined by their inertial characteristics. Differences have been observed between SoDAR and cup anemometer derived wind speeds especially during high wind speeds and events with significant vertical wind speeds that often occur in complex terrain. Following Crescenti (1997), common comparison statistics used to evaluate wind speed differences using the two methods are bias B (systematic errors), root mean squared error ($RMSE$), and coefficient of determination (r^2). The coefficient of determination is a simple linear regression that fits a line between the SoDAR and tower data and minimizes the sum of the squared residuals between the data points and the fit line. Statistics are calculated using Eq. (1)-(3) below.

$$B = \frac{1}{N}\sum_{i=1}^{N}(Y_i - X_i) \tag{1}$$

$$RMSE = \left[\frac{1}{N}\sum_{i=1}^{N}(Y_i - X_i)^2\right]^{\frac{1}{2}} \tag{2}$$

$$r^2 = 1 - \frac{\frac{1}{N}\sum_{i=1}^{N}(Y_i - X_i)^2}{\frac{1}{N}\sum_{i=1}^{N}(Y_i - \overline{Y})^2} \quad (3)$$

Y_i and X_i are the i^{th} observations from the SoDAR and reference instrument, respectively and N is the sample size. This method is used to compute statistics based on differences between the two measurement methods and therefore does not determine the "true value" of either measurement. Other calibration methods would have to be applied to determine the true measurement bias. Comparison statistics were calculated between the SoDAR and tower at a height of 50 m over a two week period when IOPs were conducted. Fig. 11 shows the results of the linear regression and Table 6 lists the computed comparison statistics. Shown in Fig. 12 are time series of wind speed and wind direction from the SoDAR and tower. It is evident from Figs. 11 and 12 that the greatest observed differences between the SoDAR and tower occur at nighttime when wind speeds exceed 15 m s^{-1}. The SoDAR may not be adequately capturing the wind speed because the signal gets blown away at extremely high wind speeds as documented by Crescenti (1997). Alternatively, these differences could be caused by anemometer overspeeding caused by large vertical wind speed components or by the inertia of the cup anemometer. Overspeeding of cups due to off-horizontal winds is a likely problem since during high wind events strong downward or negative wind speed components on the order of 2 m s^{-1} may occur at the valley exit. In this situation there can be significant overspeeding of the model #40c anemometer (Pederson 2001).

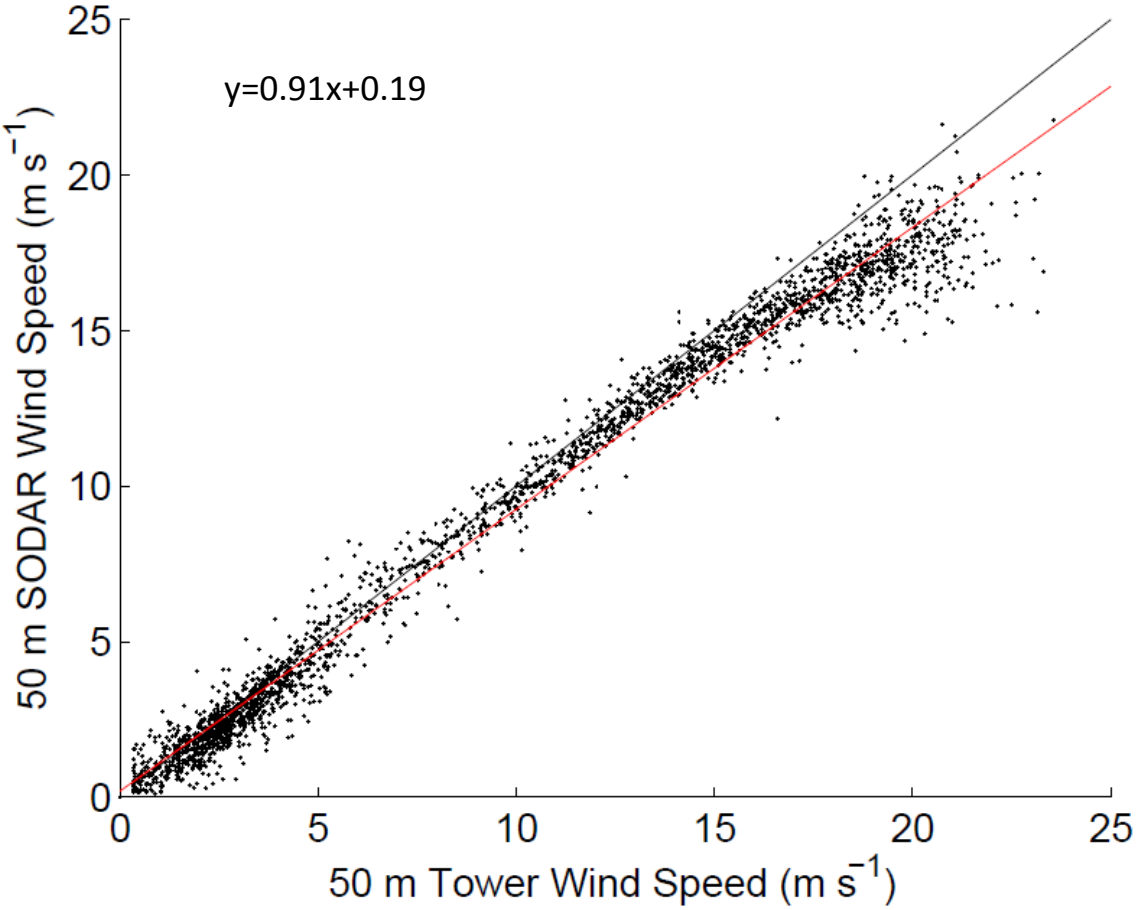

Fig. 11. Linear correlation between SoDAR and tower derived wind speeds at 50 m above ground. The 1:1 line is plotted in black and a linear fit of the data is plotted in red with the fit equation shown in the upper left.

Table 6. Comparison statistics between the SoDAR and tower at 50 m during the 2-week period shown in Fig. 12.

50 m Comparison	**Bias *B* (m s^{-1})**	***RMSE*** **(m s^{-1})**	***r*^{2}**
Wind Speed (SoDAR-TOWER)	-0.73	1.28	0.96
Wind Direction (SoDAR-TOWER)	0.36	31.2	0.88

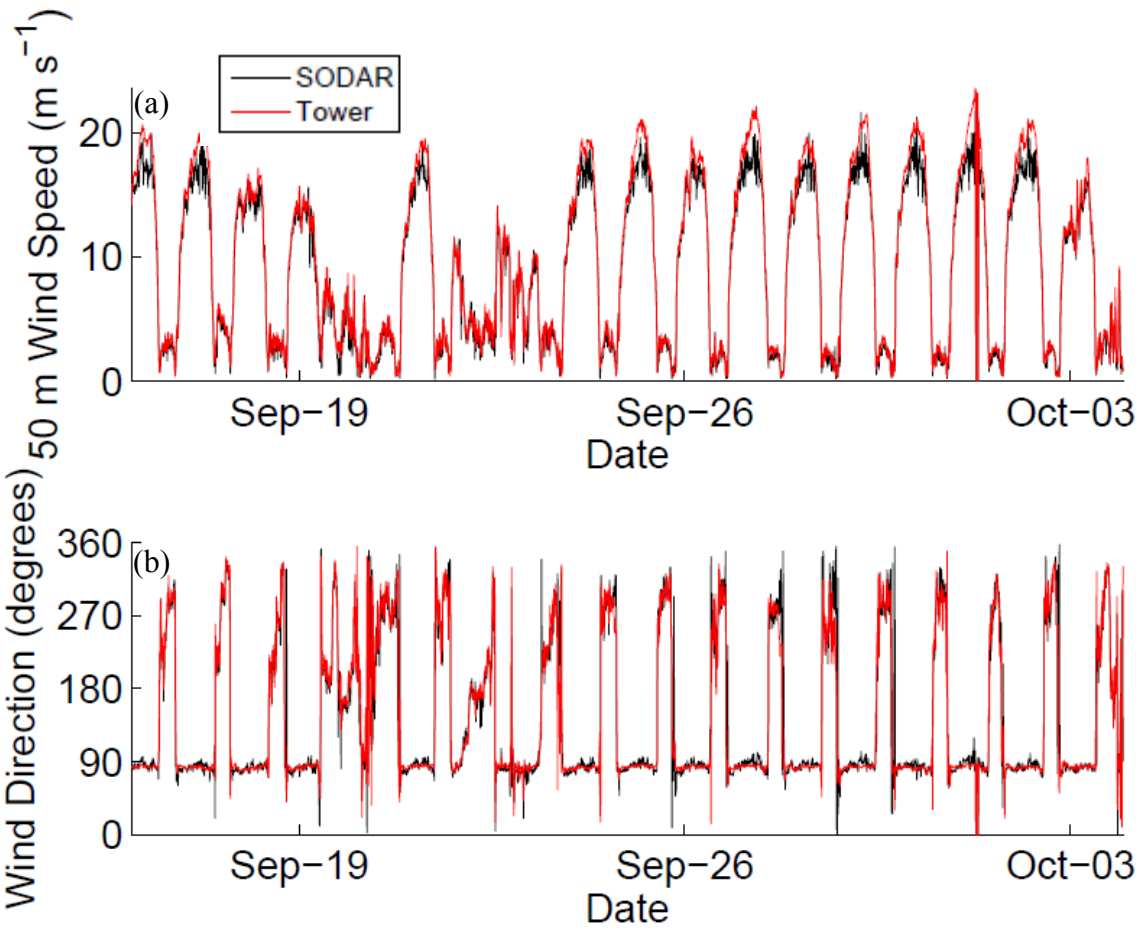

Fig. 12. Time series of SoDAR and tower measurements at 50 m above ground during the 2 week period when IOPs were conducted. Displayed is (a) wind speed, and (b) direction.

Crescenti (1997) computed comparison statistics based on a composite data set of SoDAR campaigns over the course of 20 years and calculated mean values of r^2 =0.91, B=-0.05 m s^{-1}, $RMSE$=1.11 m s^{-1} for wind speed and r^2 =0.92, B=-0.5 m s^{-1}, $RMSE$=22.0 m s^{-1} for wind direction. Thus, the results shown in Table 6 correspond well with previously obtained results, but with slightly larger wind speed and direction biases for the reasons mentioned previously.

WINDCUBE® LiDAR

A pulsed Doppler WINDCUBE® v1 LiDAR, shown in Fig. 13, was used to measure wind speed and direction profiles within the canyon. The LiDAR had fewer operational limitations relative to the SoDAR and provided reliable measurements up to 200 m. Other measurement technologies were considered such as tethersonde systems, rawinsonde, and SoDAR, but LiDAR technology was deemed to be the most appropriate technology to obtain continuous wind speed profile measurements in a narrow canyon. NRG Systems, which is partnered with the French LiDAR manufacturer Leosphere, generously loaned the LiDAR unit to us for use in this project. The WINDCUBE® operated continuously with no operational issues during the entire time period. Onsite 120 V AC power was available and the unit was set to record 10-minute data averages based on a 1-s sampling rate. Fine and coarse adjustments knobs on the WINDCUBE® legs were used to level the machine with respect to horizontal and the unit was oriented to geographic true north. Table 7 displays the LiDAR operational settings.

The WINDCUBE® operates by issuing a sequence of laser pulses, one in each of the four cardinal directions at a beam angle α from the vertical. Approximately 20 m of the atmosphere is sampled along the radial beam centred at pre-programmed range gate heights. An algorithm is used to extract a wind distribution in each sample volume based on the shift in the frequency of the returned signal of the laser beam. A most probable wind speed is extracted from each wind distribution. The horizontal wind speed and direction at each range gate is then constructed trigonometrically from at least three of the four radial wind vectors at a given range gate (Lindelöw-Marsden 2009). Fig. 14 shows a schematic of the WINDCUBE® sample volume. h is the range gate height and $\alpha = 30^{\circ}$ is

Fig. 13. Photograph of the WINDCUBE® LiDAR in Weber Canyon.

the beam angle. The diameter of the circle along which sample volumes lie can be calculated using the equation $d = 2\ h\ \tan\alpha$ as shown in the figure. For example, at a height of 100 m, the diameter of the scan circle would be 115 m. Therefore, there is significant spatial separation of the sample volumes which could be a source of error in complex terrain where winds tend to be non-homogenous. Since it is a pulsed system, wind vectors are calculated at multiple heights simultaneously. A complete description of LiDAR measurement principles and uncertainty is provided by Lindelöw-Marsden (2009).

Table 7. LiDAR operational settings.

Machine Type	WINDCUBE® v1 LiDAR
Orientation relative to true N	0º
Laser wavelength	1.55 µm
Range/First/# of heights	200 m/40 m/10

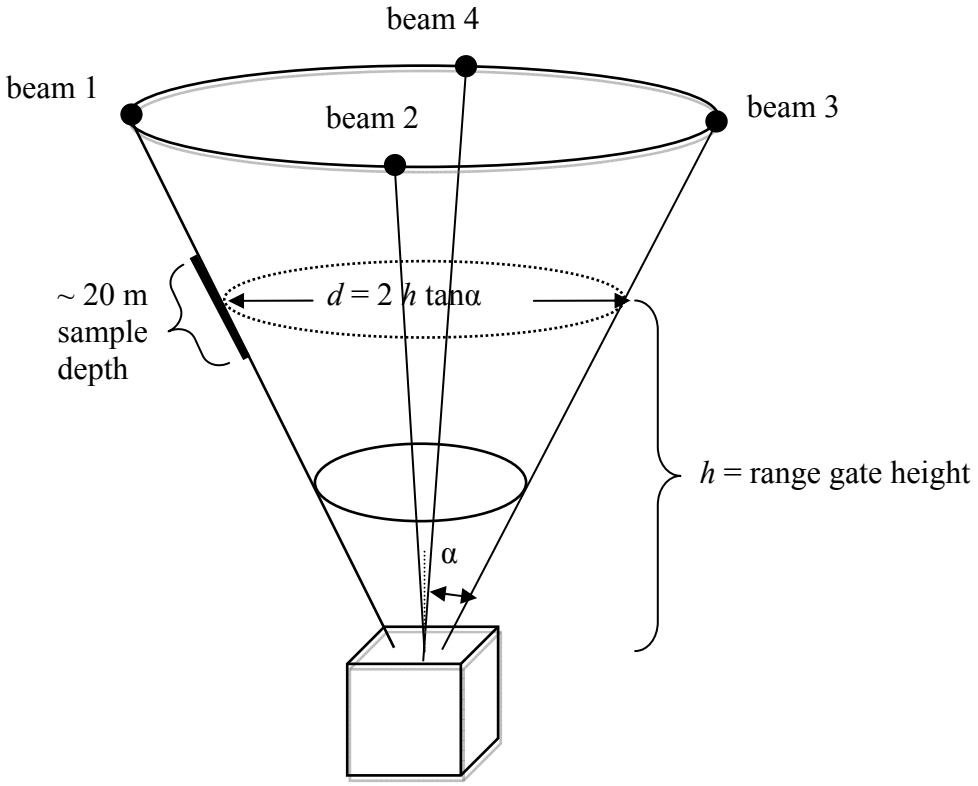

Fig. 14. Schematic of the LiDAR sampling volume, illustrating the beam geometry and a single range gate height h. (adapted from Lindelöw-Marsden 2009).

ValidWind™ balloon tracking system

A novel system developed at Utah State University was tested several times during the measurement campaign, including during one complete overnight IOP. The ValidWind™ system offers a new cost-effective method to determine wind profiles, trajectories and time series during meteorological experiments using laser balloon-tracking technology (Wilkerson et al. 2010). The main components of the system are show in Fig. 15. The ValidWind™ system, co-located with its balloon launching system was placed 0.3 km up-canyon from the WINDCUBE®. The ValidWind™ system is analogous to an optical theodolite balloon tracking system in which an optical theodolite measures elevation and azimuth angles between a ground location and an ascending balloon at known time increments. The optical theodolite technique can use single or multiple theodolites. In the case of a single theodolite, a constant rate of rise is assumed for the balloon and trigonometric relations are used to determine horizontal wind speed vectors between balloon sightings. The multiple theodolite technique eliminates the constant rate of rise assumption since the balloon's location, including altitude, can be determined by triangulation from two theodolites which are positioned some distance apart. A sequence of sightings determines how the balloon moves with time as it is carried by the wind. In comparison, the ValidWind™ system requires only a single ground station and uses a laser range finder coupled with a digital compass and inclinometer to measure range, azimuth and elevation angles, respectively. Balloon elevation is calculated trigonometrically from the range and elevation angle data. A computer measures time increments between measurements. Horizontal wind speed and

Fig. 15. Photograph of the ValidWind™ system from Utah State University.

direction can be calculated from the measurements. A sophisticated automated gimbal tracking system has been developed that automatically tracks a balloon and records the necessary trajectory information. ValidWind™ derived wind profiles were compared to profiles from the WINDCUBE® LiDAR during a 12 hour IOP to assess system performance.

ValidWind™ vs. WINDCUBE® comparison

Raw 1-second sampled data from the LiDAR was averaged over a two minute period corresponding to the approximate time period between the balloon launch and the

time to reach 200 m, which is the maximum range gate of the LiDAR. This short interval averaging was used to obtain more statistically representative wind profiles. The balloons traveled a very short distance down the canyon in the time interval required to reach 200 m. Data from ValidWind™ was interpolated onto the fixed measurement heights from the LiDAR for comparison. Concurrent wind speeds from the ValidWind™ and WINDCUBE® systems are plotted as a linear correlation in Fig. 16 and as wind profiles in Fig. 17. Despite the differences in measurement techniques, there is remarkable agreement between wind profiles derived from the two systems.

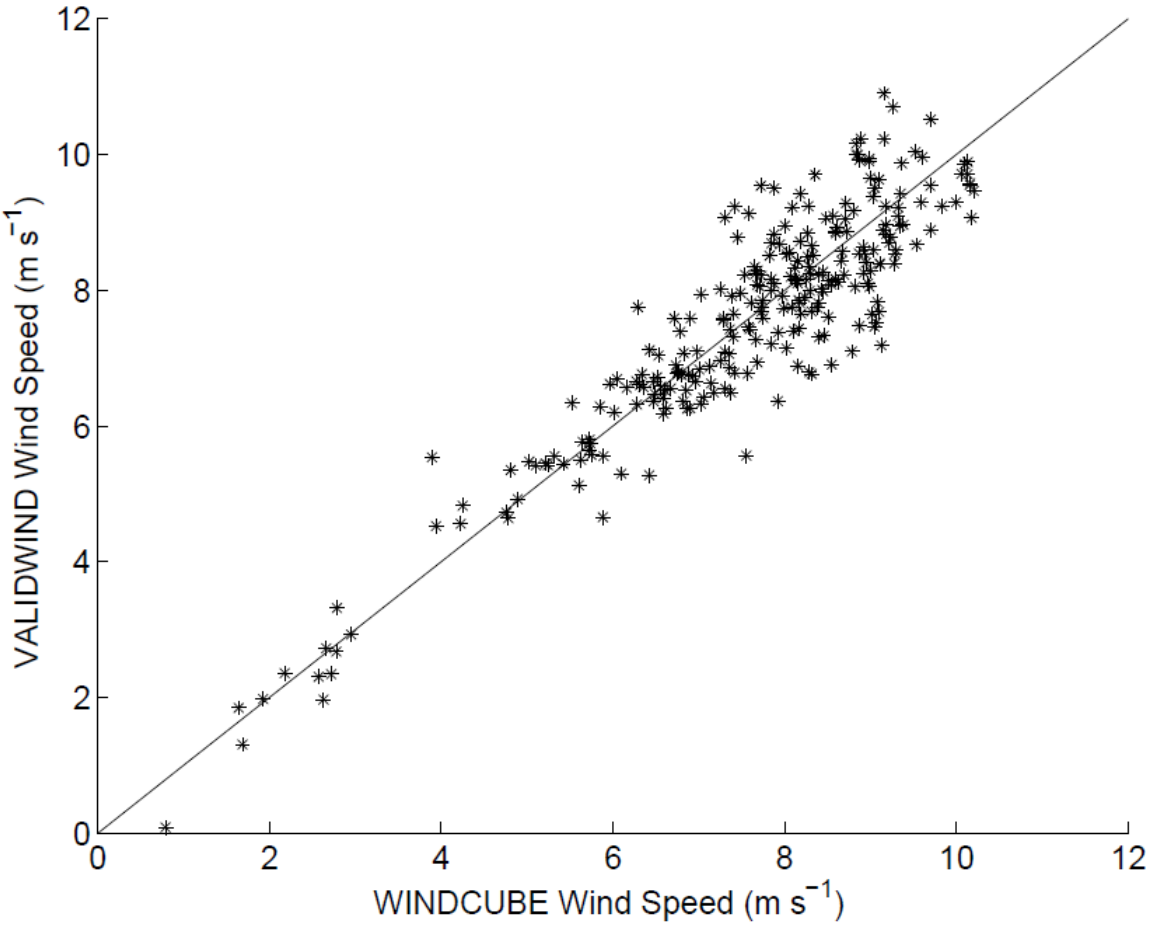

Fig. 16. Linear correlation between ValidWind™ and WINDCUBE® wind speed measurements for 28 balloon flights during IOP4. 1:1 line is shown in black.

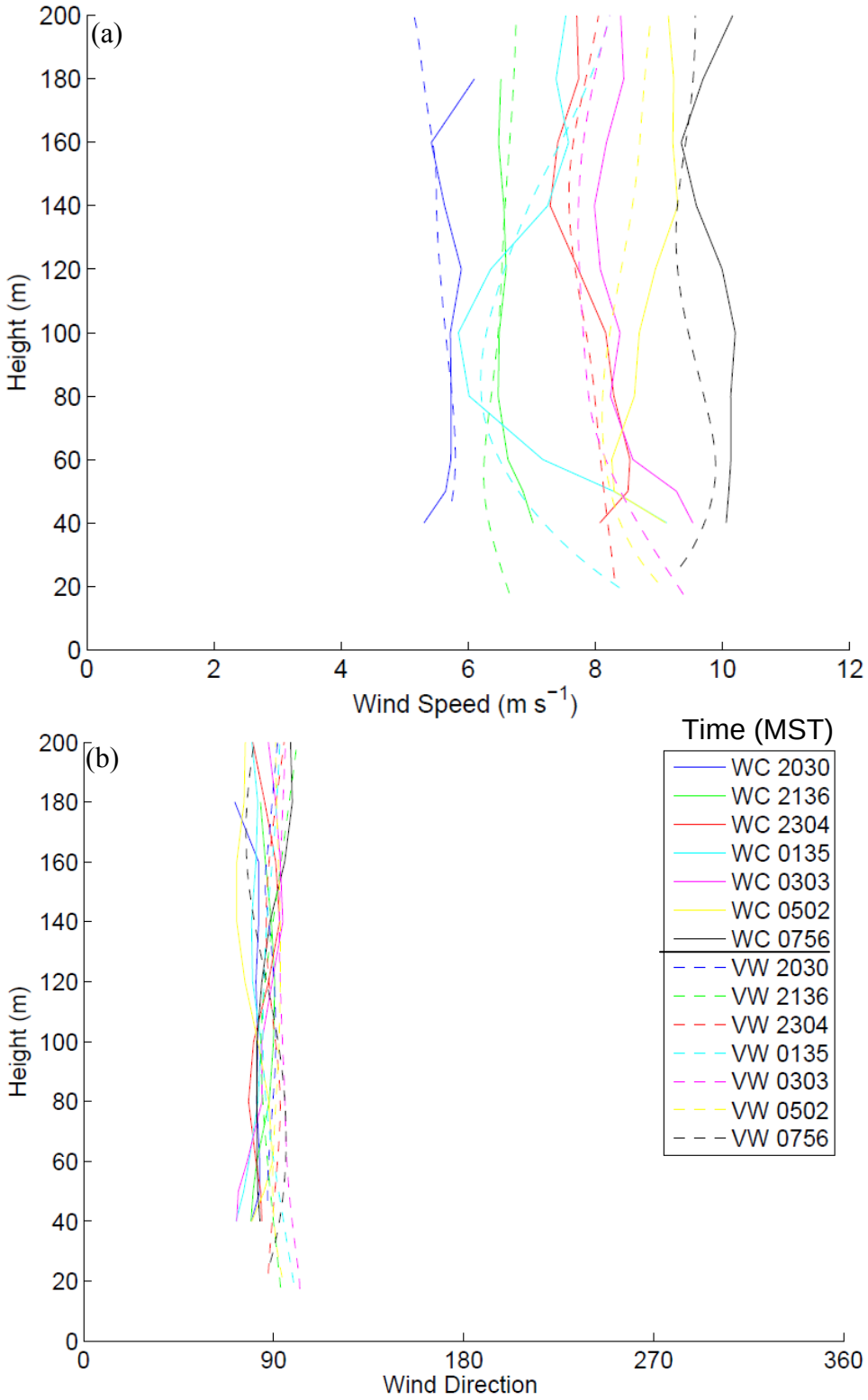

Fig. 17. ValidWind™ (VW) and WINDCUBE® (WC) profiles of (a) wind speed and (b) wind direction during IOP4. Times (MST) are shown in the legend.

Our validation of LiDAR and ValidWind™ derived wind profiles can be compared to validations of double theodolite balloon tracked wind measurements made by earlier investigators. Rider et al. (1966) compared tower measurements at 152 m (500 ft.) to theodolite derived measurements and determined that the mean error between the tower and theodolite measurements was 1.9 m s^{-1} (6.2 ft s^{-1}) for wind speed and 15.0º for wind direction and a nonlinear correlation was observed for wind speed. In light of these results the ValidWind™ system offers a significant improvement in balloon-based tracking technology.

Tethered balloon and rawinsonde launches

During IOPs a tethered balloon/sonde system and free flying rawinsondes were used to measure vertical profiles of temperature, pressure and relative humidity within the canyon and at the exit, respectively. The tethered system consisted of a blimp-shaped helium-filled meteorological balloon carrying a radiosonde manufactured by GRAW, a German company. The GRAW DFM-06 radiosonde was attached to the balloon using a mesh bag (Fig. 18). Both the tethered and free flying radiosondes transmitted meteorological data back to a GRAW GS-H high mobility ground station. The use of a tethered radiosonde was a low-cost solution to obtain frequent profile measurements in the canyon. The tethered balloon made vertical profiles through the canyon approximately every 30-60 minutes. Free flying GRAW DFM-06 radiosondes were launched at the canyon exit near AWS4 every three hours starting at 1700 MST. The GRAWmet software was used to process raw sounding files. Up-soundings were used in the analysis; down-soundings were discarded because the balloon was retrieved quickly to equilibrate the sonde at the ground to prepare for the next up-sounding. Geometric

Fig. 18. Photograph of the GRAW sonde attached to the helium-filled tethered balloon.

heights for the free flying radiosondes came from the onboard Global Positioning System (GPS). Geometric heights for the tethered radiosondes were calculated using virtual temperature and pressure measurements and the hypsometric equation.

Surface meteorological network

The MesoWest network as described by Horel et al. (2002) is a high density network of surface meteorological stations. The PWR station located within Weber Canyon, HIF (Hill Air Force Base) and the OGP station located on Ogden Peak were

used to gain an understanding of regional wind patterns during IOPs. The locations of these stations are shown in Fig. 5.

Description of the IOPs

Four IOP's were conducted during the GOP. During IOPs additional measurements were taken inside and at the exit of the canyon. IOPs were selected based on the forecast synoptic conditions. Clear skies, weak pressure gradients and light winds aloft were desired as these conditions were believed to be most conducive to the formation of local thermally driven circulations. Synoptic conditions for IOP 1 are visualized in Fig. 19a using a 700 mb upper air analysis chart from the National Climatic Data Center (NCDC). The synoptic conditions during IOP1 differed from the desired conditions, as a pressure gradient was oriented across Utah producing strong upper-level winds. Clear skies were present and, despite the strong upper-level winds, a shallow jet was still observed at the Weber Canyon Exit. IOPs 2-4 exhibited similar synoptic characteristics, with weak regional pressure gradients over Utah and lighter winds aloft. The IOP2 chart (Fig. 19b) will be used to represent the synoptic conditions during IOPs 2-4 since similar conditions existed during the three time periods. Because synoptic conditions were similar during IOPs 2-4 and minimal variation in the structure of the exit jet was observed, results in the rest of this thesis will not focus on a particular IOP, rather results are discussed from each IOP depending on the availability of other meteorological data.

(a) 700 mb analysis valid 12UTC Sep. 19 2010

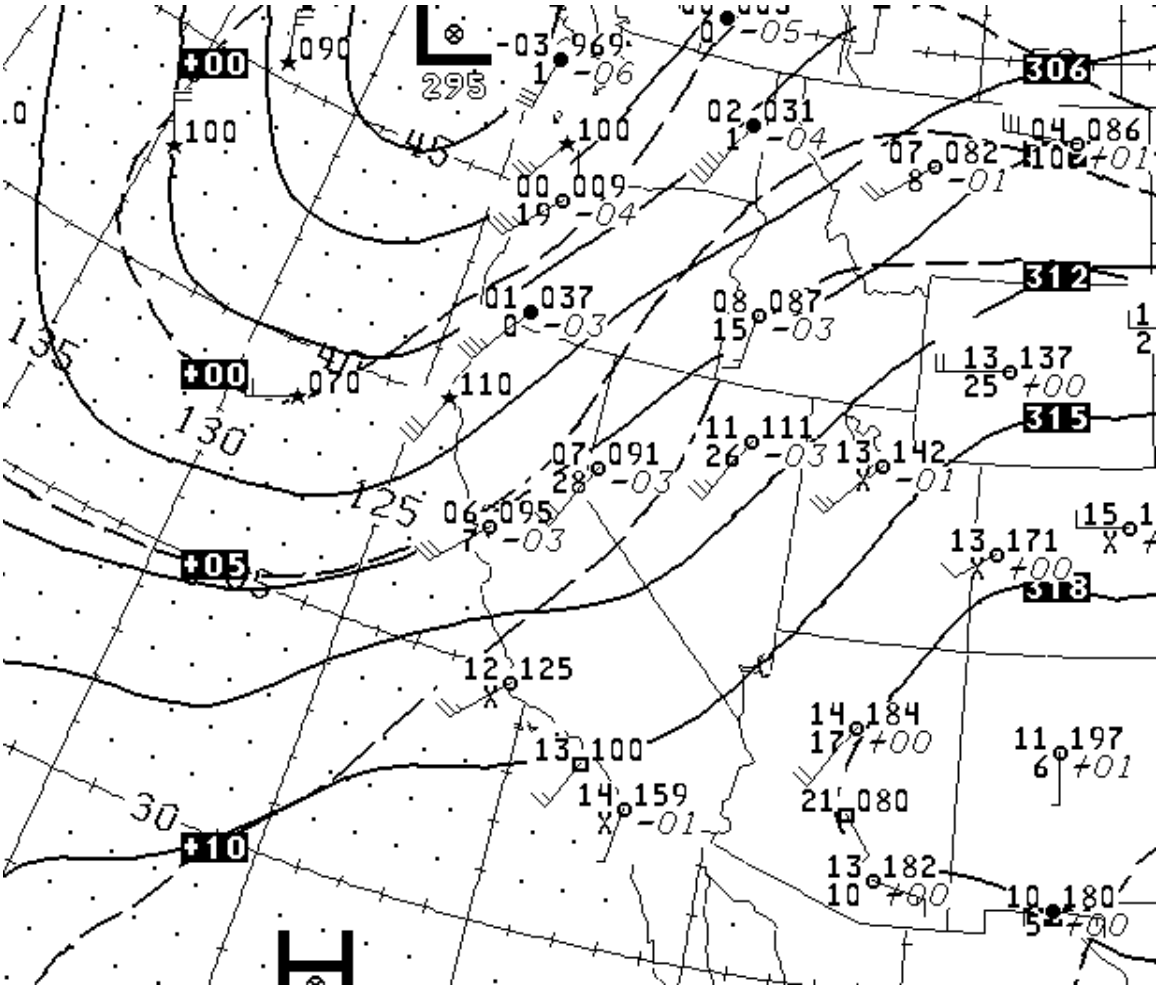

Fig. 19. 700 mb upper air analysis charts for IOPs 1 and 2. The 12 UTC (05 MST) charts shown correspond to early morning of the second day for each IOP. (a) IOP1 19 Sep.

(b) 700 mb analysis valid 12UTC Sep. 25 2010

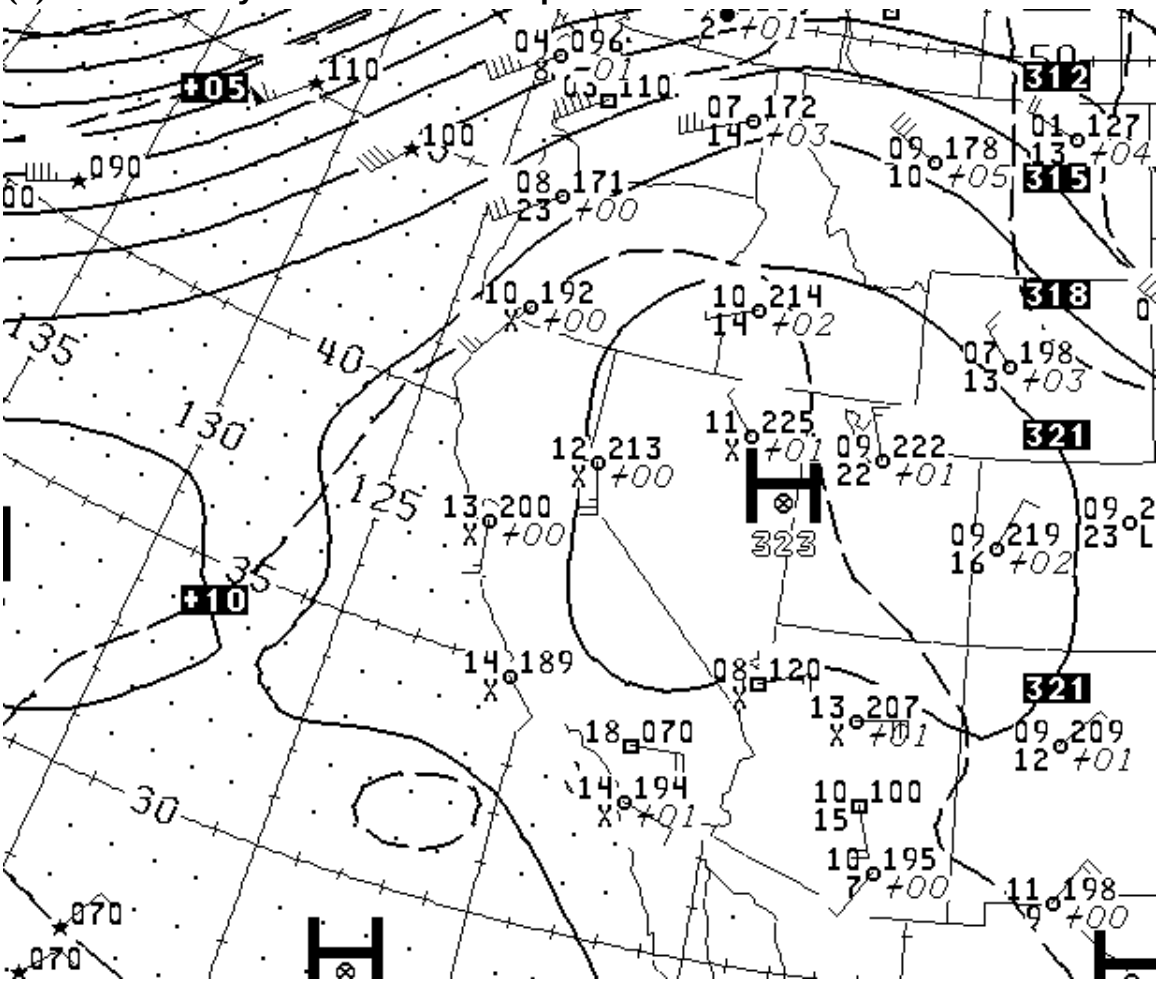

Fig. 19. continued. (b) IOP2 25 Sep.

CHAPTER 4

WIND FLOW CHARACTERISTICS OF WEBER CANYON

This chapter is focused on gaining an understanding of the temporal and spatial characteristics of the valley exit jet at Weber Canyon as well as the mechanisms that are responsible for producing it. Long-term and seasonal aspects will be discussed first followed by a discussion of shorter term and spatial phenomena.

Seasonal variations in atmospheric wind circulations were expected in Weber Canyon due to seasonal variations in insolation and large-scale synoptic conditions. To confirm this expectation, seasonal and annual wind characteristics were calculated using one year of data from the meteorological tower at the exit and 10 years of data from the PWR automatic weather station located 1 km up-canyon. Seasonal statistics based on a full year of tower data are compared to 10-year-average statistics from the weather station to gain a perspective on the long-term wind variability at the site.

Climatology of winds at the Weber Canyon exit

The prevailing winds at the exit of Weber canyon, as determined from the meteorological tower data, are easterly and directed in a down-canyon direction (Fig 20a). Down-canyon flow occurs almost 50% of the time and predominantly during nighttime. Westerly up-canyon flow occurs mostly during daytime but is much weaker and variable in direction. Wind speed frequencies exhibit a bimodal peak (Fig. 20b). The lower-speed peak is indicative of low daytime wind speeds, while the high-speed peak is

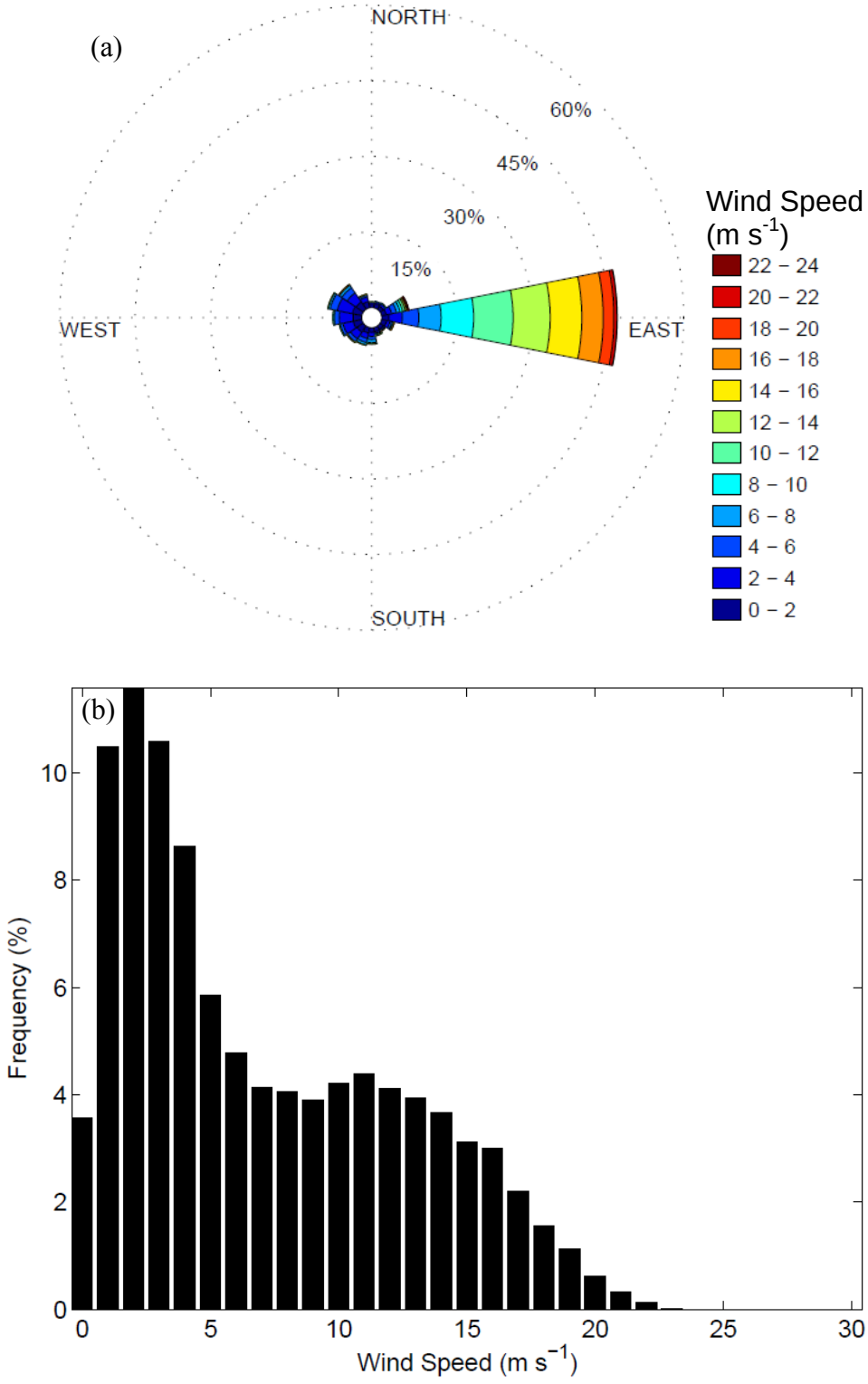

Fig. 20. Frequency distributions of (a) wind speed and (b) wind direction (wind rose) at 50 m on the meteorological tower at the exit of Weber Canyon. Color bands denote frequency of wind speeds in m s^{-1} as shown in the legend.

more indicative of strong easterly nightime flows (exit jets) coming out of the Weber Canyon exit.

Average wind speeds measured by the anemometers at different levels on the tower during the one-year period from October 2009 through September 2010 are shown in Fig. 21. Flows were strongest in the summer (June, July, August) and early fall, peaking in September. It will be shown that this is a consistent feature of the wind climate within the canyon as determined over the past 10 years. An interesting feature in Fig. 21 is on average the tendency for positive wind shear between the 30 and 50 m tower levels during summer months and negative wind shear during winter months suggesting that the height of the wind speed maximum of the jet varies seasonally.

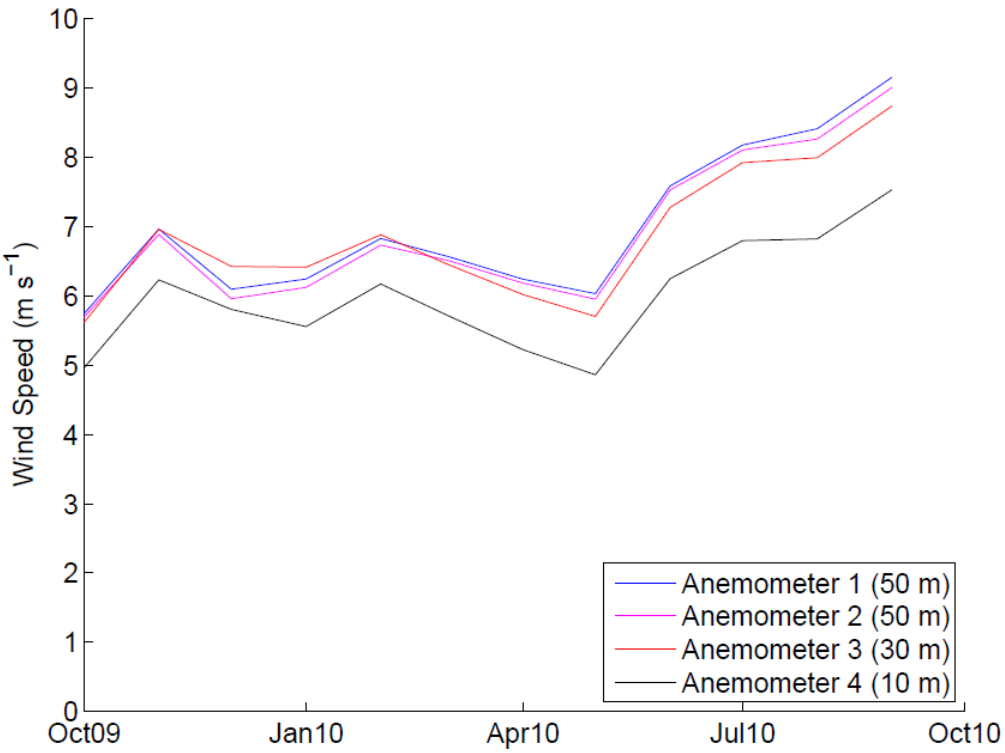

Fig. 21. Monthly wind speeds measured at the meteorological tower from October 2009 through September 2010.

Hourly and daily variations of wind speeds are displayed for the period from October 2009 through October 2010 in Fig. 22. The resulting pattern shows strong diurnal and seasonal variations. Katabatic winds are strongest and most consistent at night during the summer and fall. Winds are much weaker during the day, especially in mid-afternoon. Down-canyon flow duration varies seasonally and peaks in winter and fall. The duration is linked to the yearly course of sunrise times. In the case of Weber Canyon, the flow persists 5-6 hrs. after sunrise independent of the season. Up-canyon flow is strongest and most consistent during the daytime in spring.

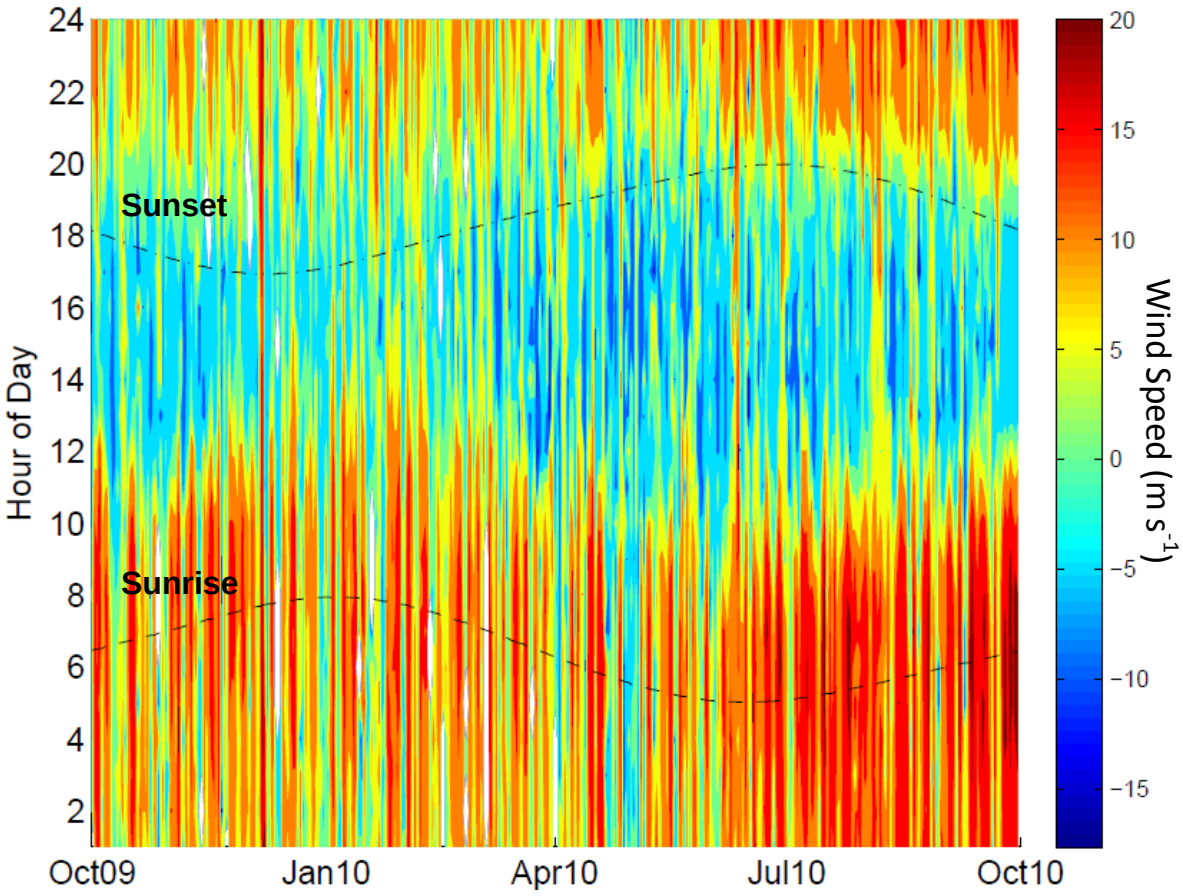

Fig. 22. Hourly and daily course of wind speeds for a 1-year period at the 50 m level of the meteorological tower. Positive (negative) wind speeds denote down-canyon (up-canyon) flow in m s^{-1}. Wind speeds are maximum 10-min wind speeds that occurred during each hour. Dashed lines indicate sunrise (bottom) and sunset (top) times in MST.

The PWR station provided 10 years of data from which interannual variations in flow strength within lower Weber Canyon could be determined. Mean monthly wind speeds for 10 years are shown in Fig. 23. Wind speeds are generally consistent from year to year and display similar seasonal trends with the strongest flows during the summer and early fall. This agrees well with measurements obtained on the meteorological tower at the valley exit during 2010 when flow strength also peaked in September. Overall the spread of the data is small, especially during the summer months. Thus, there is a high consistency in summertime thermally driven flows from year to year. Data quality issues were found in the 10 year dataset, reducing the number of available observations in some of the months. This has led to some erratic behaviour in the monthly wind speed trends during a few of the years in Fig.23.

The Weber Canyon exit jet

Overall conditions during the three-month GOP were conducive to katabatic canyon flow development with 75 of 90 nights (83%) displaying strong exit jet outflow as measured by the SoDAR. The only times when canyon flows were completely absent were during the passage of low pressure systems or frontal zones associated with increased cloud cover and precipitation. One of the main objectives of this thesis is to determine how the flow and temperature structure evolve from within the narrow part of the canyon to the exit region. In this section temperature and wind data are compared for the two locations during selected IOPs.

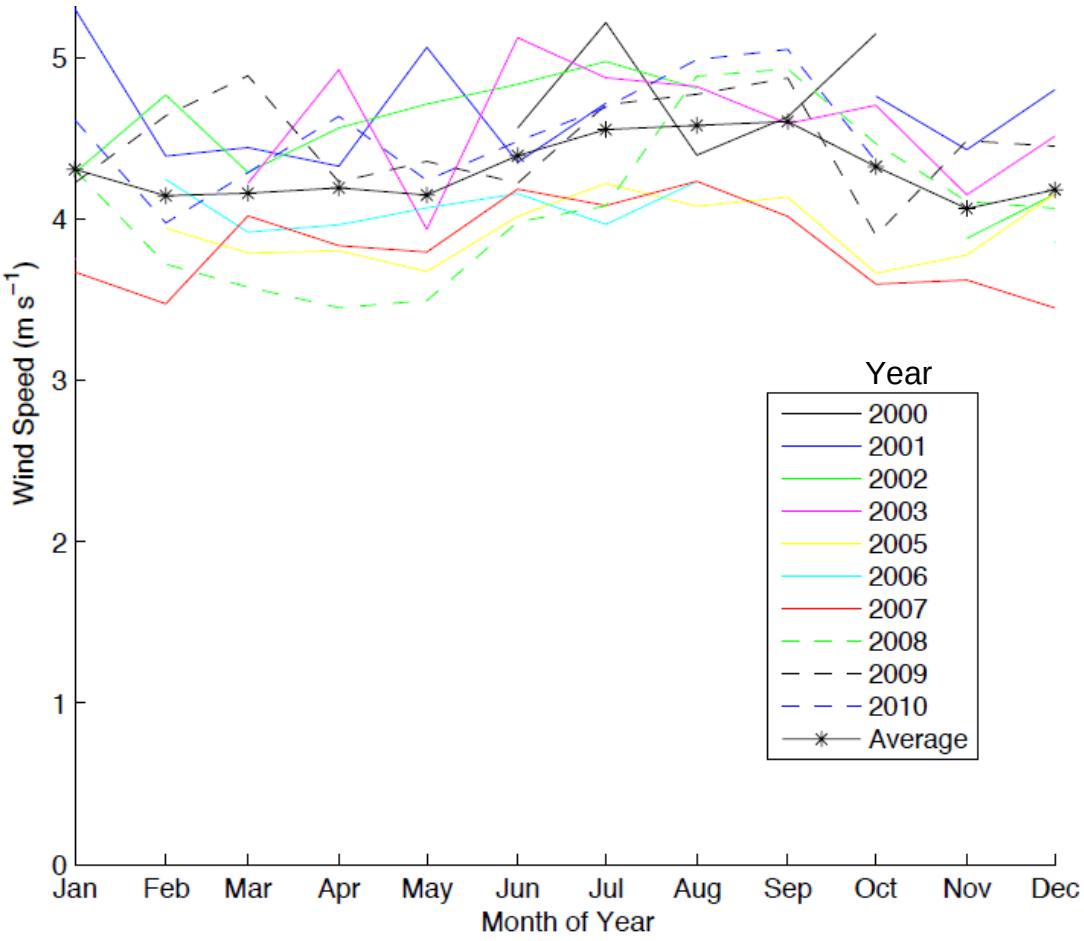

Fig. 23. Wind speeds at PWR reference station from 2000-2010. The anemometer height is around 10 m.

Overall structure

Average diurnal wind speed profiles measured at the canyon exit over the entire GOP are displayed in Fig. 24. On average, profiles during the night displayed jet characteristics with a continuous strengthening during the night (Fig. 24, 2100-0900 MST). During the day, mean wind speed profiles tended to increase monotonically with height (Fig. 24, 1200-1800 MST).

Wind profiles during IOP4 from the ValidWind^{TM} system within the canyon and from the rawinsonde balloon launches at the exit are shown in Fig. 25. IOP 4 was chosen

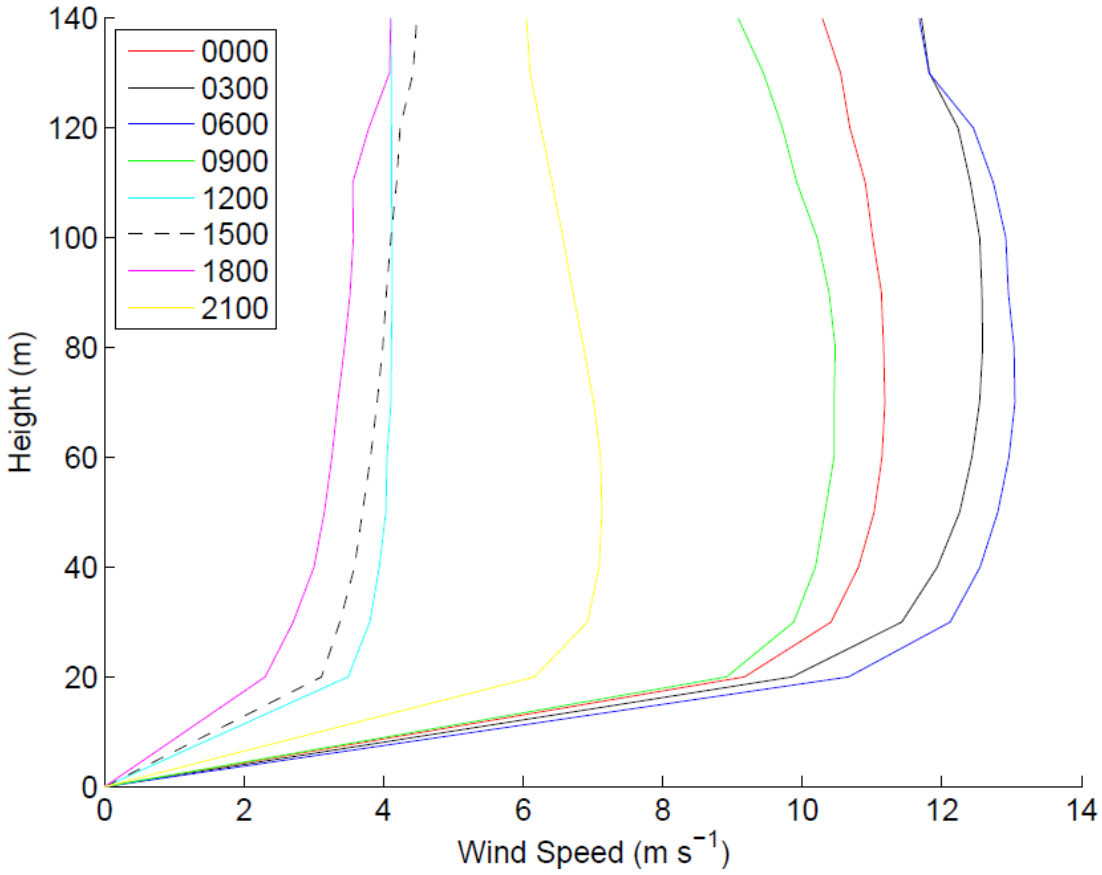

Fig. 24. SoDAR wind speed profiles at the Weber Canyon exit as averaged by hour of day (MST) over the entire GOP. Profiles display averages at each SoDAR measurement height.

as this was the IOP with the most ValidWind^{TM} data. Within the canyon there was a deep more uniform flow layer that occupied the depth of the canyon. The depth of Weber Canyon is on the order of 1000 m and decreases to around 400 m near the exit region. At the exit region the flow was much shallower with a pronounced low-level jet wind maximum. Profiles derived from the rawinsondes are uncharacteristically triangular due to linear interpolation by the sounding processing software.

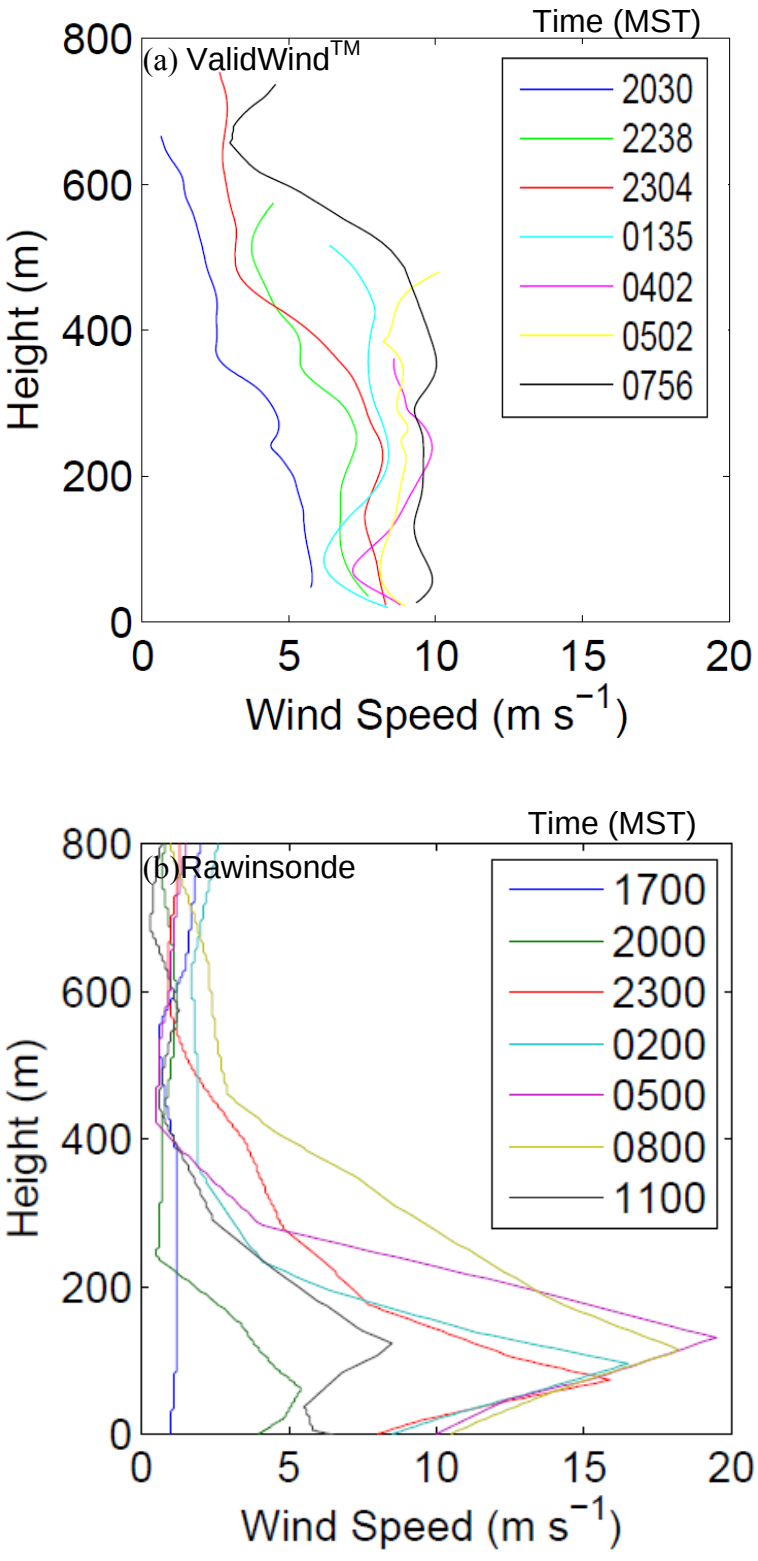

Fig. 25. Wind speed profiles during IOP4 (a) in-canyon measured with ValidWind™ and (b) at the exit measured using a rawinsonde balloon. Times in the legend are MST.

Potential temperature (θ) profiles measured using tethersonde and rawinsonde balloons at the interior and exit of the canyon during IOP 4 are shown in Fig. 26. Within the canyon at night a strong stable layer extended to heights of ~ 100 m. Above this height the profile maintained weaker stability to around 400 m. Potential temperatures were generally warmer overall at the canyon exit than inside the canyon, with a strong stable layer present to around 200 m with near-neutral conditions above. The atmosphere within the canyon cooled continuously throughout the night as shown in Fig. 26. In contrast, at the exit, cooling was contained within the jet layer with negligible cooling above. Fig. 27 overlays potential temperature profiles from within the canyon with those at the exit. A diagnosis of flow motion can be made by comparing the height at which air parcels having equal potential temperature are located. In the absence of diabatic effects, flow tends to follow along isentropes or contours of potential temperature (Cramer 1972). Under this assumption, Fig.27 implies that air parcels that originate at higher elevations within the canyon are brought down closer to the surface at the exit. Continuous cooling aloft within the canyon results in an increasing temperature difference above 200 m. This would imply that the driving mechanism due to the temperature contrast increases with time. Strong nighttime cooling also results in a shallow potential temperature deficit near the surface within the canyon. Turbulence at the exit region is believed to be responsible for the mixing of warmer air from aloft, creating warmer conditions near the surface at the exit.

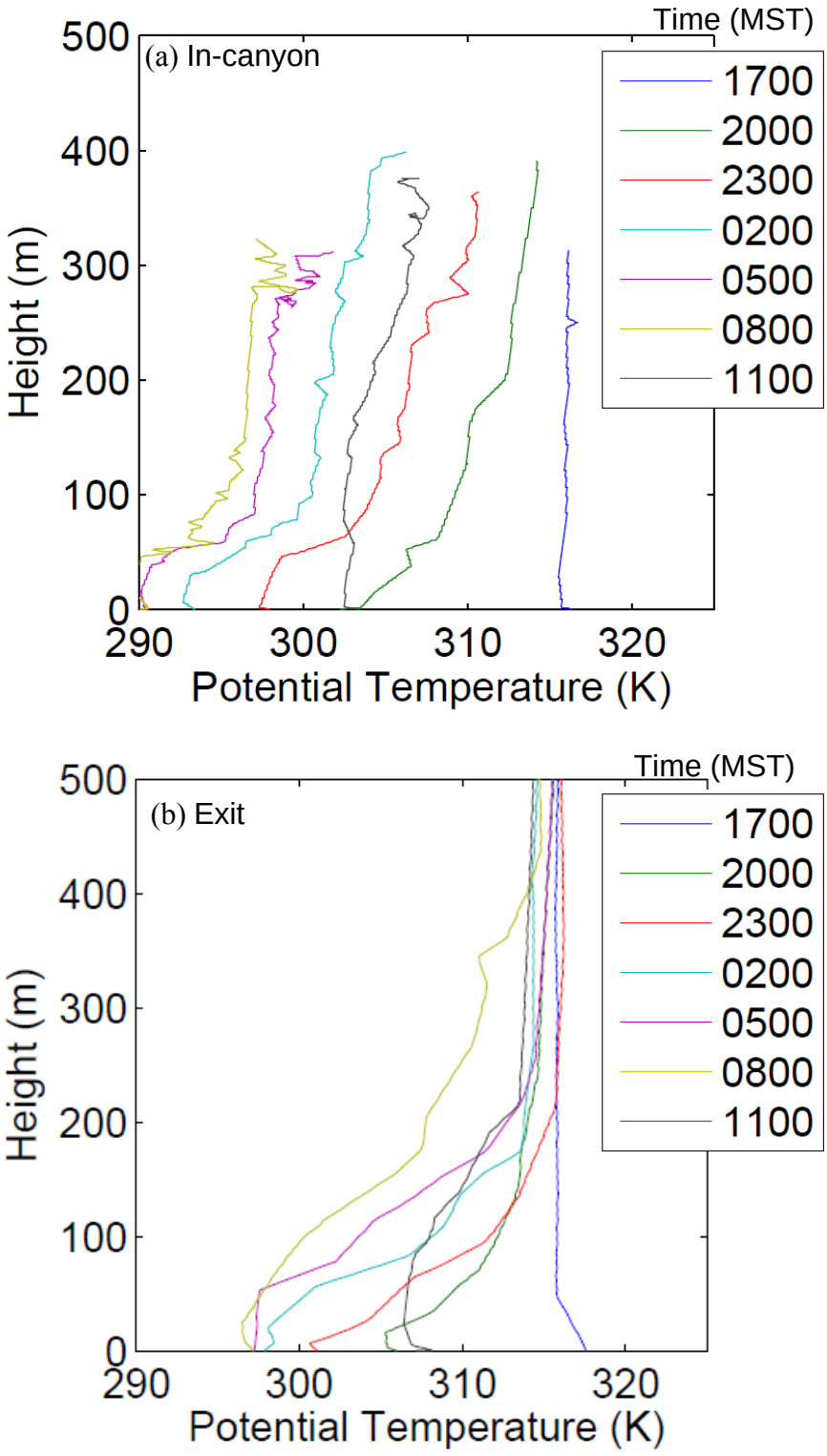

Fig. 26. Potential temperature profiles (a) in the canyon and (b) at the canyon exit, during IOP4. Times are given in the legend in MST.

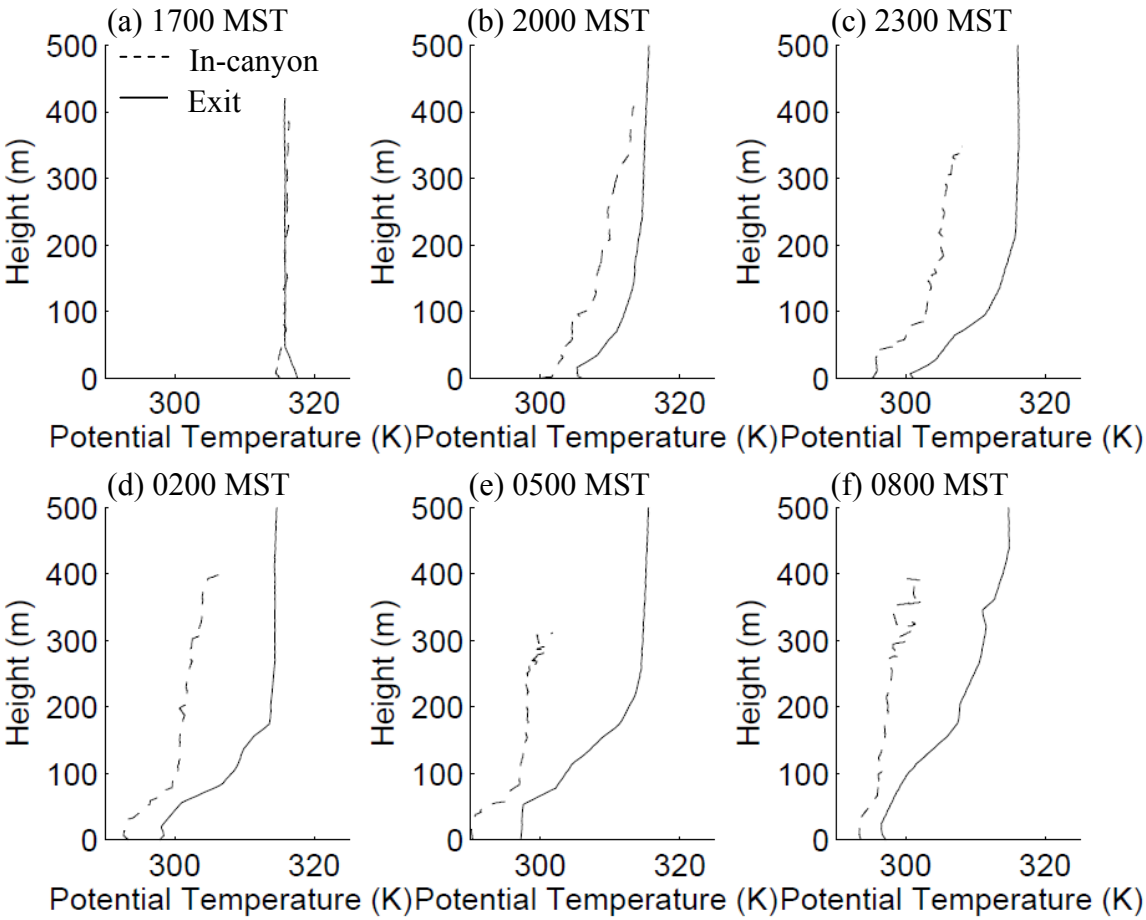

Fig. 27. Potential temperature profiles in the canyon (dashed line) and at the exit (solid line) during IOP4 at (a) 1700, (b) 2000, (c) 2300, (d) 0200, (e) 0500, and (f) 0800 MST.

Flow evolution

Fig. 28 shows time series of wind speed and direction from the LiDAR and SoDAR at three heights within and at the exit of the canyon during IOPs 1 and 4. IOP1 was selected because the flow exhibited subtle differences from the other IOPs. Winds peak before sunrise at both locations. Following sunrise, the winds are eroded by surface heating. At both locations, the transition to down-canyon flow occurs shortly after sunset. The transition to up-canyon flow following sunrise, on the other hand, occurs much more gradually. During the day, anabatic winds are about twice as strong inside the canyon as

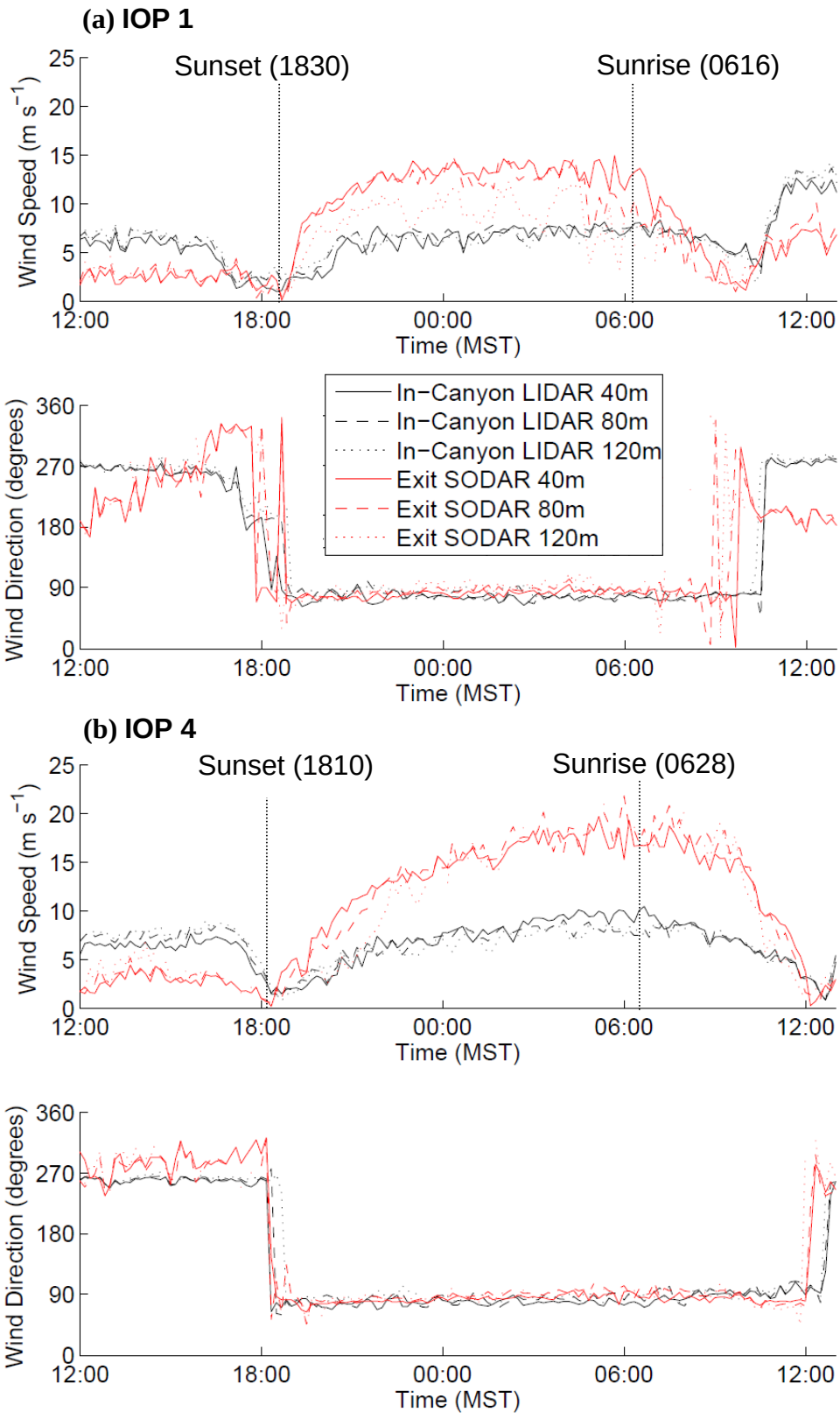

Fig. 28. Time series of wind speed (top) and direction (bottom) in Weber Canyon (black) and at the exit (blue) during (a) IOP1 and (b) IOP4. Sunset and sunrise times in MST are noted in the figure.

at the canyon exit. At night, wind speeds at the exit are about twice as strong as winds within the canyon. During IOP1, the morning transition to up-canyon flow at the exit occurred sooner, possibly as a result of a strong aiding westerly wind component in the GSLB, while down-canyon winds remained quite strong within the canyon for another 1-2 hr. In contrast, during IOP4 winds became calm at both locations prior to the flow reversal and the timing of the transition was delayed until around 1200 MST. During the evening transition, wind direction reversal to down-canyon occurred almost simultaneously at the canyon exit and in the canyon. During both IOPs, winds at the exit of the canyon were the first to undergo a morning wind direction reversal while winds within the canyon followed shortly thereafter.

Time-height cross sections of wind speed and temperature are used to understand how the vertical structure of the atmosphere evolved during IOPs. Figs. 29 and 30 display time-height cross sections of wind and potential temperature at the exit and within the canyon using data from the SoDAR and LiDAR, respectively, during IOPs 1 and 4. In accordance with ValidWind^{TM} profiles during IOP4, there was a deep uniform flow within the canyon (Figs. 29b and 30b). At the exit the flow was forced to compress downwards leading to strong vertical and horizontal accelerations (Figs. 29a and 30a). This compression brought potentially warmer air at the upper levels of the canyon down near the surface at the canyon exit. A very strong stable layer was present across the core of the jet as seen in Fig. 30a, possibly as a result of the flow compression that had the effect of packing the isotherms more closely.

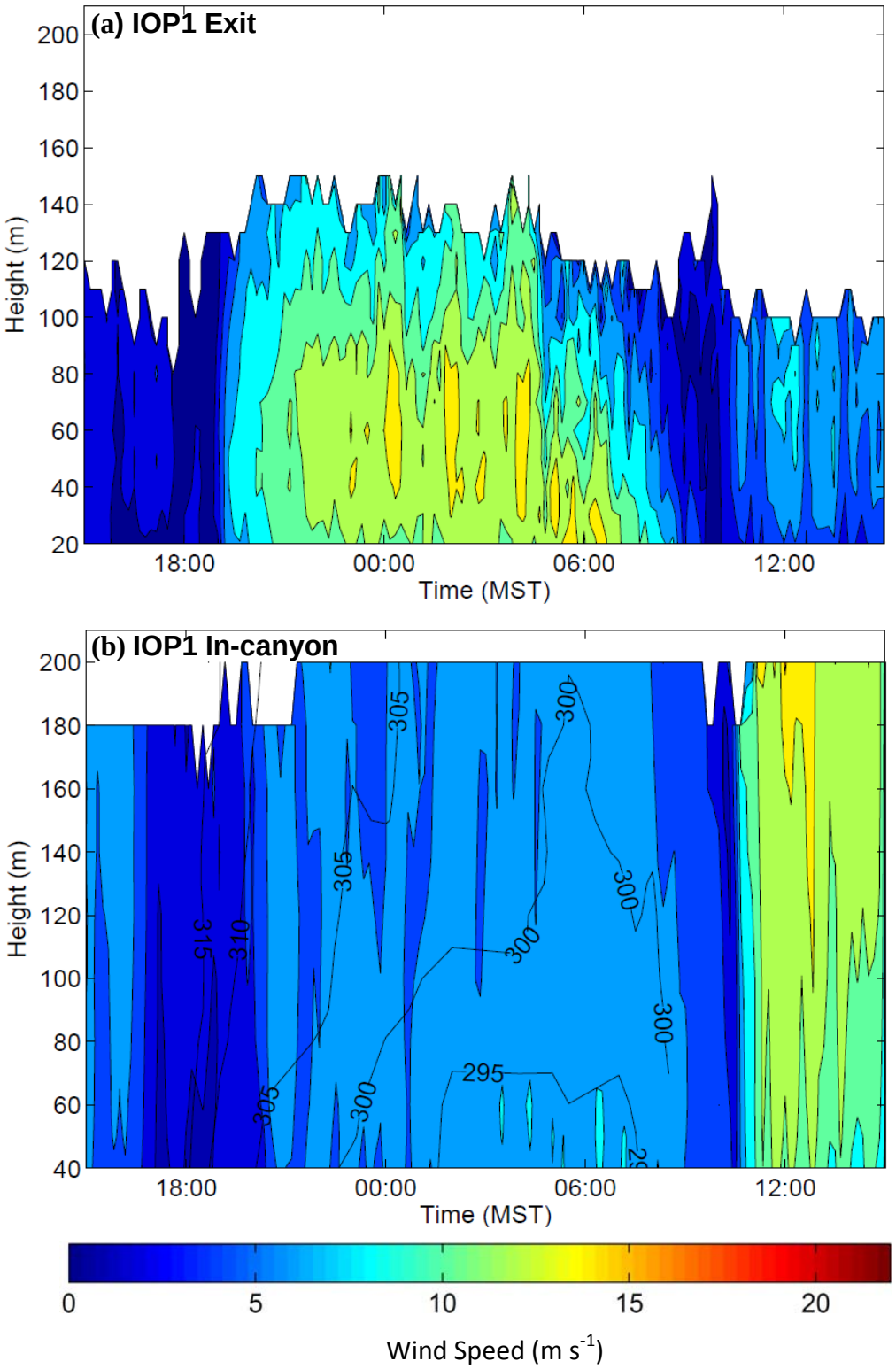

Fig. 29. Wind structure at the (a) exit and (b) in-canyon along with potential temperature (b) in-canyon during IOP4. Contour lines of potential temperature are shown in black. Colors indicate wind speeds (m s^{-1}), as shown in the legend.

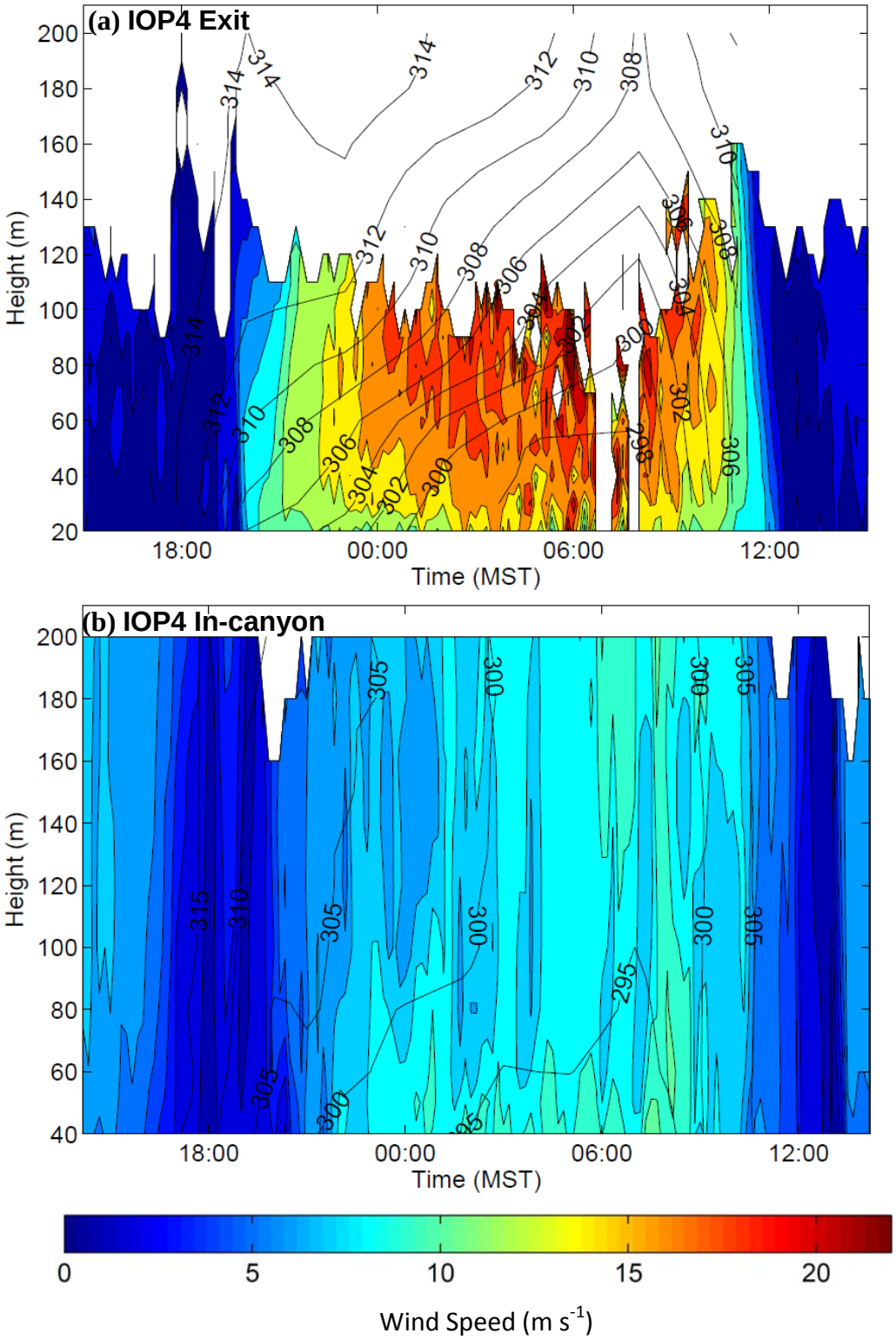

Fig. 30. Wind and potential temperature structure at the (a) exit and (b) in-canyon during IOP4. Contour lines of potential temperature are shown in black. Colors indicate wind speeds (m s^{-1}), as shown in the legend.

The flow at the canyon exit during IOP1 was confined to a shallower layer (Fig. 29a) that is believed to be a result of strong ridge top winds that eroded the canyon flow through detrainment and turbulence at the top of the flow layer. This may have also caused the jet to rapidly decay following sunrise. During subsequent IOPs the SoDAR was unable to resolve winds up to 200 m and therefore some of the structure of the flow is not resolved. During IOP4 winds at the exit were about 5 m s^{-1} stronger and much deeper than during IOP1.

Along-canyon flow evolution

Despite being separated by only a few kilometers, katabatic winds at the exit of the canyon were observed to be about twice as strong as those within the canyon. Concurrent measurements of wind speed within the canyon and at the canyon exit are plotted in the scatter diagram of Fig. 31 for the 3-week period that the LiDAR was used. Anabatic winds are weak at the valley exit while they take on a broader range of speeds within the canyon. Katabatic winds are about twice as strong at the exit region compared to inside the canyon. This agrees well with wind conditions observed during IOPs.

In-canyon flow characteristics

During installation the LiDAR was aligned to geographic north and due to the east-west orientation of Weber Canyon, the u component of the wind speed was directed down the canyon, the v component was directed northward across the canyon and the w component was directed vertically. Time-height cross sections of the three wind speed

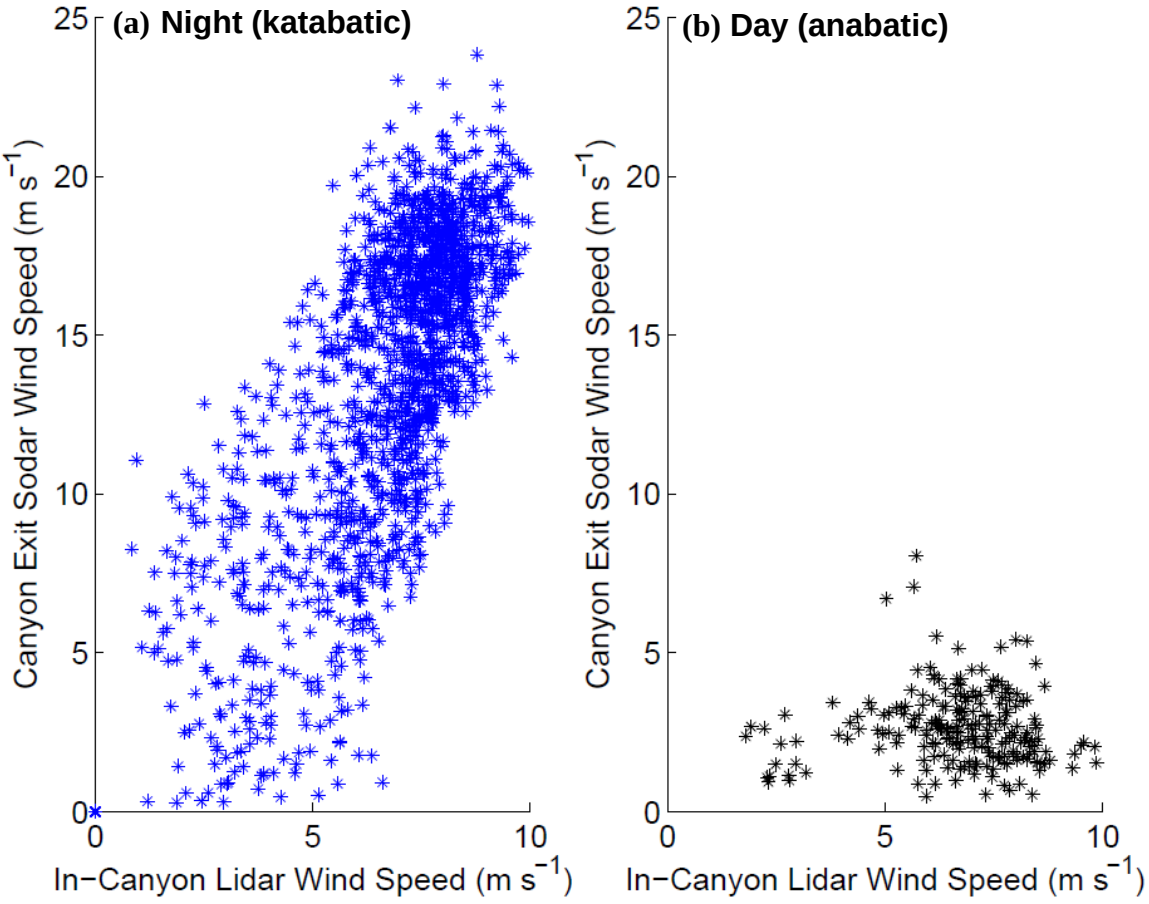

Fig. 31. Concurrent measurements of wind speed at 80 m AGL in the canyon and at the canyon exit during (a) nighttime katabatic flow and (b) daytime anabatic flow. Data points are 10-min averages over a three week period for which there are concurrent measurements from the SoDAR and LiDAR.

components, the average horizontal wind speed and the turbulence intensity (TI) during IOP3 are shown in Fig. 32. Turbulence intensity is defined as the ratio of the standard deviation of wind speed over the average wind speed over a measurement period. In this case 10-min averages are used. IOP3 was chosen because distinct cross-canyon circulations were observed. Flow along-canyon (Fig. 32a) was strongest near the surface and then deepened around 0600 MST where along-canyon winds became uniform up to at least 200m. Distinct periodic cross-canyon pulsations are observed

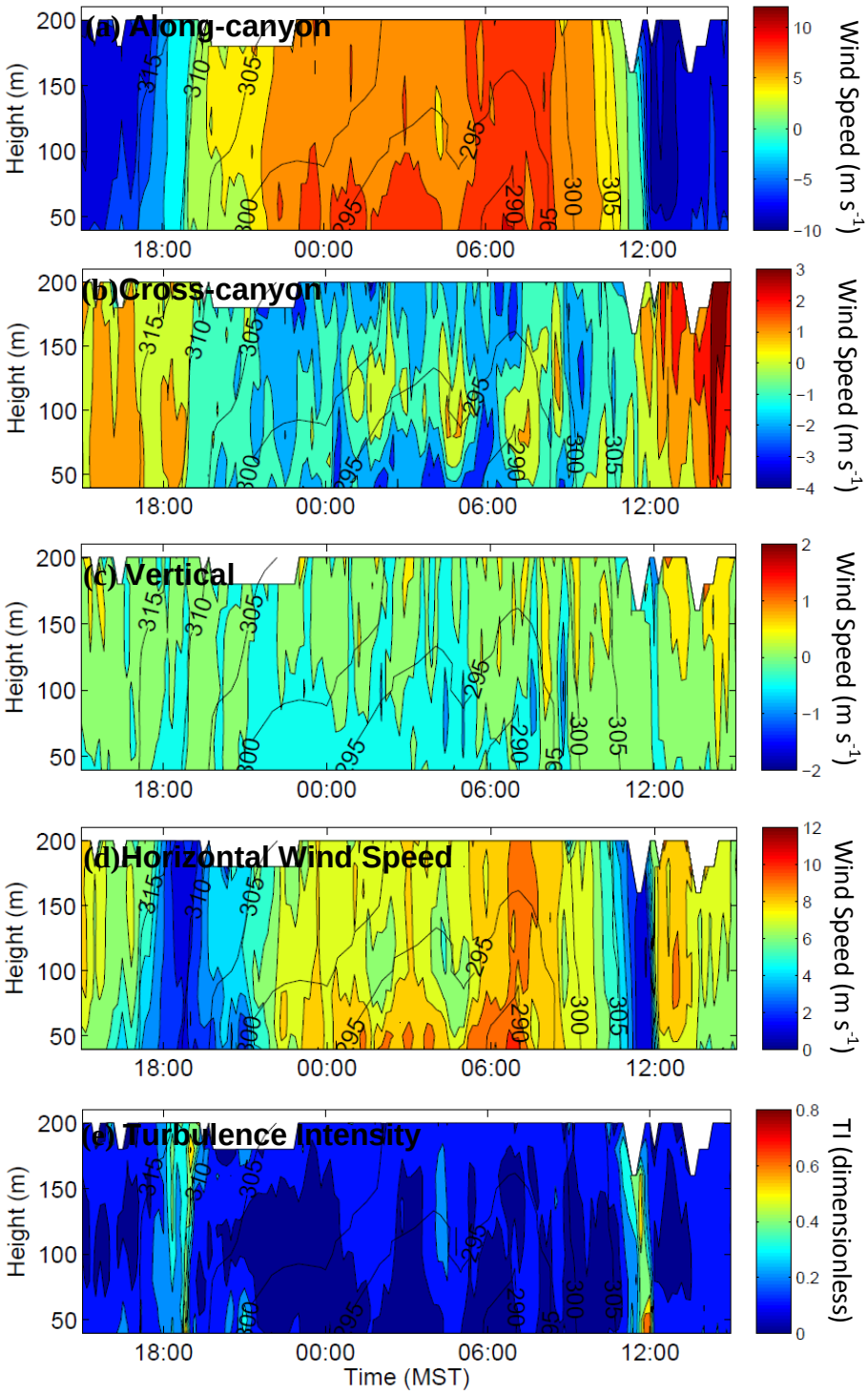

Fig. 32. Along-canyon (a), cross-canyon (b), and vertical wind speed components (c), average horizontal wind speed (d) and turbulence intensities (TI) (e) as measured by the LiDAR during IOP3 in Weber Canyon. In (a)-(d) legend colors indicate wind speeds (m s^{-1}), and in (e) legend colors indicate turbulence intensity. Times are in MST.

(Fig. 32b, 0000-0900 MST) during the night. Corresponding weak downward vertical motion is observed to occur concurrently (Fig. 32c), possibly representing the convergence of slope flows in the valley center. The cross canyon circulations also correspond to brief periods of increased turbulence intensity as shown in Fig. 32e. Variability is observed in the horizontal wind profile (Fig. 32d) over time and this variation appears to be related to the juxtaposition of the along and cross canyon wind circulations.

Discussion of the exit jet formation

As described previously, potential temperature data support the conclusion that slower moving air from aloft within the canyon descends along constant potential temperature surfaces and accelerates into a jet at the exit region of Weber Canyon. Vertical winds observed at the SoDAR location support the conclusion of strong downward motion at the exit. Fig. 33 displays vertical wind speeds measured at the canyon exit during IOPs 1 and 4. Vertical wind speeds during IOPs 1 and 4 are -1.5 and -2.5 m s^{-1}, respectively. The strong vertical winds form as a deep layer of air drains out of the canyon, thins and compresses downward into a shallower layer forming the jet. There is a conversion of potential energy from the deep in-canyon flow layer to kinetic energy at the exit as the flow speed increases. The jet-like shape of the wind speed profile is a result of the flow compression and friction that forces the wind speed to vanish at the surface.

The net vertical motion is due to the flow compression and the downward slope of the canyon floor. At the exit region of Weber Canyon the average slope of the terrain in the down-canyon direction is approximately 1.5%. Considering wind speeds on the order

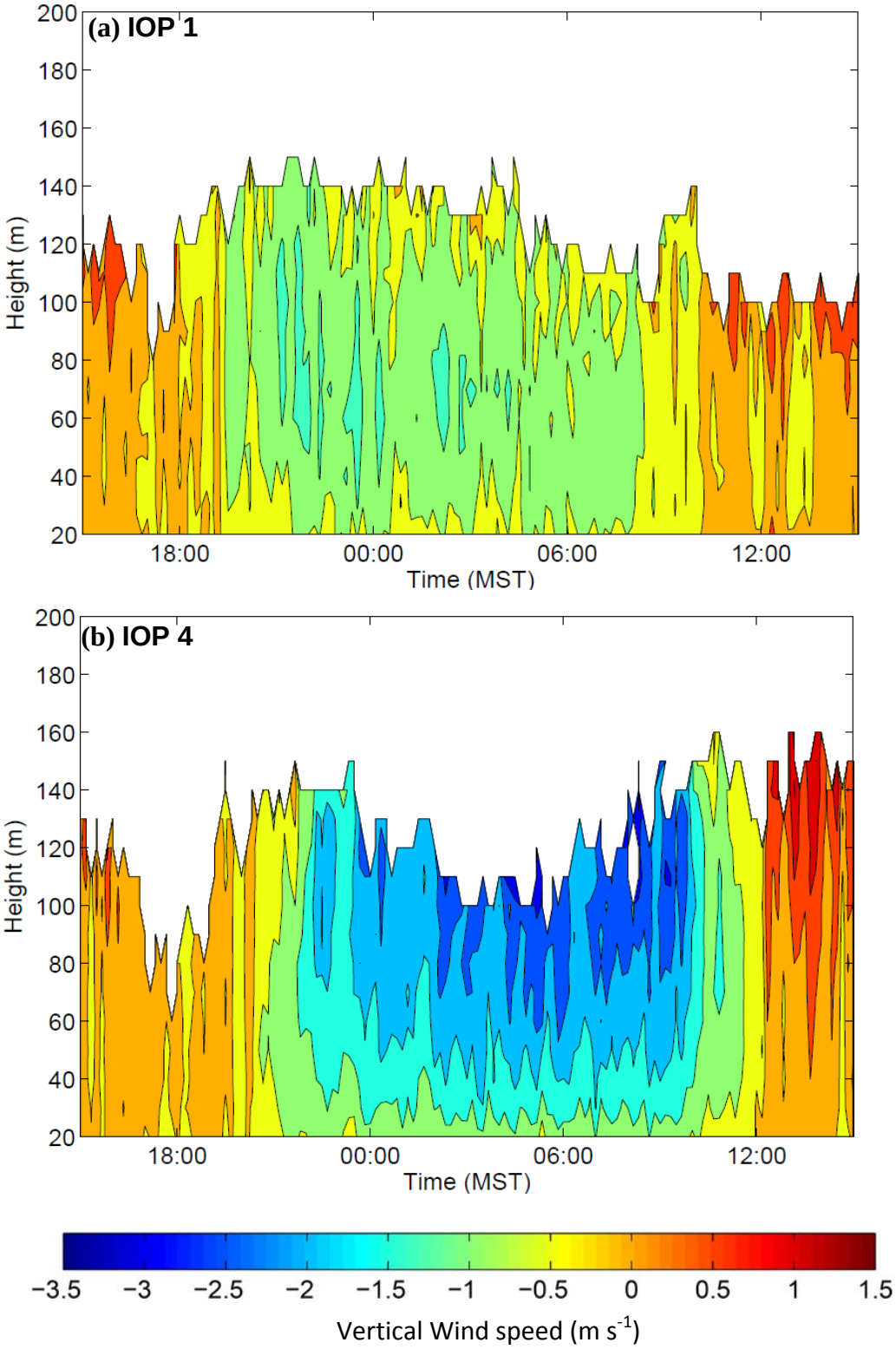

Fig. 33. Vertical wind speed measured by the SoDAR at the exit of Weber Canyon during (a) IOP1 and (b) IOP4. Colors indicate wind speeds (m s^{-1}), as shown in the legend.

of 20 m s^{-1}, this would produce a vertical wind component on the order of 0.3 m s^{-1}. Estimates can be made about the strength of the vertical wind speeds produced by adiabatic descent of air from within the canyon to the exit region. As shown in Fig. 27 at 2000 MST, air from a level of ~ 400 m within the canyon is brought down to a level of ~ 100 m at the exit. Considering that the two locations are separated by a distance of ~ 5 km and that the mean flow motion is on the order of 15 m s^{-1}, this would produce average vertical winds on the order of 1 m s^{-1}. Overall, the net effect of the terrain slope and flow compression can partially help explain the magnitude of the vertical winds measured at the exit region.

It has been suggested that hydraulic effects can help explain the accelerations at the exits of valleys and gaps. Zängl (2004) computed the reduced gravity Froude number (*Fr*) to quantify whether there was a transition from subcritical to supercritical flow at the exit of the Inn Valley in Austria. *Fr* is shown in Eqs. (4) and (5) below and can be interpreted as the ratio of inertial to gravitational effects or similarly as the ratio of kinetic to potential energy of a flow layer. Model results from Zängl (2004) suggest that the flow became supercritical in the exit region and formed a low-level jet.

$$Fr = \frac{U}{\sqrt{g' H}} \tag{4}$$

$$g' = g\frac{\Delta\theta}{\theta} \tag{5}$$

Eqs. (4) and (5) along with data from IOP 4 (Figs. 25 and 26) were used to compute the reduced gravity Froude number inside and at the exit of Weber Canyon. Our results indicate that the $Fr < 1$ inside the canyon and that at the exit region $Fr \sim 0.5$-1,

indicating that the flow can be interpreted as subcritical within the canyon and that it can possibly approach a critical state at the exit.

As previously discussed, Mayr et al. (2007) found that hydraulic theory can be used to describe gap flow conditions in the Brenner Pass within the Wipp Valley of Austria. The exit of the gap was found to be the point at which the flow transitioned from subcritical to supercritical. Further downstream a hydraulic jump was found that returned the flow back to a subcritical state. Because of a lack of observations, it is unclear at this time whether or not a hydraulic jump, which would occur if there was a return from supercritical to subcritical flow, is present beyond the exit of Weber Canyon.

Role of synoptic conditions in producing variability in the jet

The jets at the exit of Weber Canyon exhibited subtle differences from day to day over the course of the GOP. Several data sources were used to investigate whether differences in canyon flow characteristics could be linked to the synoptic conditions. Synoptic charts, SoDAR, and surface weather data were compared to find interelationships. The two nearby surface weather stations that proved useful were the Ogden Peak (OGP) and Hill Air Force base (HIF) stations. OGP, located on Ogden peak at an elevation of 2900 m, provided a source of data for ridgetop conditions. By applying a spectral decomposition to surface timeseries data, Rife et al. (2004) found that about 67% of the power at the OGP station is within the super diurnal band and that only ~2% is in the diurnal band, justifying its use as an indicator of synoptic conditions. HIF is located on a mesa top 7 km southeast of the Weber Canyon exit. A separate analysis has shown that during typical nightime outflow conditions from Weber Canyon, the flow routinely extends to Hill AFB so that this station provided an indication of flow

penetration into the GSLB. Results from the data intercomparison indicate that synoptic conditions appear to produce changes in the structure of the jet at the exit of the canyon. For example, the jet was weaker and shallower at the exit (Fig. 29a) during IOP1 when ridgetop winds were strong (Fig. 34a) and was deeper and stronger at the exit (Fig. 40a) during IOP2 when ridgetop winds were lighter (Fig. 34b).

Because the exit jet structure appeared to be influenced by synoptic conditions during the IOPs, we extended our analysis to the entire GOP to relate SoDAR-determined exit jet structure to synoptic conditions. A subjective analysis of the data led to an identification of four flow regimes based on ridgetop and exit region winds during the GOP. Results were as follows: (1) shallow jets were observed when ridgetop winds were strong (> 5 m s^{-1}) and in direct opposition to the downcanyon flow; (2) shallow jets were also seen when very strong ridgetop winds (> 10 m s^{-1}) blow at an acute angle to the canyon flow (e.g. during IOP 1 when ridgetop winds were from the southwest); (3) a much stronger outflow was observed at the canyon exit with the flow no longer contained within a shallower layer when ridgetop winds were at an acute angle to the canyon outflow but less than 10 m s^{-1}; and (4) strong outflow was observed during times of weak ridgetop winds (IOP2) and when easterly wind directions aided the downcanyon flow from the east.

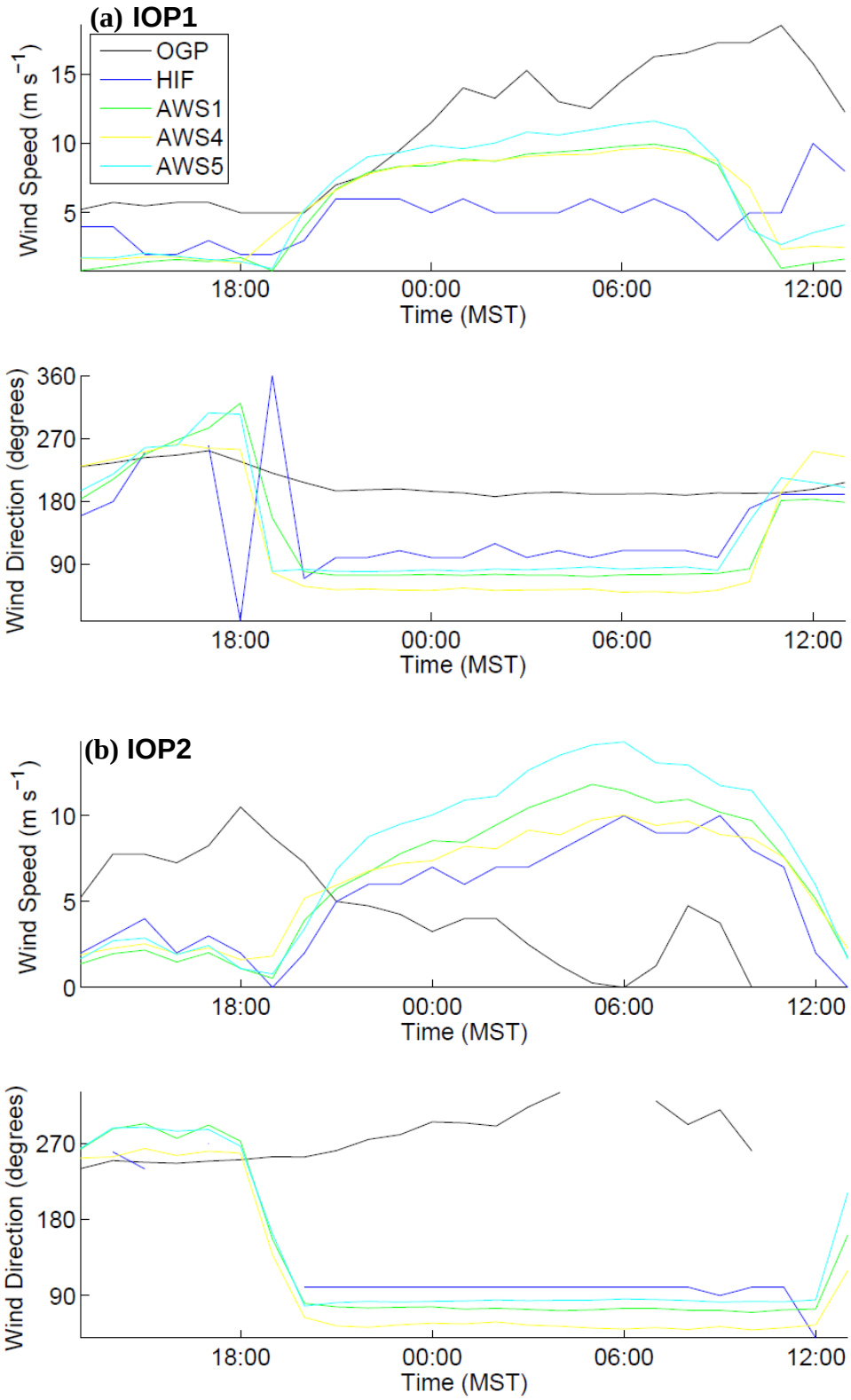

Fig. 34. Wind speed (top) and wind direction (bottom) at selected surface stations (see legend) during (a) IOP1 and (b) IOP2.

CHAPTER 5

WIND ENERGY POTENTIAL AT EXIT REGION

The power contained in the wind is proportional to the cube of the wind speed (Manwell et al. 2002). Using a binning method, average power and wind energy density at the Weber Canyon exit are calculated using Eqs. (6) and (7), respectively. Wind speed measurements for a full year are binned by month to produce mean monthly wind speed frequency distributions.

$$\frac{\overline{P}}{A} = \frac{1}{2}\rho \sum_{j=1}^{N_B} V_j^3 f_j \tag{6}$$

$$\frac{\overline{E}}{A} = \frac{\overline{P}}{A}\Delta t \tag{7}$$

In Eq. (6), ρ is the monthly air density, V^3_j is the cube of the wind speed value of each bin, N_B is the number of bins and f_j is the frequency associated with each bin by month. The result is a measure of average power $\overline{P}$ per unit area A at the measurement height. The average monthly energy density $\overline{E}$ can be calculated as the time integral of the power density using Eq. (7). For our case the time period is one month since monthly values are desired.

The resulting wind power and energy densities by month are shown in Fig 35. Manwell et al. (2002) suggest that wind power density $\geq$ 400 W m^{-2} is considered good

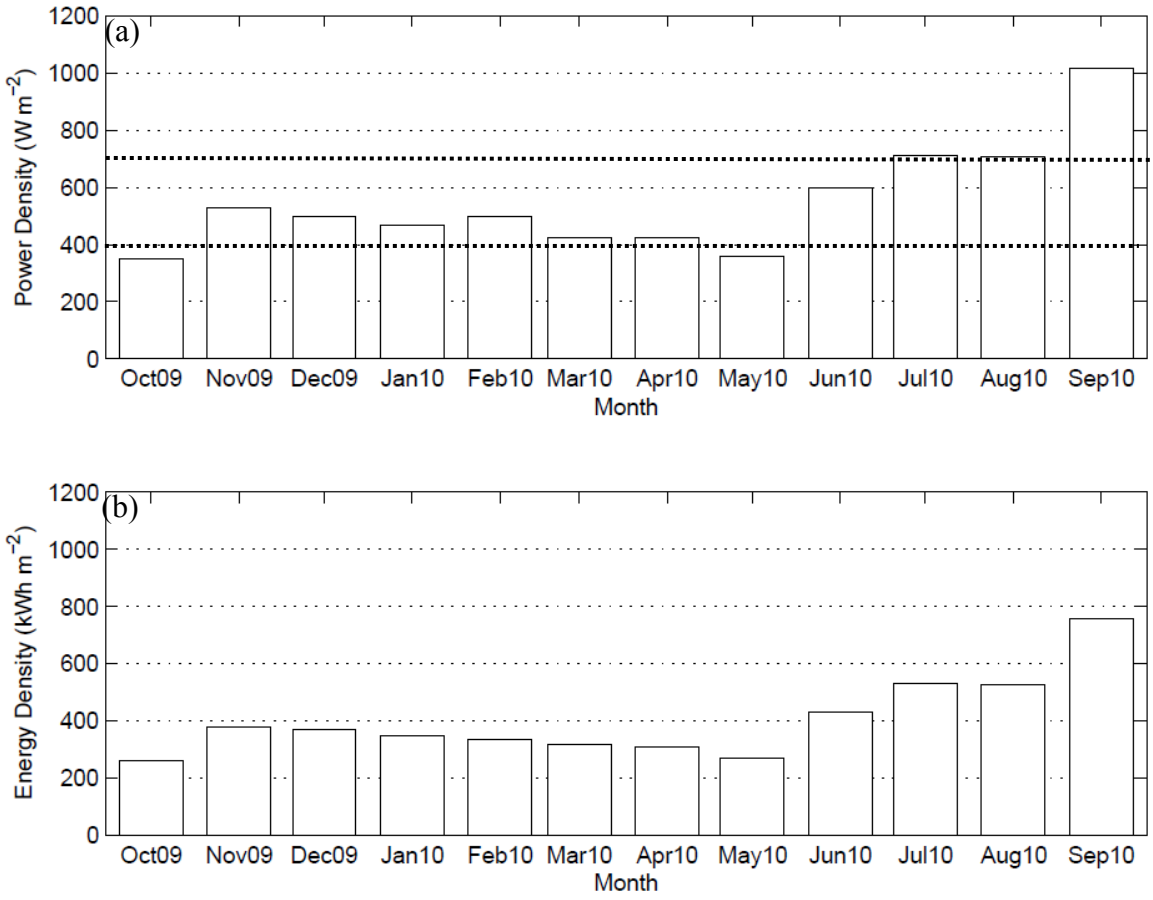

Fig. 35. Monthly wind (a) power density and (b) energy density at 50 m based on one year of tower data from October 2009-September 2010. Threshold wind power density levels defined by Manwell et al. (2002) are shown in the top panel as bold dashed lines.

and wind power density ≥ 700 W m^{-2} is considered great for wind power potential. In this context the wind power density potential at the exit of Weber Canyon is good in most months and great in the summer and early fall months.

With respect to wind energy estimation, wind data from a lower height is usually extrapolated to the expected hub height of future wind turbines using shear values calculated between the lower heights. This practice has been a major source of error and contention within the wind energy meteorology community. Two common models to extrapolate wind data are the power law and log law shear models (Manwell et al. 2002).

The power law model is shown in Eq. (8) and the log law model in Eqs. (9) and (10). In these equations z is the height of interest in meters, U is the wind speed (m s^{-1}) at the height of interest and z_r is the reference height in meters, U^* is the friction velocity in m s^{-1}, z_o is the roughness length in meters, $k = 0.4$ is the Von Karman constant and α is the power law shear exponent.

$$\frac{U(z)}{U(z_r)} = \left(\frac{z}{z_r}\right)^{\alpha} \tag{8}$$

$$U(z) = \frac{U^*}{k}\ln\left(\frac{z}{z_o}\right) \tag{9}$$

The log law Eq. (9) can be rewritten as,

$$U(z) = \underbrace{\frac{U^*}{k}}_{m}\ln(z) - \underbrace{\frac{U^*}{k}\ln(z_o)}_{b} \tag{10}$$

For a neutral atmosphere, if average wind speed is plotted against the logarithm of height, the resulting profile is linear and a best fit line through the points allows one to determine the friction velocity U^* and the roughness length z_o from the slope m and offset b as shown in Eq. (10). Many empirical studies have determined that wind profiles in the lowest part of the atmospheric boundary layer can be described using these models. However, for complex terrain situations in which jet wind speed profiles are typical, an alternative method is needed as is demonstrated by our exit jet data.

To illustrate the problems in using the standard extrapolation methods, these methods have been applied using three months of tower data during the GOP. The

extrapolations to hub height are then compared to SoDAR data, which extend through and above the jet maximum, during the same period to diagnose how well the standard methods work for wind data extrapolation. The overall average SoDAR profile (day and night) is plotted in Fig. 36 along with percentages of data recovered at the individual range gates (i.e. heights). A wind speed maximum is seen at 70-80 m, with winds decreasing slowly above this height. 140 meters was chosen as the height below which data recovery rates were acceptable from the SoDAR. Overall, recovery rates of the SoDAR data slowly decreased with increasing height. Because the SoDAR tended to not adequately capture high wind speed events it is possible that some of the decrease in winds with height as seen in the SoDAR wind profile could be due to this loss of data. Average tower measurements at heights of 10, 30 and 50 m are plotted next to the SoDAR profile. A bias is observed in the average wind speed profiles between the SoDAR and tower, with the SoDAR reporting wind speed ~ 0.5 m s^{-1} lower than those measured on the tower. The three methods of wind extrapolation using the wind shear models previously described are joined with the measured tower profile to illustrate how well each extrapolation method performs. The log law method (Eq. 10) produces the extrapolated wind speed profile that is plotted in red. This method produces over-predictions of wind speeds at hub height. It should be noted again that the above equations are valid only for a near-neutral atmosphere. In cases where the stability differs substantially these equations can produce additional errors. The power law extrapolation method, using shear exponents derived from tower measurements between 30 and 50 m and from SoDAR measurements between 50 and 80 m is shown in Fig. 36 as pink and green lines. Predictions of the 80 m average wind speed are over-predicted using shear

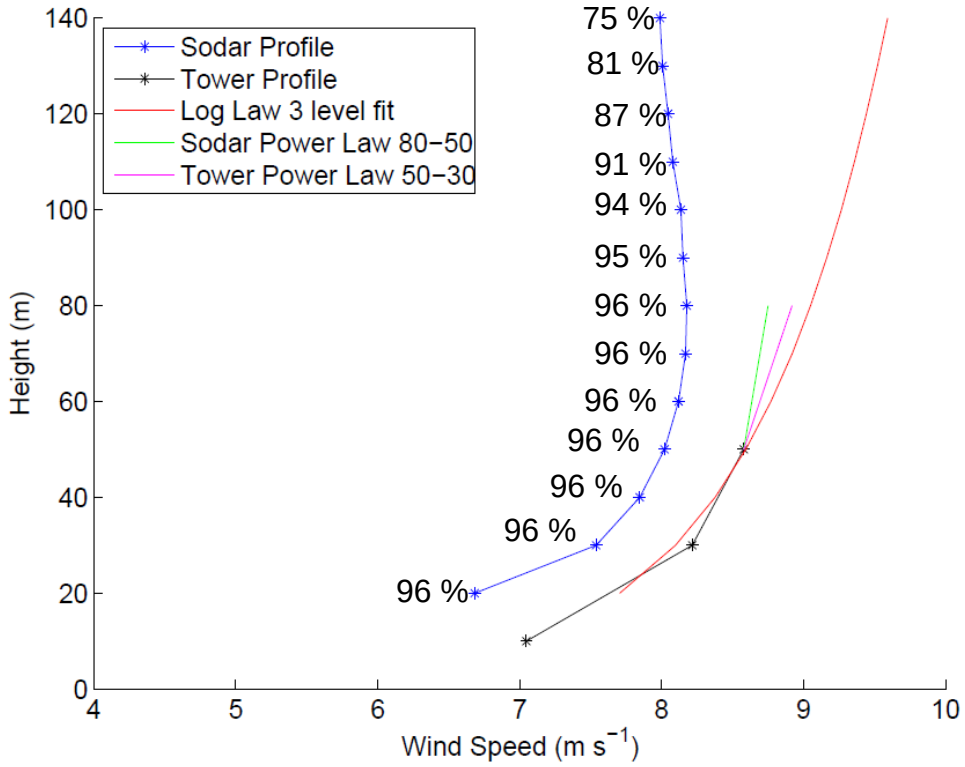

Fig. 36. Average wind speed profile from the SoDAR and tower over the GOP. Three methods of wind shear extrapolation are shown with respect to the tower profile. The red curve displays a 3 level fit using the log law (Eq. 10), and the green and pink lines illustrate extrapolated hub height wind speeds using power law (Eq. 8) shear parameters from the SoDAR between 80 and 50 m and from the tower between 50 and 30 m, respectively. Data recovery rates (in percentage) at each height are shown.

parameters derived from the tower data. Only when the measured shear value between 80 and 50 m from the SoDAR is used does the prediction (green line in Fig. 36) of the 80 m tower wind speeds match the trend observed in the SoDAR wind profile although wind speeds continue to exceed those measured by the SoDAR due to the bias previously mentioned. This is where the value of remote sensing is realized. For a fraction of the cost of installing taller towers, a remote sensing device could be used to measure wind profiles at higher heights. Unfortunately in some cases of wind energy estimation, remote sensing data is not acceptable solely on its own because of reliability and measurement technique issues.

CHAPTER 6

MODEL SIMULATIONS

The Advanced Research WRF (ARW) model developed at the National Center for Atmospheric Research (NCAR) was used to perform numerical simulations of katabatic and anabatic flows within Weber canyon. The WRF is a numerical weather prediction (NWP) model that has been developed to simulate atmospheric flows that encompass a variety of length and time scales ranging from slowly varying global climate down to rapidly varying planetary boundary layer (PBL) turbulence. The model has been developed so that nested simulations consisting of smaller domains with finer grid spacing may be carried out within larger simulation domains resulting in the ability to model a range of atmospheric motions.

WRF model description

The WRF model has been designed as an open source community model and therefore is very flexible in how it is set up and run. The main components are the WRF pre-processing system and the ARW model. The WRF pre-processing system is responsible for ingesting various types of input data such as meteorological observations, topography and land surface parameters as well as defining the simulation domains, grid array and interpolating model input data onto this grid. The ARW is one dynamical core within the WRF model, the other is the Non hydrostatic Mesoscale Model (NMM). The

ARW dynamical core is based on the fully compressible nonhydrostatic form of the Euler equations. See Skamarock et al. (2008) for a complete technical description of the WRF ARW model.

Initial and boundary conditions

The WRF model uses a terrain-following sigma coordinate system with the top model level representing a constant pressure surface at the top of the atmosphere. The equations are prognostic, meaning that the evolution of variables at each grid point is solved sequentially in time. Boundary and initial conditions are supplied through the input of meteorological data. In this case, meteorological data from the National Center for Environmental Prediction (NCEP)/NCAR North American Regional Reanalysis (NARR) model was used to supply boundary and initial conditions. Mesinger et al. (2006) describe the methodology used to produce the NARR. They describe the NARR as being a long-term, dynamically consistent, high resolution, atmospheric and land surface hydrology data set for North America. Essential components of the system used to generate the NARR are the lateral boundaries from and the data used for the NCEP-DOE Global Reanalysis, the NCEP Eta model and its data assimilation system, and a recent version of the Noah land surface model (Mesinger et al. 2006). The NARR has a horizontal resolution of 32 km with 45 vertical layers. The NARR combines several data sources including rawinsonde and dropsonde soundings, pilot balloons, aircraft soundings, satellite, and other surface and upper air networks. The data is assimilated and interpolated onto a rectangular grid for each domain in WRF every three hours.

Flow in Weber Canyon is a result of atmospheric forcing that acts over a range of length scales, from synoptic forcing to micro scale forcing due to topography and surface

roughness. For this reason the model was set up to run multiple nested domains sequentially in order to capture the dynamics down to the micro scale. The outermost domain covers the entire western half of the U.S and the inner domain is centered over the lower section of Weber Canyon as shown in Fig. 37. The horizontal grid resolutions of the four domains shown in Fig. 37 are 33.25 km, 6.25 km, 1.25 km, and 250 m, respectively. The first model vertical level was located at 34 m above ground level (agl), followed by 100 m agl and then approximately every 100 m above 100 m agl. Topographic data was input into the WRF model and interpolated onto each domain grid during the pre-processing stage. The WRF model itself includes 30 arc second (~1 km) coarse resolution topography data used for the outermost domains. For the two innermost domains, high resolution topographical data from the United States Geological Survey (USGS), at a spacing of 1 arc second (~30 m), was used after a slight smoothing to reduce numerical noise and instabilities. The topography of the two inner grid domains is shown in Fig. 38.

Model parameterizations

Atmospheric motions are a result of the interaction of complex physical processes that act over a range of time and length scales. Due to limitations in current computational resources it is impossible to explicitly resolve all of the processes that contribute to atmospheric motions even though the governing equations describe them well. These processes include turbulence and mixing, radiation, surface physics, cloud formation and other microphysical processes such as evapotranspiration. Depending upon the grid resolution of a particular simulation and the characteristic length and time scales of the dominant physical processes, some sub-gridscale (SGS) processes must be

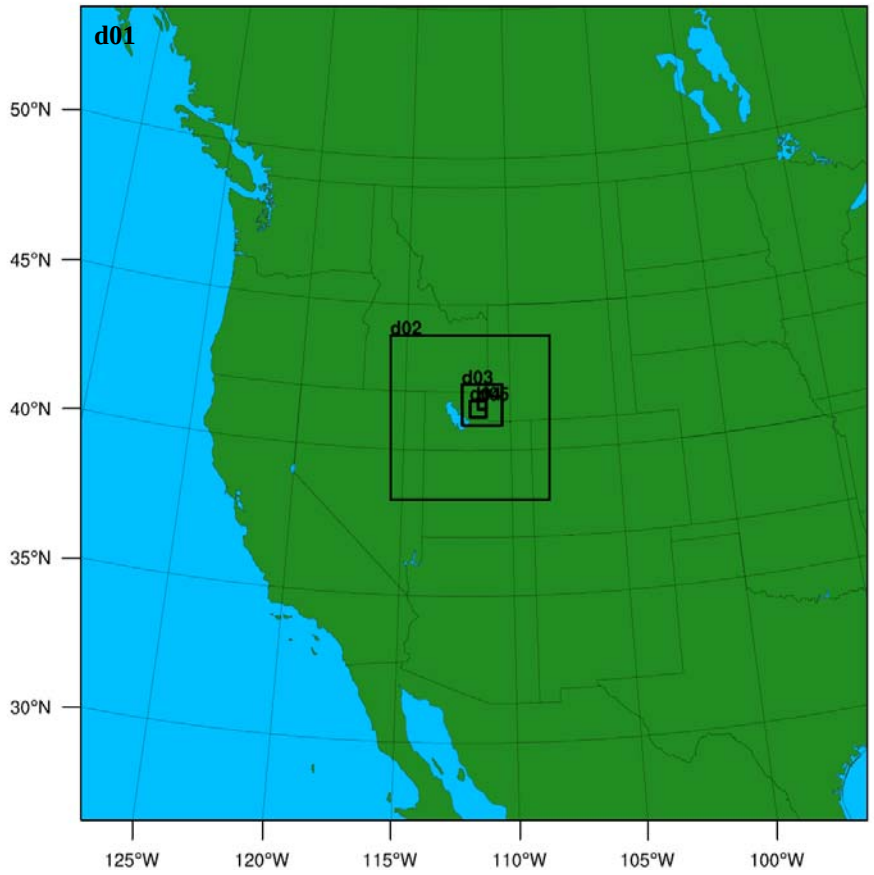

Fig. 37. Boundaries of the four WRF simulation domains. The horizontal grid resolution of the four domains is 33.25 km, 6.25 km, 1.25 km, and 250 m, respectively.

parameterized. Modeling of SGS processes is necessary to incorporate their effects into the resolved mean flow evolution.

The simulations discussed in this chapter utilize large eddy simulation (LES) techniques. In LES, PBL turbulence parameterization is turned off allowing the model to explicitly resolve most of the turbulent PBL circulations. SGS turbulence parameterization is still necessary to resolve small turbulent eddies that are responsible mostly for dissipation of energy but also for the small scale transport of heat and momentum. The LES technique was used only for the innermost high resolution grid domain. Standard parameterization methods were used in the outer domains.WRF offers

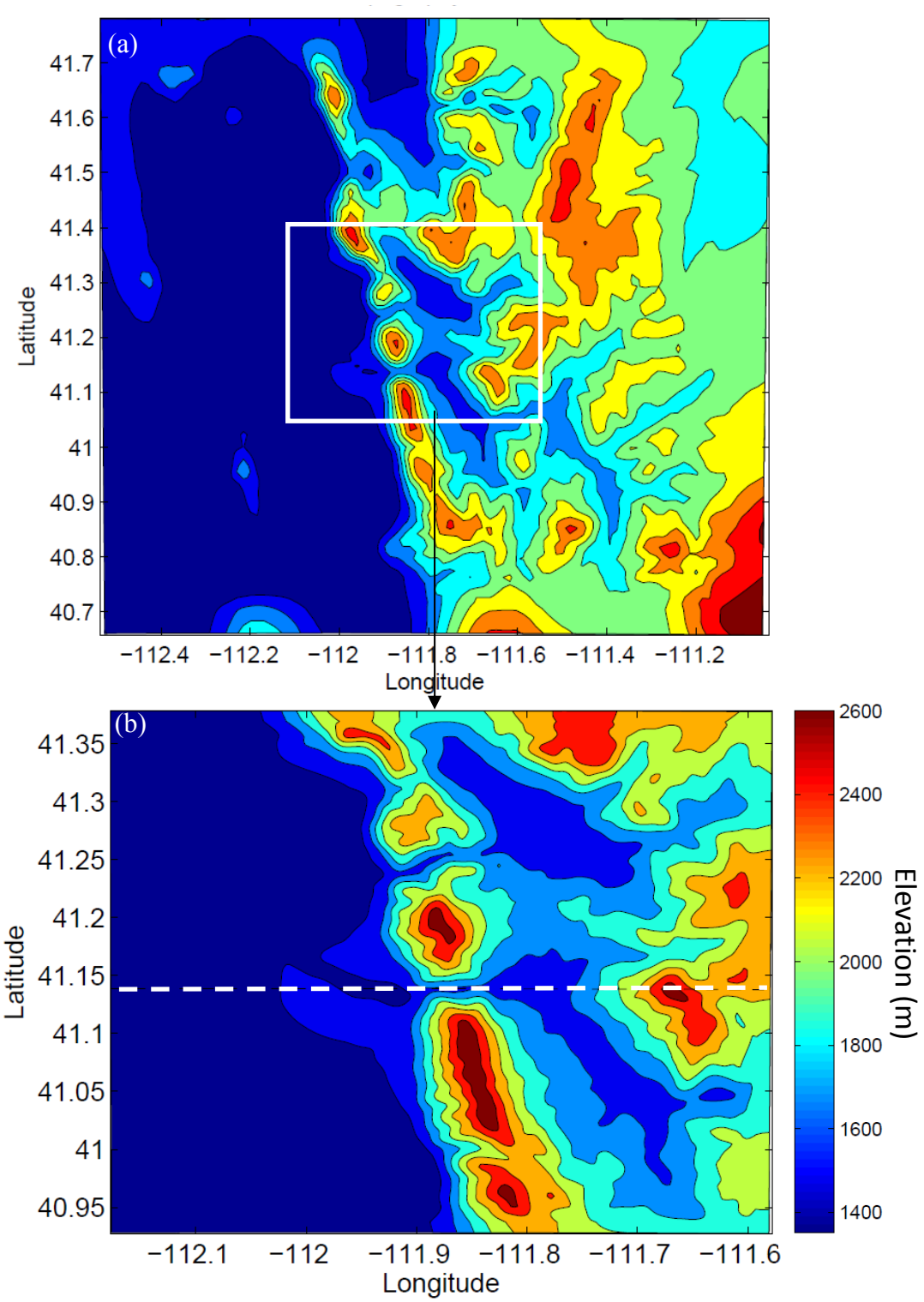

Fig. 38. Smoothed grid topography of the two inner WRF simulation domains. The color scale shows the contour heights in meters. The corresponding horizontal grid resolutions are (a) 1250 m and (b) 250 m, respectively. The location of the east-west cross section shown in Fig. 43 is plotted as a dashed black line in (b).

many parameterization options and some of the key ones used are described here in more depth.

Turbulence and mixing in the planetary boundary layer (PBL)

PBL parameterizations are used to model fluxes of heat, moisture and momentum in the boundary layer for which vertical mixing and diffusion play large roles. A 1.5 order turbulent kinetic energy (TKE) closure scheme (Janic 1990, 1996, 2002; Mellor and Yamada 1982) with second order diffusion was employed for turbulence parameterization. This closure method was used for full turbulence parameterization in the larger domains and for SGS parameterization in the highest resolution domain, where LES techniques were used.

Recently there has been controversy regarding whether typical PBL parameterization models are appropriate for use in modeling SGS turbulence in LES models. Mirocha et al. (2010) propose an alternative closure model for the treatment of SGS stresses and discuss deficiencies in the typical PBL parameterizations. Their closure model, termed the nonlinear backscatter and anisotropy (NBA) model, accounts for second-order nonlinear turbulence stress terms. The authors note that the NBA model has shown considerable improvement over linear eddy-viscosity models in convective, neutral and stable stratified LES PBL simulations. The NBA closure technique has been now implemented into WRF as a standard option for LES. The NBA option was tried for simulations at Weber Canyon, but after several hours the simulations became unstable, so that the final simulations had to use TKE closure. Further implementation of the NBA closure model is proposed as future work.

Radiation

Radiation parameterization in WRF is related to shortwave and longwave surface radiative fluxes as well as atmospheric temperature evolution. The simulations described here used a rapid radiative transfer model (RRTM) scheme (Mlawer et al. 1997) for long wave radiation and the Dudhia scheme (Dudhia 1989) for shortwave radiation. Both longwave and shortwave radiation schemes are capable of interacting with clouds, trace gases and aerosols in the atmosphere. The shortwave scheme accounted for the effects of sloping terrain and topographic shading in the Weber Canyon simulations.

Surface physics

The surface physics parameterization, which interacts with other parameterization schemes as shown in Fig. 39, determines the exchange coefficients of heat, moisture and momentum between the surface and the atmosphere based on Monin-Obukhov similarity theory (Monin and Obukhov 1954). The unified Noah land surface model was employed to define surface properties such as surface roughness.

Microphysical processes

Microphysics parameterizations are responsible for modelling the effects of evaporation and condensation, as well as water and ice nucleation leading to rain and snowfall. These are related to the overall tendencies of heat and moisture in the atmosphere. The WRF single moment 3-class scheme as described in Hong et al. (2004) was employed in these simulations, allowing for mixed-phase processes and super-cooled water. However, because the simulation was dry the microphysics scheme was unimportant.

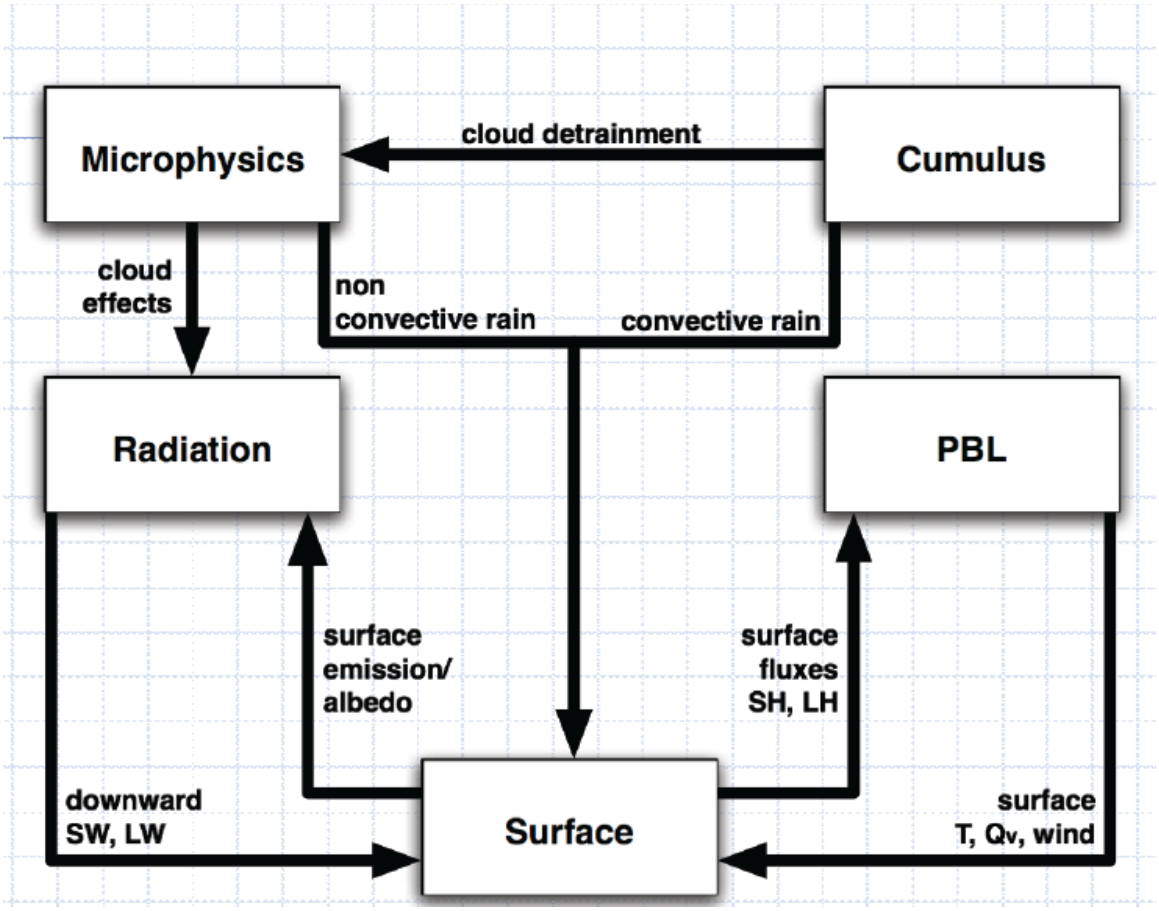

Fig. 39. Interaction of parameterizations in the WRF model.

Cumulus

The cumulus parameterization deals with updrafts, downdrafts and rainfall development within the model. Cumulus schemes are most often applied in models that have large grid spacing. For our simulations, the Kain-Fritsch scheme (Kain 2004) was used. However, because clear skies dominated the simulation period the cumulus scheme was unimportant.

Results

The WRF model was run for the four domains shown in Fig. 36. The innermost 250 m grid spacing domain was run using LES techniques. Results are shown for the 250 m resolution domain.

IOP comparison

Figs. 40 and 41 compare time-height observations of wind and temperature with model simulated results at the SoDAR and LiDAR locations during IOP2. Model results were bilinearly interpolated from the model grid to the two locations. The results show that the model does a fair job of simulating the timing and vertical structure of the observed flow and temperature fields. Weak uniform flow in the canyon and strong jet-like flow at the exit are predicted by the model. The simulated initiation and cessation times of the canyon flow (Fig. 40) match the observations. However, the simulated wind speeds inside the canyon and at the canyon exit are too low by several m s^{-1}. The simulations also produce potential temperatures that are generally too cold and potential temperature gradients that are too small and shallow compared to the observations. Some of the differences between the simulations and observations can be attributed to coarse height and time resolution (1-h) of the model output.

Spatial evolution of winds over the simulation domain

Surface wind speeds over the inner simulation domain are shown at different times during a 24 hr simulation period in Fig. 42. At night, weak surface winds are predicted over most of the domain but the model predicts a very strong outflow jet from Weber Canyon and other adjacent canyons. The simulated flow accelerates within the

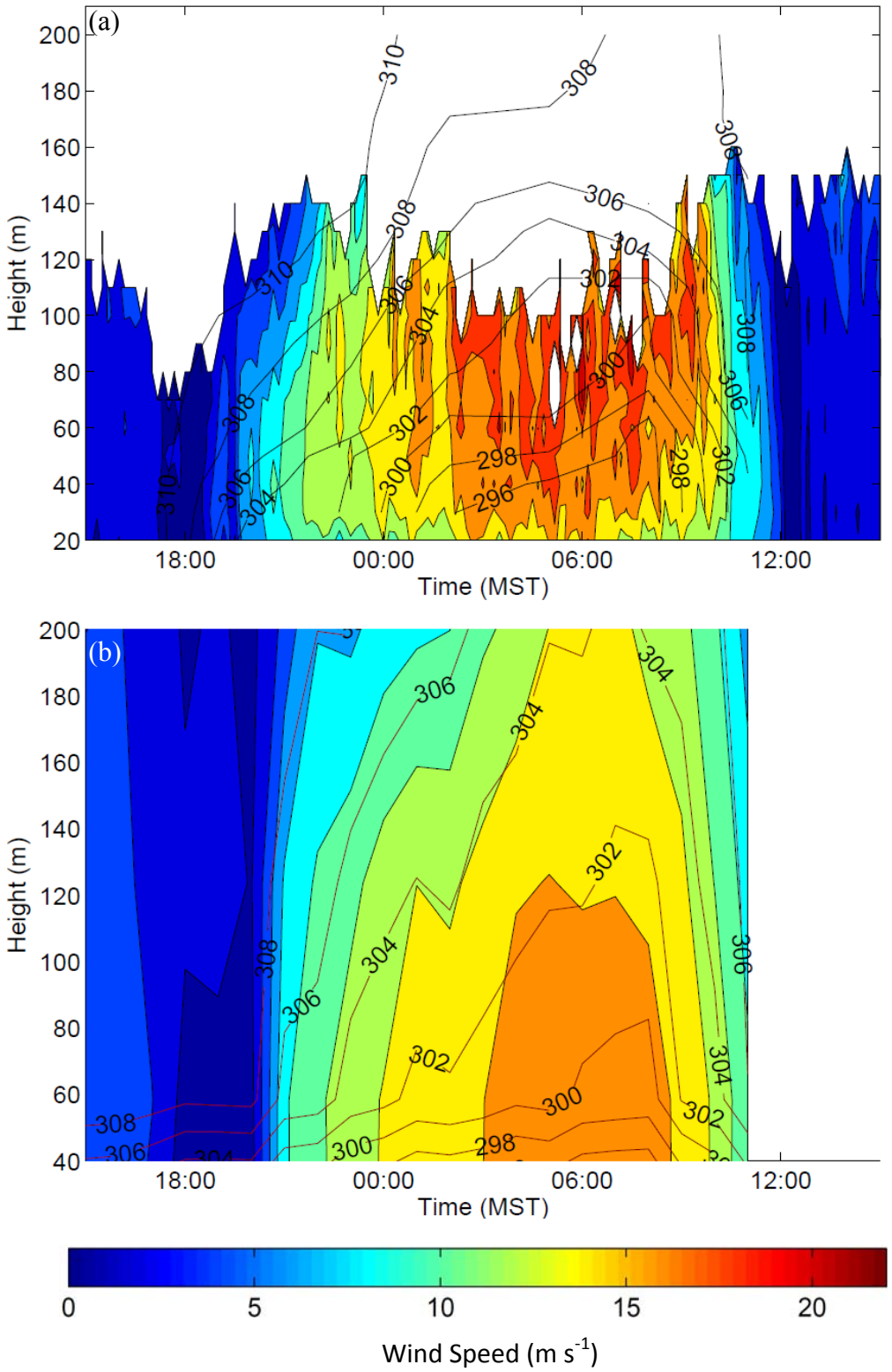

Fig. 40. Time height cross section of potential temperature (K, contours) and wind speed (m s^{-1}, colors) measured (a) at the Weber Canyon exit by the SoDAR and (b) simulated using WRF for the 250 m grid resolution domain during IOP2.

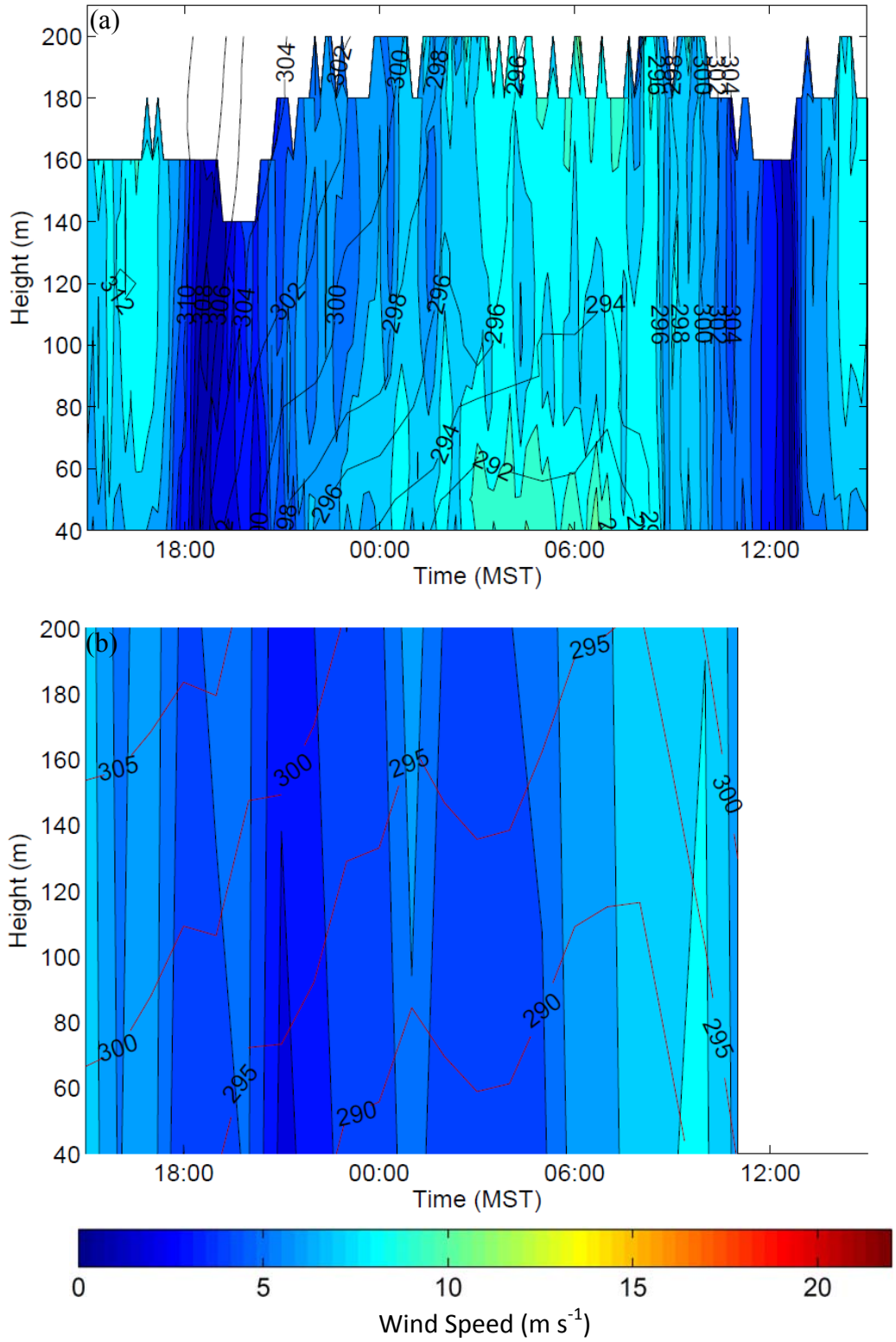

Fig. 41. Time-height cross section of potential temperature (K, contours) and wind speed (m s^{-1}, colors) measured (a) in Weber Canyon at the LiDAR and (b) simulated using WRF for the 250 m grid resolution domain during IOP.

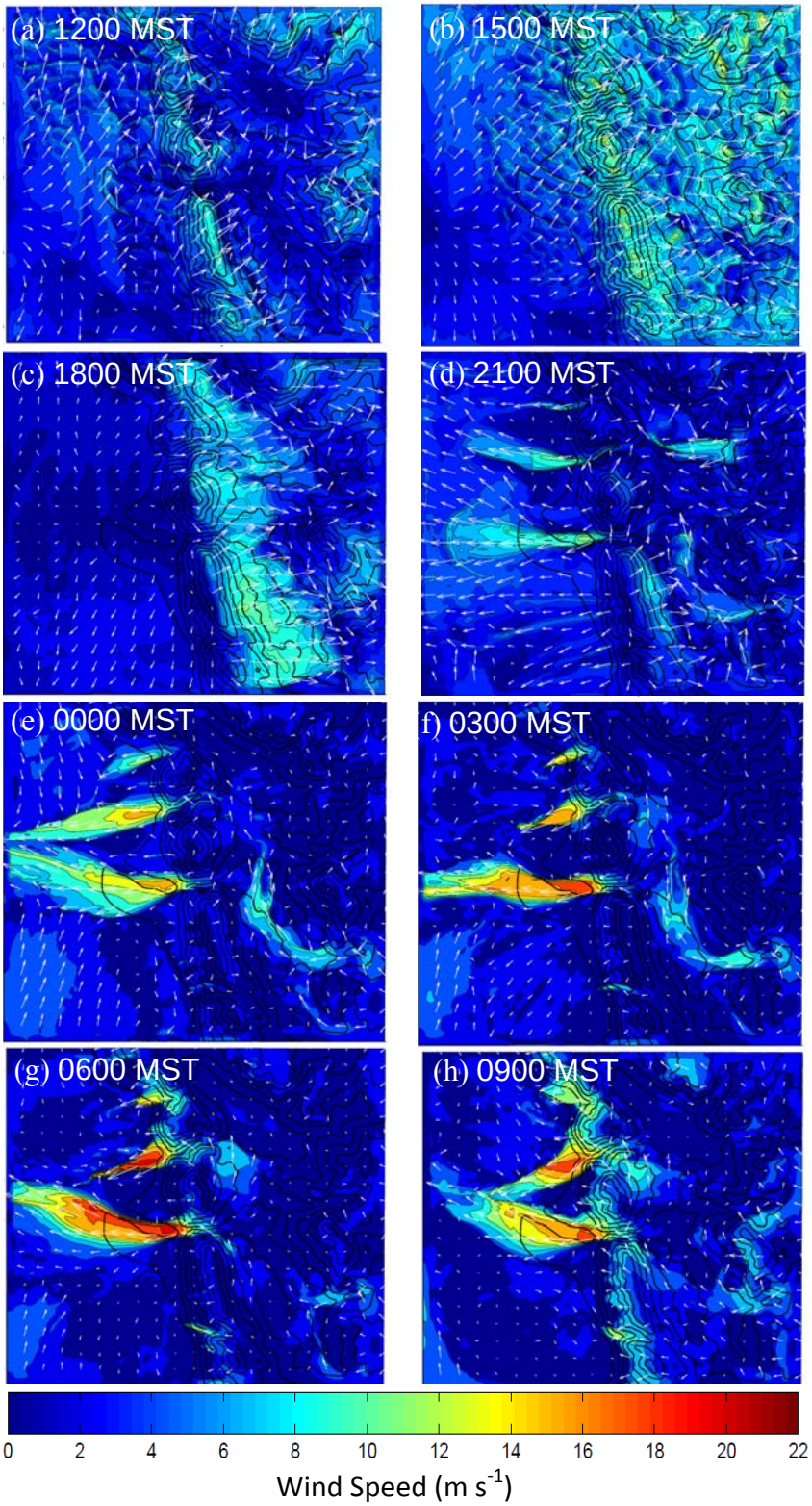

Fig. 42. Birdseye view of WRF-simulated 10 m wind speeds in the 250 m resolution domain over a 24 hr. period of IOP2. Panels (a)-(h) show simulated wind speeds every 3 hours starting at 1200 MST. Wind vectors denote wind direction. Color legend indicates speeds (m s^{-1}). The domain topography and location is the same as shown in Fig. 38b.

lower section of the canyon followed by a rapid acceleration at the canyon exit. Beyond the exit the jet diffuses and widens. On the northern flank, winds tend to follow the topographic gradient that flows slightly northward to the GSLB. Winds in the interior portion of the jet tend to flow straight westward and on the southern flank they diverge slightly southward. The jet extends more than 20 km into the GSLB to the shore of the Great Salt Lake.

Limitations exist in the model for defining land surface properties such as surface roughness and obstacles that often cause significant momentum loss near the surface. Because of this the actual jet may not extend as far as predicted by the model. The flow is observed to routinely extend to the HIF weather station, located 7 km beyond the Weber Canyon exit. An interesting feature in Fig. 42 is that downslope winds develop on the eastern flank of the Wasatch Mountains and flow into the Weber Canyon basin prior to canyon flow initiation. Wind speeds in this flow appear to be quite strong, perhaps unrealistically so. During the day, organized wind circulations are present at the surface representing model generated convection and turbulence. Prevailing winds are from the southwest and stronger wind speeds are predicted at the ridgetops.

Along canyon acceleration

Wind and temperature data along the E-W cross section depicted in Fig 38b is shown in Fig. 43. This particular cross section was chosen because grid points run E-W through the lower section and exit of Weber Canyon, providing a display of the spatial evolution of the wind field as it transitions from within the canyon to the exit region. The approximate longitudinal position of the SoDAR (S) and LiDAR (L) are shown at the bottom of the figure. The elevation profiles of the canyon floor and from the ridgetop on

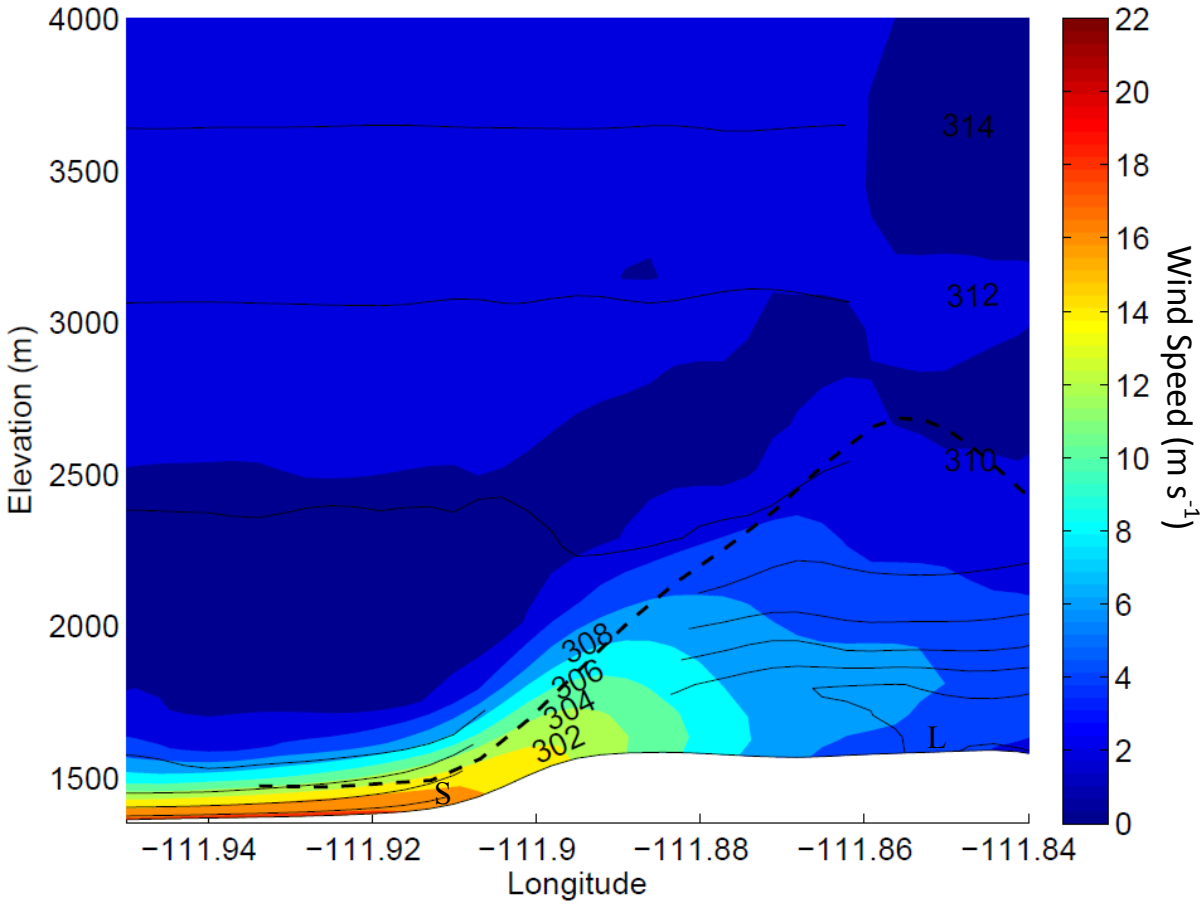

Fig. 43. WRF simulated wind and potential temperature along the east-west cross section through Weber Canyon shown in Fig. 38b. The contours are potential temperatures in Kelvin. The colors represent wind speeds in m s^{-1}. Approximate longitudes of the SoDAR (S) and LiDAR (L) are displayed. The ridge-top elevation profile (in meters) of the lower section of Weber Canyon is shown as a dashed line. The elevation profile is taken from the mountains on the south side of the canyon. The elevation of the lowest model level is shown as a solid black line at the bottom of the figure where the contours terminate.

the south side of the canyon are also displayed. As winds flow from within the canyon to the exit, a uniform flow layer compresses and accelerates as it reaches the exit region. Potentially warmer air from above from within the canyon is brought down closer to the surface resulting in a near isothermal layer of weak winds above the jet and a compressing of isentropic surfaces within the jet resulting in a strong potential temperature gradient at the exit.

CHAPTER 7

CONCLUSIONS AND RECOMMENDATIONS

This thesis research has led to several conclusions regarding the nature of canyon wind flows and valley exit jets that form within the Wasatch Mountains of northern Utah and, specifically at Weber Canyon. A summary of conclusions follows:

- The durations of nocturnal katabatic winds inside and at the exit of canyons along the Wasatch Front are longer for canyons having larger drainage areas.
- Nocturnal winds issuing from each of the canyons provides a source of cold air to the GSLB. During the day anabatic winds advect air from the GSLB into the mountains.
- Katabatic outflows begin ~ 0-3 hours after sunset. In the larger canyons, katabatic outflows continue 5-6 hours after sunrise. In the smaller canyons, the transition from katabatic to anabatic flow occurs much sooner.
- In Weber Canyon, katabatic outflow continues 5-6 hours past sunrise regardless of the season. The evening transition from anabatic to katabatic flow usually occurs 1-3 hours after sunset, with the most rapid transition occurring in summer and early fall months.

- In Weber Canyon, wind flows exhibit a strong seasonal dependence with the strongest, deepest and most consistent down-canyon flows occurring during summer and early fall nights. Highly consistent valley exit jets were observed in Weber Canyon during the summer and early fall of 2010 with ~ 83% of the nights from July through September exhibiting strong exit jets. Up-canyon flow was strongest in Weber Canyon during the springtime.
- The katabatic flow was observed to rapidly accelerate from inside the canyon to the exit region where winds were typically twice as strong as those inside the canyon.
- Strong downward vertical wind speeds were observed at the canyon exit supporting the theory that a deep but weak down valley flow inside the canyon thins, descends and accelerates at the exit of the canyon converting potential energy into kinetic energy. Through this compression mechanism potentially warmer air from aloft within the canyon down closer to the surface at the exit.
- The average nose height, depth and speed of the summertime nocturnal wind jet at the exit of Weber Canyon were observed to be around 70 m, 400 m, and 18 m s^{-1}, respectively. The exit jet speeds at Weber Canyon are greater than for other previously reported valley exit jets.
- The strongest winds were contained within a strong surface-based temperature inversion both inside and at the exit of the canyon.

- There was little interannual variation of wind speeds in Weber Canyon over the last 10 years.
- The structure of the canyon exit jet varied depending on the synoptic weather conditions. Four exit jet regimes were identified based on a subjective analysis of several data sources. Strong deep jets were observed when the component of opposing synoptic flow was small or in the aiding direction and shallower jets were observed when the component of opposing synoptic flow was large.
- Several methods of acquiring wind and temperature profile data inside and at the exit of a narrow canyon were demonstrated.
- ValidWind^{TM}, a novel balloon tracking measurement system developed at Utah State University, was validated against the WindCube LiDAR during an IOP resulting in good agreement between the two measurement methods.
- The exit region of Weber Canyon has sufficient wind power potential to support commercial scale wind turbines. Common boundary layer methods of extrapolating wind speeds from tower measurements to a higher turbine hub height were shown to be inappropriate at this site due to the jet-like wind speed profiles. An overall negative bias of ~ 0.5 m s^{-1} was observed between the mean SoDAR profile and the mean tower profile at the same heights.

- Initial simulations using the WRF model produced fairly good agreement with observations. This bodes well for the future use of NWP models in predicting atmospheric flows in complex mountainous terrain.
- Model simulations show that a uniform flow layer accelerates in the lower portion of Weber Canyon and then compresses and further accelerates to form a jet at the exit region. This results in a strong vertical temperature gradient within the jet near the ground and a calm uniform neutral flow layer above the jet.
- Model simulations show that flow from Weber Canyon can extend into the GSLB tens of kilometers. Significant flow should also be expected from canyons adjacent to Weber Canyon and these flows can converge in the GSLB potentially leading to vertical atmospheric circulations.

Future Work

This thesis research investigated canyon exit jet formation along the Wasatch Front of northern Utah, and is one of the first studies of this phenomenon. This research project had a limited scope and budget, leaving much room for further research. A more comprehensive study of wind patterns within and at the exit of canyons along the Wasatch Front could help answer fundamental questions about the nature of canyon flows, how they develop, and if they have any impacts on flow properties or pollutant dispersion in the GSLB. This could be better quantified through the determination of a mass flow rate in each of the canyons, which would provide a measure of how much clean canyon air is advected and mixed into the GSLB. A study on the relationship between drainage basin and canyon exit geometry and flow characteristics could help

determine if properties other than drainage area are important in accounting for the flow variations observed between selected basins. Surface energy budget information was not available for this research but could help quantify the role of surface fluxes in the canyon drainage basins in the formation and maintenance of canyon flows.

Our initial model simulations demonstrate that the WRF model can predict atmospheric flows in complex terrain reasonably well using an LES technique. However, further optimization of the simulations is necessary to improve the results. The optimization should be focused around improving physical parameterizations and enhancing the representation of gridded terrain and land use data. As was described, new parameterizations exist for the treatment of sub-gridscale turbulence closure in the governing equations. These new parameterizations should be systematically tested in complex terrain. Fundamentally, methods for representing complex terrain while still maintaining numerical stability need further development. Lundquist et al. (2010) discuss how numerical errors are introduced using a traditional terrain following coordinate system. They propose an alternative method, the immersed boundary method (IBM), for high-resolution simulations in complex terrain. They state that the use of the IBM alleviates coordinate transformation errors and eliminates restrictions on terrain slope that currently limit mesoscale models to slowly varying terrain.

REFERENCES

Antoniou, I., H.E. Jørgensen, F. Ormel, S. Bradley, S. von Hünerbein, S. Emeis, and G. Warmbier, (2003): On the theory of SoDAR measurement techniques. Technical report from the Risø National Laboratory for Sustainable Energy. Technical University of Denmark.

Banta, R. M., L. D. Olivier, W. D. Neff, D. H. Levinson, and D. Ruffieux, 1995: Influence of canyon-induced flows on flow and dispersion over adjacent plains. *Theor. Appl. Climatology*, **52**, 27-41.

Banta, R. M., L. S. Darby, J. D. Fast, J. Pinto, C. D. Whiteman, W. J. Shaw, and B. D. Orr, 2004: Nocturnal low-level jet in a mountain basin complex. I: Evolution and effects on local flows. *J. Appl. Meteor*., **43**, 1348-1365.

Clements, W. E., J. A. Archuleta, and D. E. Hoard, 1989: Mean structure of the nocturnal drainage flow in a deep valley. *J. Appl. Meteor.*, **28**, 457-462.

Coulter, R.L., and P.Gudiksen, 1995: The dependence of canyon winds on surface cooling and external forcing in Colorado's front range. *J.Appl.Meteor*., **34**, 1419-1429.

Cramer, P., 1972: Potential temperature analysis for mountainous terrain. *J. Appl. Meteor.*, **11**, 44-50.

Crescenti, G., 1997: A look back on two decades of Doppler SoDAR comparison studies. *Bull. Amer. Meteor. Soc., **78**, 651-673.*

Darby, L. S., and R. M. Banta, 2006: The modulation of canyon flows by larger-scale influences. Ext. Abstr., *12th Conf Mount. Meteor.*, Santa Fe, NM. Amer. Meteor. Soc., Boston, MA.

Darby, L. S., K. J. Allwine, and R. M. Banta, 2006: Nocturnal low-level jet in a mountain basin complex. Part II: Transport and diffusion of tracer under stable conditions. *J. Appl. Meteor. Climatol.*, **45**, 740-753.

Doran, J. C., J. D. Fast, and J. Horel, 2002: The VTMX 2000 campaign. *Bull. Amer. Meteor. Soc.*, **83**, 537-551.

Dudhia, J., 1989: Numerical study of convection observed during the winter monsoon experiment using a mesoscale two-dimensional model. *J. Atmos. Sci*., **46**, 3077-3107.

Dwyer, T. J., M. Farley-Chrust, P. A. McMurtry, and E. R. Pardyjak, 2007: Siting wind turbines in complex terrain: Spanish Fork Canyon a case study. Paper proceedings of the 5th international conference for renewable energy, energy saving and energy education. Havana, Cuba.

Fast, J. D., and L. S. Darby, 2004: An evaluation of mesoscale model predictions of down-valley and canyon flows and their consequences using Doppler LiDAR measurements during VTMX 2000. *J. Appl. Meteor.*, **43**, 420-436.

Haiden, T., and C. D. Whiteman, 2005: Katabatic flow mechanisms on a low-angle slope. *J. Appl. Meteor*., **44**, 113-126.

Hong, S.-Y., J. Dudhia, and S.-H. Chen, 2004: A revised approach to ice microphysical processes for the bulk parameterization of clouds and precipitation. *Mon. Wea. Rev.*, **132**, 103-120.

Horel, J., M. Splitt, L. Dunn, J. Pechmann, B. White, C. Ciliberti, S. Lazarus, J. Slemmer, D. Zaff, and J. Burks, 2002: MesoWest: Cooperative mesonets in the western United States. *Bull. Amer. Meteor. Soc.*, **83**, 211-225.

International Energy Agency (IEA) (2003): Recommended Practices for Wind Turbine Testing and Evaluation: 11. Wind Speed Measurement and Use of Cup Anemometry (First Edition, 2nd Print 2003).

Janic, Z. I., 1990: The step-mountain coordinate: physical package. *Mon. Wea. Rev*., **118**, 1429-1443.

Janic, Z. I., 1996: The surface layer in the NCEP Eta Model. *Eleventh Conference on Numerical Weather Prediction*, Norfolk, VA, 19-23 August. Amer. Meteor. Soc., Boston, MA, 354-355.

Janic, Z. I., 2002: Nonsingular implementation of the Mellor-Yamada Level 2.5 scheme in the NCEP meso model. *NCEP Office Note*, **No. 437**, 61 pp.

Kain, J. S., 2004: The Kain-Fritsch convective parameterization: An update. *J. Appl. Meteor*,. **43**, 170-181.

Levinson, D. H., and R. M. Banta, 1995: Observations of a terrain-forced mesoscale vortex and canyon drainage flows along the Front Range of Colorado. *Mon. Wea. Rev.*, **123**, 2029-2050.

Lindelöw-Marsden, P., 2009: UpWind D1. Uncertainties in wind assessment with LiDAR. Technical report from the Risø National Laboratory for Sustainable Energy. Technical University of Denmark.

Lundquist, K. A., F. K. Chow, and J. K. Lundquist, 2010: An immersed boundary method for the weather research and forecasting model. *Mon. Wea. Rev*., **138**, 796-817.

Manwell, J. F., J. G. McGowan, and A. L. Rogers, 2002: *Wind Energy Explained, Theory, Design and Application*. John Wiley and Sons, LTD, 577 pp.

Mellor, G. L., and T. Yamada, 1982: Development of a turbulence closure model for geophysical fluid problems. *Rev. Geophys. Space Phys*., **20**, 851-875.

Mesinger, F., and Coauthors, 2006: North American Regional Reanalysis. *Bull. Amer. Meteor. Soc*., **87**, 343-360.

Mirocha, J. D., J. K. Lundquist, and B. Kosovic, 2010: Implementation of a nonlinear subfilter turbulence stress model for large eddy simulation in the advanced research WRF model. *Mon. Wea. Rev*., **138,** 4212-4228**.**

Mlawer, E. J., S. J. Taubman, P. D. Brown, M. J. Iacono, and S. A. Clough, 1997: Radiative transfer for inhomogeneous atmosphere: RRTM, a validated correlated-k model for the longwave. *J. Geophys. Res*., **102** (D14), 16663-16682.

Monin, A. S., and A. M. Obukhov, 1954: Basic laws of turbulent mixing in the surface layer of the atmosphere. *Contrib. Geophys. Inst. Acad. Sci*., USSR, **151**, 163-187.

Pamperin, H., and G. Stilke, 1985: Nächtliche Grenzschicht und LLJ im Alpenvorland nahe dem Inntalausgang. [Nocturnal boundary layer and low level jet near the Inn Valley exit]. *Meteor. Rundsch.*, **38**, 145-156.

Pedersen, T. F., 2001: Cup anemometer characteristics with respect to recommendations in the Danish certification system. Technical report from the Risø National Laboratory for Sustainable Energy. Technical University of Denmark.

Poulos, G. S., and S. Zhong, 2008: The observational history of small-scale katabatic winds in mid-latitudes. *Geography Compass,* **2**, 1798-1821.

Rife, D. L., C. A. Davis, Y. Liu, and T. T. Warner, 2004: Predictability of low-level winds by mesoscale meteorological models. *Mon. Wea. Rev*., **132**, 2553-2569.

Skamarock, W. C., and Coauthors, 2008: A description of the advanced research WRF version 3, NCAR Technical Note NCAR/TN–475+STR, National Center for Atmospheric Research, 88 pp.

Spengler, T., J. H. Schween, M. Ablinger, G. Zangl, and J.Egger, 2009: Thermally driven flows at an asymmetric valley exit: Observations and model studies and the Lech Valley exit. *Mon. Wea. Rev.*, **137**, 3437-3454.

Stewart, J. Q., C. D. Whiteman, W. J. Steenburgh, and X. Bian, 2002: A climatological study of thermally driven wind systems of the US Intermountain West. *Bull. Amer. Meteor. Soc*., **83**, 699-708.

Stilke, G., 1984: Nocturnal boundary layer and low-level jet in the pre-Alpine region near the outlet of the Inn Valley. *Zbornik Meteor. i Hidrol. Radova,* Beograd, **10**. Proceedings, 18th Intern. Conf. for Alpine Meteorology, Opatija, 25-28 September 1984, 68-71.

Vergeiner, I., and E. Dreiseitl, 1987: Valley winds and slope winds-observations and elementary thoughts. *Meteor. Atmos. Phys.*, **36**, 264-286.

Whiteman, C. D., 1990: Observations of Thermally Developed Wind Systems in Mountainous Terrain. Chapter 2 in Atmospheric Processes Over Complex Terrain, (W. Blumen, Ed.), *Meteorological Monographs*, **23**, no. 45. American Meteorological Society, Boston, Massachusetts, 5-42.

Whiteman, C. D., 2000: *Mountain Meteorology, Fundamentals and Applications.* Oxford University Press, 355 pp.

Whiteman, C. D., and S. Zhong, 2008: Downslope flows on a low angle slope and their interaction with valley inversions. Part I: Observations. *J. Appl. Meteor. Climatol.*, **47**, 2023-2038.

Wilkerson, T., A. Marchant, T. Apedaile, J. Simmons, and B. Bradford, 2010: ValidWind applications: wind power prospecting and aerosol transport. *Proceedings of SPIE-Europe*, 7832, in press.

Zängl, G., 2004: A reexamination of the valley wind system in the Alpine Inn Valley with numerical simulations. *Meteor. Atmos. Phys.*, **87**, 241-256.

Zhong S., and J. Fast, 2003: An evaluation of the MM5, RAMS and Meso-Eta models at subkilometer resolution using VTMX field campaign data in the Salt Lake Valley. *Mon. Wea. Rev*., **131**, 1301-1322.

Zhong S., and C.D. Whiteman, 2008: Downslope flows on a low angle slope and their interaction with valley inversions. Part II: Numerical Modeling. *J. Appl. Meteor. Climatol.*, **47**, 2039-2057.